

Single-Walled Carbon Nanotubes

Sebastien Nanot, Nicholas A. Thompson, Ji-Hee Kim, Xuan Wang, William D. Rice, Erik H. H  roz, Yogeewaran Ganesan, Cary L. Pint, Junichiro Kono

Single-walled carbon nanotubes (SWCNTs) are hollow, long cylinders with extremely large aspect ratios, made of one atomic sheet of carbon atoms in a honeycomb lattice. They possess extraordinary thermal, mechanical, and electrical properties and are considered as one of the most promising nanomaterials for applications and basic research. This chapter describes the structural, electronic, vibrational, optical, transport, mechanical, and thermal properties of these unusual one-dimensional (1-D) nanomaterials. The crystallographic (Sect. 4.2.1), electronic (Sect. 4.2.2), vibrational (Sect. 4.2.3), optical (Sect. 4.4), transport (Sect. 4.5), thermal (Sect. 4.6.1), and mechanical (Sect. 4.6.2) properties of these unusual 1-D nanomaterials will be outlined. In addition, we will provide an overview of the various methods developed for synthesizing SWCNTs in Sect. 4.3.

Even after more than two decades of extensive basic studies since their discovery, carbon nanotubes continue to surprise researchers with potential new applications and interesting discoveries of novel phenomena and properties. Because of an enormous thrust towards finding practical applications, carbon nanotube research is actively being pursued in diverse areas including energy storage, molecular electronics, nanomechanical devices, composites, and chemical and bio-sensing.

Structurally, carbon nanotubes are made up of sp^2 -bonded carbon atoms, like graphite, and can be conceptually viewed as rolled-up sheets of single-layer graphite, or graphene. Their diameter typically lies in the nanometer range while their length often exceeds microns, sometimes centimeters, thus making them 1-D nanostructures. Depending on the number of tubes that are arranged concentrically, carbon nanotubes are further classified into single-walled and multi-

walled nanotubes. Single-walled carbon nanotubes, the subject of this chapter, are especially interesting. They are ideal materials in which to explore one-dimensional physics and strong Coulomb correlations. In addition, their cylindrical topology allows them to exhibit nonintuitive quantum phenomena when placed in a parallel magnetic field, due to the Aharonov-Bohm effect. A number of research groups have found exotic many-body effects through a variety of transport, optical, magnetic, and photoemission experiments.

Their electronic properties are very sensitive to their microscopic atomic arrangements and symmetry, covering a wide spectrum of energy scales. They can be either metallic or semiconducting with varying band gaps, depending on their diameter and chirality. Semiconducting nanotubes are particularly promising for photonic device applications with their diameter-dependent, direct band gaps, while metallic tubes are considered to be ideal candidates for a variety of electronic applications such as nanocircuit components and power transmission cables.

4.1 History	106
4.2 Crystallographic and Electronic Structure	106
4.2.1 Crystallographic Structure	106
4.2.2 Electronic Dispersion	107
4.2.3 Phonon Dispersion	109
4.3 Synthesis	111
4.3.1 Substrate-Free Growth Techniques	112
4.3.2 Substrate-Bound Growth Technique	113
4.3.3 Growth Mechanisms	114
4.4 Optical Properties	115
4.4.1 Optical Absorption and Photoluminescence	116

4.4.2 Raman Spectroscopy.....	118	4.6 Thermal and Mechanical Properties.....	128
4.4.3 Resonant Rayleigh Spectroscopy.....	119	4.6.1 Thermal Properties	128
4.4.4 Ultrafast Spectroscopy.....	120	4.6.2 Mechanical Properties.....	130
4.4.5 Excitonic Effects	121	4.7 Concluding Remarks	135
4.5 Transport Properties	123	References	135

4.1 History

This chapter summarizes some of the basic properties of carbon nanotubes (CNTs), one of the most ideal realizations of one-dimensional (1-D) systems available today. Since their discovery [4.1], much attention has been given to their unique structure and properties that are promising for a wide range of applications and fundamental physical and chemical studies [4.2–5]. These hollow crystals of sp²-bonded carbon atoms have exhibited a variety of extraordinary thermal, mechanical, and electrical properties and phenomena, fascinating scientists and engineers in diverse disciplines. Even after more than two decades of extensive basic studies since their discovery, they continue to surprise researchers through exciting discoveries of phenomena and properties as well as novel potential applications, including energy storage, molecular electronics, nanomechanical devices, composites, and chemical and bio-sensing.

The diameters of carbon nanotubes are in the nanometer range while their lengths are typically microns and often millimeters, corresponding to aspect ratios of millions, especially in single-walled carbon nanotubes (SWCNTs), the most prominent member of the carbon nanotube family. A typical SWCNT has a diameter of ≈ 1 nm and consists of just one atomic sheet, which can be pictured as a rolled-up version

of graphene, i.e., a honey-comb lattice of sp²-bonded carbon atoms. The one-dimensionality of SWCNTs is attractive, allowing researchers to explore exotic 1-D physics in the quantum regime [4.6] and new functionalities in optoelectronic devices [4.7, 8]. The strong 1-D confinement of electrons and phonons results in unique anisotropic effects in various properties, e.g., polarization-dependent Raman scattering [4.9] and optical absorption [4.10–12], large magnetic susceptibility anisotropies [4.13–17], and anisotropic terahertz dynamic conductivities [4.18–21].

One of the most striking properties of SWCNTs is their chirality-dependent metallicity. Namely, depending on their microscopic atomic arrangements and symmetry, a SWCNT can be either metallic or semiconducting. A subtle structural difference leads to opening or closing of a band gap, which is also tunable by a magnetic field applied parallel to the tube axis via the Aharonov–Bohm effect [4.10, 22–25]. Semiconducting nanotubes are particularly promising for photonic device applications with their diameter-dependent, direct band gaps, while metallic tubes are considered to be ideal candidates for a variety of electronic and electrical applications ranging from nano-circuit wires to power transmission cables.

4.2 Crystallographic and Electronic Structure

A SWCNT can be viewed as a graphene sheet rolled into a cylinder which is terminated by two half-fullerene caps. The diameter of these species typically ranges from 0.7 to 2.5 nm, and their aspect ratio can be as high as 10⁴–10⁵. This very strong confinement along their circumference make them behave like 1-D materials. The purpose of this section is to describe the crystallographic and electronic structure of SWCNTs, which will be used throughout the text. For a more detailed

study we refer the reader to some of the many published books [4.2, 5, 26–28].

4.2.1 Crystallographic Structure

To give a formal description of the crystal structure of a SWCNT, it is easiest to first consider its parent material, graphene. Graphene is a monolayer of sp²-hybridized carbon atoms arranged in a honeycomb

lattice. Its unit cell is defined by the primitive vectors \mathbf{a}_1 and \mathbf{a}_2 (bottom right of Fig. 4.1, for a review see [4.29]). Each SWCNT is then indicated by a *chiral vector* \mathbf{C}_h , which specifies the two atoms of the graphene sheet which are identified upon formation of the tube (see the points O and A in Fig. 4.1). The chiral vector is defined with respect to the graphene primitive vectors as

$$\mathbf{C}_h \equiv n\mathbf{a}_1 + m\mathbf{a}_2 \equiv (n, m), \quad (4.1)$$

where n and m are integers such that $0 \leq m \leq n$. When we express the chiral vector \mathbf{C}_h in the form (n, m) , we call it the *chiral index*. These two terms should be regarded as synonymous. The angle θ formed between \mathbf{C}_h and \mathbf{a}_1 is a quantity of great importance for determining the electronic properties of the SWCNT; it is called the *chiral angle*, and is defined through

$$\cos \theta = \frac{\mathbf{C}_h \cdot \mathbf{a}_1}{|\mathbf{C}_h| |\mathbf{a}_1|} = \frac{2n + m}{2\sqrt{n^2 + m^2 + nm}}. \quad (4.2)$$

The nanotube diameter can be computed from the chiral vector by

$$d_t = |\mathbf{C}_h| / \pi = \frac{a_{C-C}}{\pi} \sqrt{3(m^2 + mn + n^2)}, \quad (4.3)$$

where $a_{C-C} \approx 1.44 \text{ \AA}$ is the nearest neighbor distance between carbon atoms in graphene.

SWCNTs can be classified into three main types:

1. *Armchair* nanotubes for which $n = m$ (i.e. $\mathbf{C}_h = (n, n)$)
2. *Zig-zag* nanotubes for which $m = 0$ (i.e. $\mathbf{C}_h = (n, 0)$)
3. *Chiral* nanotubes ($n \neq m \neq 0$) whose mirror images have a different structure and display different properties, for example in circular dichroism.

Armchair and zigzag nanotubes (having the highest symmetry) (Fig. 4.1b) are named after the shape of their cross section along \mathbf{C}_h . All three of these different structures will display various physical properties and their distinction will be of prime importance for their electronic structure, phonon dispersion and optical properties.

4.2.2 Electronic Dispersion

Single-walled carbon nanotubes can be either metals or semiconductors depending on their chirality (Sect. 4.2.1). Their metallicity can be deduced from purely geometrical considerations related to their chiral angle. Similar conclusions can be drawn from

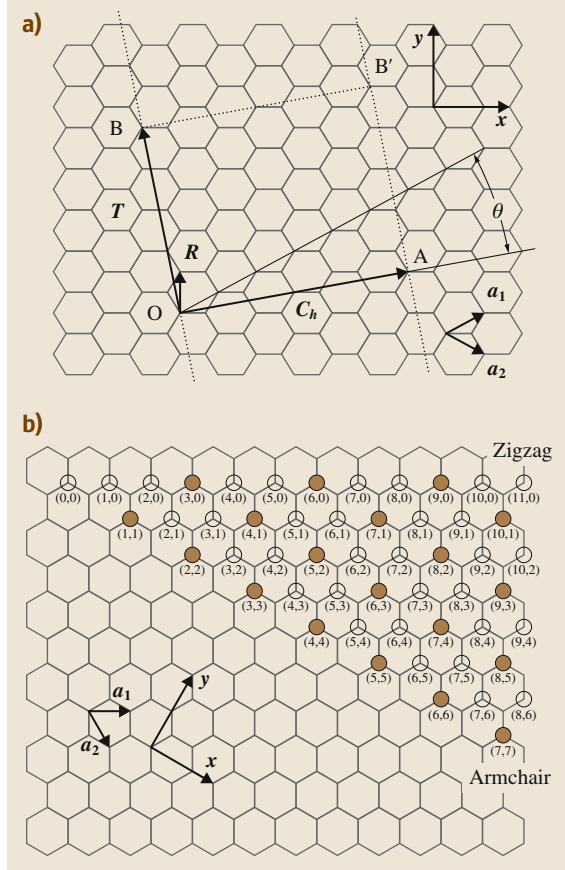


Fig. 4.1 (a) The unrolled hexagonal lattice of a nanotube. When we connect sites O–A, and B–B', a nanotube can be constructed. \mathbf{OA} and \mathbf{OB} define the chiral vector \mathbf{C}_h and the translational vector \mathbf{T} of the nanotube, respectively. The rectangle OAB'B defines the unit cell for the nanotube. The vector \mathbf{R} denotes a symmetry vector. (b) The hexagonal lattice of all possible (n, m) species formed by rolling the $(0, 0)$ point onto (n, m) . The empty circles are semiconducting (n, m) , ($v = \pm 1$). The filled circles represent *metallic*, $v = 0$ (n, m) species. (After [4.26])

tight-binding models of graphene [4.30, 31] or $\mathbf{k} \cdot \mathbf{p}$ formalism for low energy bands [4.32], although the precise band structure of (very) small diameter nanotubes necessitates more complex calculations which include curvature effects, second neighbor interactions, or the use of ab initio methods [4.33].

The electronic properties of graphene have been studied extensively [4.29], so here we will only describe the properties useful for deducing the nanotube band structure. The graphene reciprocal lattice is hexagonal

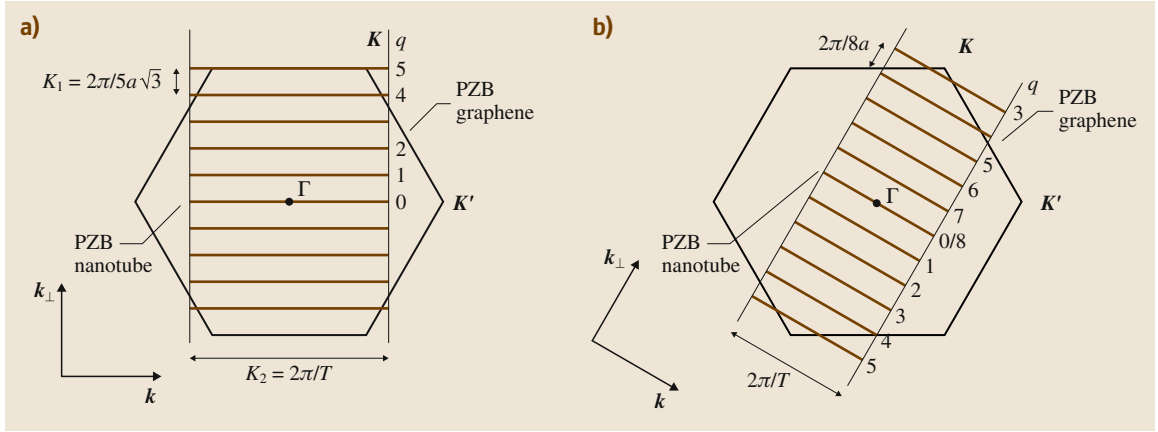


Fig. 4.2a,b First Brillouin zone and quantized vectors of (a) an armchair nanotube (5,5) and (b) a zigzag nanotube (8,0) with rotational indices q corresponding to the zone folding method indices. PZB = 1st Brillouin zone (After [4.35])

and the (nonequivalent) points K and K' at the corners of the first Brillouin zone (called *Dirac points*) are of particular importance for its electronic properties. The valence and conduction band meet only at the Dirac points [4.34], making graphene a zero bandgap semiconductor. Moreover, its dispersion is linear close to these points and hence low energy carriers behave like massless, chiral Dirac fermions. As a consequence, its electronic dispersion near the Dirac points is well described by

$$E(\delta k) = \pm \hbar v_F \delta k, \quad (4.4)$$

where $v_F = \sqrt{3}\gamma_0 a / 2\hbar \approx 9.5 \times 10^5$ m/s is the electron Fermi velocity, $\gamma_0 = 2.9$ eV is the nearest neighbor hopping energy, $a = |\mathbf{a}_1| = |\mathbf{a}_2| = 2.49$ Å and δk is the wavevector with origin at either the K or K' point.

The periodicity condition introduced on the wavefunctions along the circumference of carbon nanotubes induces a quantization along their axes. As a consequence, they are quasi-1-D systems with only specific \mathbf{k} vectors allowed along the circumference and the base vector parallel to the axis, as illustrated in Fig. 4.2. The mono-electronic dispersion relation can be directly deduced from graphene by using the *zone folding method*, which imposes the periodic boundary condition $\psi(x + nC_h) = \psi(x)$ on graphene. The continuous graphene wavevector is replaced by a *half-quantized* new vector (continuous along the nanotube axis and quantized along the circumference). As can be seen from Fig. 4.2, a specific (n, m) nanotube will be metallic if an authorized subband crosses the K point or semiconducting otherwise. Simple geometric considerations related the chiral vector C_h allows one to deduce

that the condition for a nanotube to be metallic is $n - m = 3\ell$ ($\ell \in \mathbb{N}$) [4.30, 31, 33]. If we define $\nu \equiv n - m \bmod 3$, we can see that $\nu = 0$ if the nanotube is metallic and $\nu = \pm 1$ if it is a semiconductor. Hence one-third of all possible carbon nanotube species are expected to be metallic.

Using (4.4), one can deduce the band structures close to the K points through the $\mathbf{k} \cdot \mathbf{p}$ formalism [4.32]

$$E_q(k) = \pm \gamma_0 \sqrt{\left(q - \frac{\nu}{3}\right)^2 + \left(\frac{k d_t}{2}\right)^2}. \quad (4.5)$$

Noticeably:

- Metallic nanotubes have a linear dispersion and massless charge carriers, just as their parent material graphene
- Semiconducting nanotubes have a band gap $E_g = 2\gamma_0 a_{C-C} / d_t \approx 0.839$ eV · nm/ d_t .

A complete band structure can be deduced by folding the tight-binding dispersion of graphene [4.30, 31, 33]. This is shown for a representative metallic armchair nanotube and a semiconducting zigzag nanotube of similar diameters in Fig. 4.3. Due to symmetries of the K and K' points, all subbands are doubly degenerate. The corresponding density of states (Fig. 4.4) is constant in the metallic bands and presents van Hove singularities typical of 1-D systems at the onset of each new subband.

These considerations are sufficient for nanotubes with large diameter. However, for small diameter nanotubes, one has to consider the distortions of the

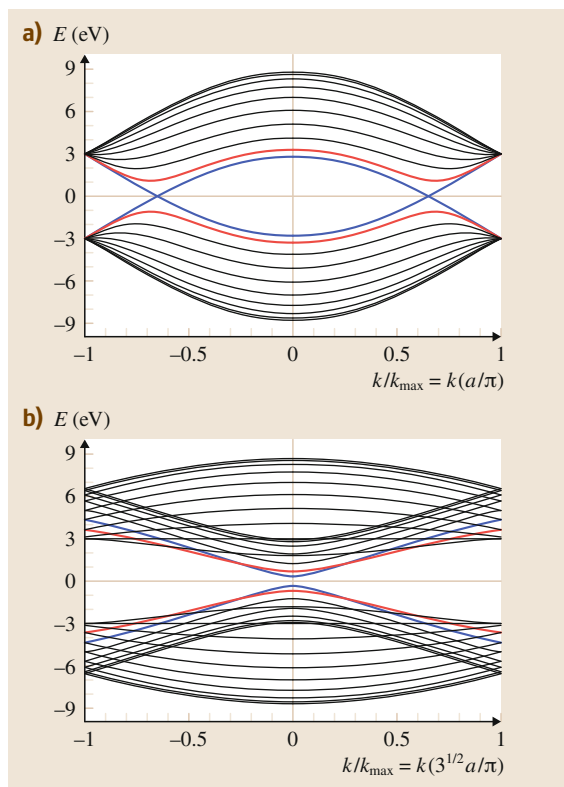


Fig. 4.3a,b Electronic dispersion of (a) a metallic (9,9) armchair nanotube and (b) a semiconducting (16,0) zigzag nanotube. Both nanotubes have similar diameter $d_t \approx 1.2$ nm

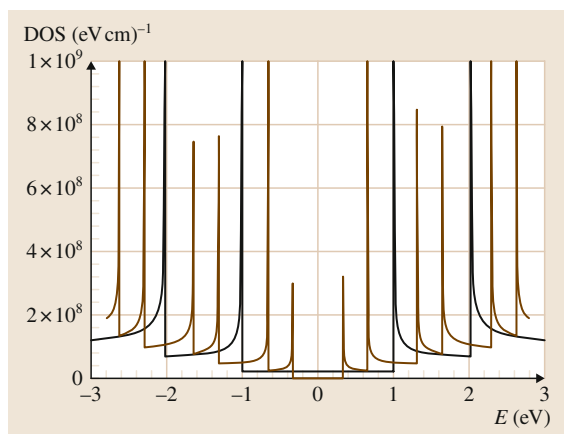


Fig. 4.4 Density of states (DOS) of the same SWCNTs as above; a metallic (9,9) armchair nanotube (black curve) and a semiconducting (16,0) zigzag nanotube (dark-brown curve)

hexagonal lattice due to curvature [4.31, 36] and that graphene dispersion is not linear at the high energies where new subbands appear (i. e., (4.4) and (4.5) are no longer valid, due to trigonal warping effects). These become of particular importance for optical experiments and low temperature transport measurements. Important considerations are:

- Armchair (n, n) nanotubes are the only truly metallic nanotubes.
- Other nanotubes satisfying $n - m \bmod 3 = 0$ but $n \neq m$ develop a small band gap (typically on the order of some tens of meV) and the degeneracy between higher energy subbands is lifted.
- Semiconducting nanotubes develop a chirality dependent band gap (with a term proportional to $\cos(3\theta)$).

4.2.3 Phonon Dispersion

Atomic vibrational motions of carbon nanotubes are very similar to those of graphene but due to their cylindrical symmetry they are separated into radial *breathing* modes (along the radial axis), transverse modes (along the azimuth angle axis), and longitudinal modes (along the length axis) [4.37]. The phonon band structure has been calculated by various methods including zone folding [4.38, 39], constant force [4.40, 41], tight-binding [4.42, 43] and ab initio methods [4.44–46]. Similar to the electronic structure, the phonon dispersion in SWCNTs is quantized and exhibits singularities specific to their 1-D nature.

Due to its honeycomb lattice containing two atoms in each unit cell, graphene phonon dispersion contains six modes, with two types of transverse and one type of longitudinal motions; hence three acoustic and three optical modes. There are two main consequences when wrapping a graphene sheet into an SWCNT. First, it introduces a periodic boundary condition along the circumference, which quantizes the corresponding wavevector. As a result, the 2-D graphene phonon modes are further split into a large number of subbands. If the SWCNT contains $2N$ atoms per unit cell, there are $6N$ phonon modes in total, many of which are degenerated (Fig. 4.5b,c [4.45]). The second consequence is that the curvature makes its three fundamental atomic motions different from those of graphene. Hence, the SWCNT phonon modes can be viewed as a mixture of 2-D graphene phonon modes [4.37]. The effect of such symmetry difference is significant for lower frequency modes. For instance, there are four acoustic modes in-

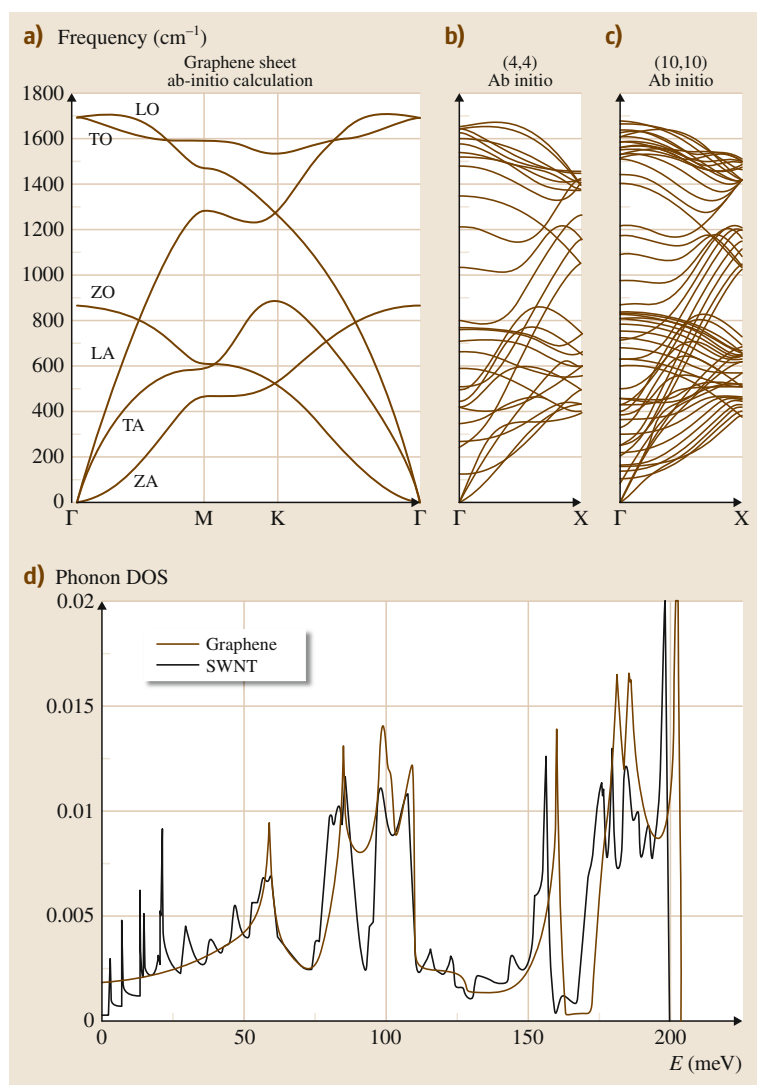


Fig. 4.5 (a). Ab initio dispersion relations for the (4,4) (b), and the (10,10) (c) nanotubes. In (c) and (d), thicker lines are used to mark two special branches: the acoustic band is a twist mode (torsional shape vibrations), the other (with finite frequency γ) is the breathing mode. (d) Phonon density of states of an isolated (10,10) SWCNT (solid line), compared to a 2-D graphene sheet. ((a–c) after [4.45], (d) after [4.48])

stead of three (Fig. 4.5b,c [4.47]; also see Fig. 4.25a for a larger view):

- A *longitudinal acoustic* (LA) mode, corresponding to motion of the atoms along the tube axis (similar to the LA mode in graphene).
- Two degenerate *transverse acoustic* (TA) modes, corresponding to atomic displacements perpendicular to the nanotube axis (a combination of in-plane and out-of plane TA modes in graphene).
- A *twist mode*, corresponding to a torsion of the tube around its axis (similar to the in-plane TA modes in graphene).

The *radial breathing mode* (RBM) is another important low-frequency mode, corresponding to radial expansion-contraction of the nanotube. It is similar to the out-of plane TA mode in graphene with zero energy at the center of the Brillouin zone, but becomes a mode with a finite energy due to the curvature. To first order, the energy of the RBM mode is inversely proportional to the diameter of the tube and presents chiral angle dependencies similar to electronic subbands [4.44].

Figure 4.5d shows the calculated phonon density of states of a (10, 10) tube and a graphene sheet side by side [4.49]. One of the main features is that the

SWCNT phonon density of states has a number of sharp peaks (van Hove singularities) due to its 1-D structure. Such a difference is more profound at lower frequencies, because low frequency phonon modes are more reflective of the symmetry of carbon nanotubes, while higher frequency modes are more reflective of carbon-carbon bonding. For this nanotube the calculated energy of RBM mode is 21.7 meV while the first van Hove singularity appears at about 2.5 meV. Van Hove singularities have been observed by neutron scattering experiments [4.48], thus confirming theoretical calculation.

When carbon nanotubes are bundled together, the intertube interaction will introduce dispersion along the transverse (intertube) direction. This will reduce the density of phonon states at low frequency, which has profound effect on the thermal properties of SWCNTs [4.49]. However, the heterogeneous nature of carbon nanotube bundles make theoretical calculation difficult. Figure 4.6 shows a tight-binding calculation for the case of graphite-like SWCNT bundles [4.50]. It can be seen that the intertube acoustic modes have fairly flat dispersion and the overall phonon frequencies are much less than those of intratube modes. Consequently, these modes should have very low Debye temperature

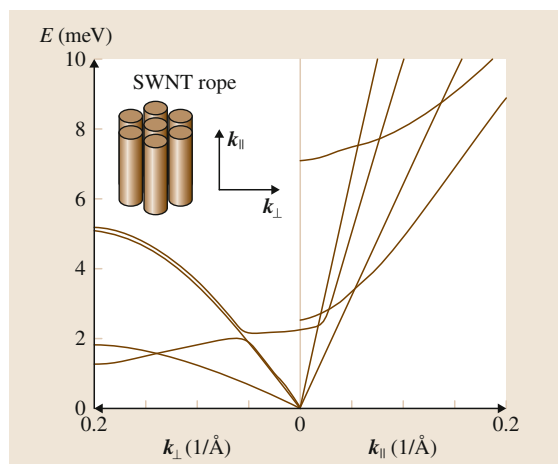


Fig. 4.6 Calculated low-energy phonon band structure of a SWNT bundle, for the case of graphite-like (strong) coupling

Θ_D and their contributions are only significant at very low temperature. The intratube modes are also different from those for SWCNT showing a shift in frequency, which mostly affects low frequency modes or small diameter SWCNTs [4.37, 51].

4.3 Synthesis

Over 20 years after the first batches of carbon nanotubes (CNTs) were synthesized and documented as such [4.1], CNTs continue on a steady trajectory toward industrial applications while many of the remaining challenges of growth continued to be ironed out. Whereas CNT growth has been a dynamic topical area for the past few decades, the gap between readily available products incorporating CNTs and the progression of studies in this area remains significant. In recent years, it has been estimated that the capacity for production of multi-walled CNTs could be as high as 300 to/yr, whereas that of single-walled CNTs could be as high as 7 to/yr [4.52]. However, the challenge required to further push production levels is to build a global market for CNT-based products that will instigate further scale-up production based on cost, safety, and material performance, and to develop understanding of CNT growth that will aid in the design of cheaper, more efficient synthesis techniques. One drawback to industry is that many of the largest potential CNT markets require specific homogeneous properties, even though most large-scale CNT synthesis techniques yield mixtures of CNTs with dif-

ferent diameters and physical properties. This motivates research efforts continuing in the area of CNT growth to understand how to tighten the CNT diameter and property distribution by building a strong understanding of the growth processes and mechanisms. However, there is still a market even for wide-distribution multi-walled CNTs that can be produced at low cost in bulk quantities for their use as structural enhancers in materials.

The purpose of this section is to introduce the reader to the different techniques utilized to synthesize carbon nanotubes in addition to the different types of carbon nanotubes that can be produced using these methods. The caveat to this section is that the sheer breadth of techniques utilized in CNT growth makes it challenging to present a unified picture of CNT growth processes explaining every observation made thus far. A myriad of unique processes and systems have been utilized to grow CNTs, often reporting conflicting mechanistic results. Therefore, this section will focus on the ideas that have been accepted and have the capability to apply broadly to the vast majority of growth techniques discussed.

4.3.1 Substrate-Free Growth Techniques

In general, one can separate the growth of CNTs into two different categories: substrate-free CNT growth and substrate-bound CNT growth. By far, substrate-free CNT growth processes make up the majority of the large-scale industrial efforts due to the ease of scaling such techniques to implement continuous processes as opposed to operating using batch processes. From a historical perspective, two primary techniques have built the foundation of substrate-free CNT growth processes, which are (i) arc discharge [4.55, 56] and (ii) laser ablation [4.57]. In an arc discharge growth process, illustrated in Fig. 4.7a, two graphite electrodes are utilized in a chamber with an inert gas. A DC power supply is connected across the two electrodes (or rods) that passes electric current through the electrode configuration. This creates a discharge that consumes one of the electrodes and leaves a deposit on the other electrode that contains carbon nanomaterials that can vary in composition depending on the specific conditions utilized. One can tune the process to produce primarily multi-walled CNTs using two standard graphite electrodes to a process that produces single-walled CNTs using metal catalysts such as Ni, Fe, Mo, or Co doped into the electrode. Arc discharge is the most straightforward approach to synthesize carbon nanotubes, but its application as a large-scale production technique suffers due to the moderate yield of CNTs (often between 30–50%) amidst a variety of other carbons that requires one to employ post-process separation techniques to achieve well-defined samples. However, arc discharge processes predate carbon nanotubes and were readily employed in the synthesis of carbon whiskers and C₆₀ decades before the report by Iijima in 1991 [4.58]. It is suggested that processes to form carbon materials using arc discharge date back to the 1960s, and closer analysis of

the soot in these materials would have revealed carbon nanotubes.

Laser ablation growth of CNTs (Fig. 4.7b), on the other hand, is a process whereby the energy is supplied to the graphite target using either a continuous wave or pulsed laser, in comparison to a DC power supply in arc discharge. In laser ablation growth, the laser hits a hot target, which typically involves graphite with a catalytic metal (Ni, Fe, Co, etc.) doped into it, and vaporizes the target. Downstream of the target, a water-cooled condenser collects the product of the vaporized carbon/metal mixture that is carried using a flow of inert gas, such as Ar. Laser ablation processes can also be tuned to yield either single-walled CNTs or multi-walled CNTs based on the variation of parameters in the growth process such as the laser wavelength, laser power, laser pulse duration, furnace temperature, and graphite target composition. In particular, a low metal : graphite ratio in the target and a high furnace temperature (typically $\approx 1200^\circ\text{C}$) is generally associated with good quality crystalline single-walled CNTs, whereas greater amounts of metal yields multi-walled CNTs, and lower furnace temperatures compromise crystallinity of the CNT tube walls. Today, laser ablation and arc discharge processes are still employed readily in the research lab, although industry scale-up efforts have typically not incorporated these techniques due to the *batch-by-batch* nature of these processes and the common difficulty of getting mixtures of CNTs and amorphous carbons, metals, or fullerenes. However, significant progress has been made in utilizing processes such as laser ablation to yield controllable double-walled CNTs with moderately small diameters (2–3 nm) compared to other techniques.

Aside from these techniques, there are a myriad of other processes that have been developed and adopted for substrate-free CNT synthesis. Many of these techniques represent a form of chemical vapor deposition

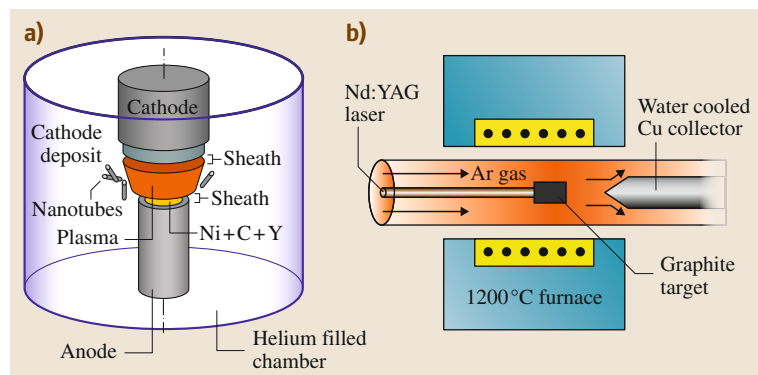


Fig. 4.7a,b Illustration of (a) an arc-discharge apparatus and (b) a laser ablation apparatus for growing carbon nanotubes. ((a) After [4.53]. (b) After [4.54])

(CVD) that can be scalable to large areas or can produce bulk quantities using cost-effective continuous processing. Generally, CVD techniques for CNT growth involve the reaction of a feedstock gas that contains carbon with nanoscale metal catalyst particles inside a heated reaction zone. For substrate-free synthesis processes, the metal is typically supplied during the process. Two notable processes that have proved capable of industrial-scale production are the HiPco process and fluidized bed CVD. The HiPco process was first designed at Rice University, with reports as early as 2001 documenting lab-scale SWNT production at 0.45 g/day [4.59]. The HiPco process is a form of CVD where an organometallic compound, such as $\text{Fe}(\text{CO})_5$, is fed into a reaction zone at high pressures (up to 50 atm) and high temperatures (900–1100 °C). This process causes the organometallic compound to decompose into small, nanoscale metal clusters that catalyze the CO disproportionation reaction to form by-products of CO_2 and single-walled CNTs. Although additional processes for synthesizing single-walled CNTs have been developed on an industrial front in recent years, much of the widespread CNT research efforts over the past decade can be attributed to the HiPco process.

In addition to HiPco, another key CVD-based process that has demonstrated significant potential for large-scale production is the fluidized bed CVD (FB-CVD) process [4.62]. In this process, illustrated in Fig. 4.8, feedstock gases and catalyst material are fed into the reaction zone forming CNTs that are then collected in a continuous fashion. In some cases, the FB-CVD process involves two distinct reaction zones whereby a catalyst precursor reacts in the first zone forming the catalytic material, and this then flows downstream to the reaction zone where the CNTs form through reaction with this catalytic material. The benefit of this process is that the catalyst source is continuous, enabling the development of highly scalable CNTs with controllable properties in many cases. However, the drawback to FB-CVD is often the excess metal present in the CNTs that can be difficult to remove, and the difficulty achieving the level of precision in growth processes that can be comparable to fixed substrate-based CNT growth techniques.

4.3.2 Substrate-Bound Growth Technique

Whereas substrate-free growth techniques have been the medium for bridging the CNT synthesis effort to the industrial marketplace, substrate-bound CNT growth represents a growth form that is more tailored to

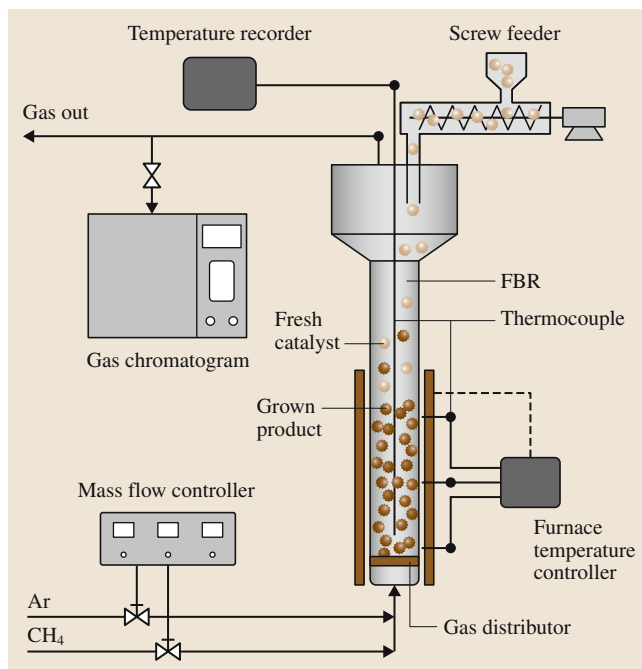


Fig. 4.8 Schematic diagram of a fluidized bed chemical vapor deposition system. (After [4.60])

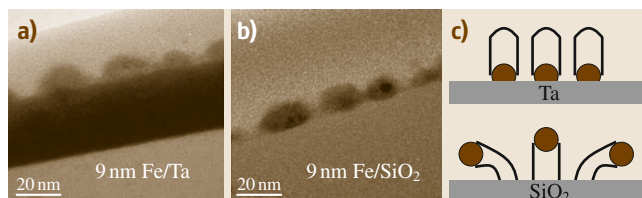


Fig. 4.9 (a,b) TEM images of catalyst particles that grow CNTs supported on Ta and SiO_2 . (c) Schematic showing how the substrate supporting the particles dictate whether tip growth (SiO_2) or base growth (Ta) is achieved. (After [4.61])

electronics or specialized fields. Substrate-based CNT growth is almost always based on variations of the CVD growth technique and involves a substrate that usually supports both the CNTs formed during growth in addition to the catalyst material that grows the CNTs. In substrate-bound CVD growth, there are two types of growth modes that are well-accepted, which are (i) *base-growth* where growth of CNTs occurs while the layer of catalyst nanoparticles remains at the interface with the growth substrate, and (ii) *tip-growth*, where the catalyst nanoparticles lift off the substrate and are supported by the growing CNT during the growth process (Fig. 4.9). In a typical substrate-bound CNT growth ex-

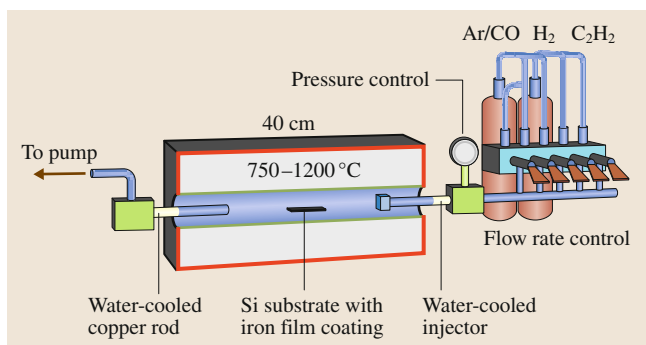


Fig. 4.10 Schematic of thermal CVD system setup generally utilized in aligned CNT growth (courtesy Atomic Physics, Göteborg University)

periment using thermal CVD, the substrate containing the catalyst is placed into a heated zone, and a flow of carbon feedstock initiates the nucleation and growth of the CNTs. Variations of this process include plasma-enhanced CVD [4.63] and hot-filament CVD [4.64], where the plasma or hot filament act as energy sources to form reactive species for catalytic growth that would otherwise not form in a thermal CVD environment. A general illustration of a thermal CVD system utilized in these sort of experiments is shown in Fig. 4.10.

One of the most remarkable observations for the substrate-based growth of CNTs was the notion that a thin, uniform layer of catalytic material can be deposited onto the surface of a substrate, and the growth from this catalytic layer can result in self-oriented, aligned arrays of CNTs. Whereas this was initially shown for multi-walled CNTs in 1999 [4.66], by 2004 a few groups had demonstrated this for single-walled CNTs as well [4.67, 68]. One of the most notable observations early-on was that the addition of a small amount of H₂O during the catalytic reaction in addition to the carbon feedstock can accelerate the growth process dramatically, yielding millimeter-scale single-walled CNT arrays that grow in 10 min or less. Since the CNTs produced in this novel synthetic approach – which themselves are only a few nanometers in diameter – can be greater than a centimeter [4.69] in length and grown in structures where alignment is inherent from the stage of growth, these materials drew excitement from researchers. Figure 4.11 shows an SEM image of a short CNT forest where the individual CNT bundles are visible. In particular, substrate-free growth techniques such as arc discharge, laser ablation, or HiPco yield tangled CNTs that have submicron lengths. The challenge that remains for these materials is that

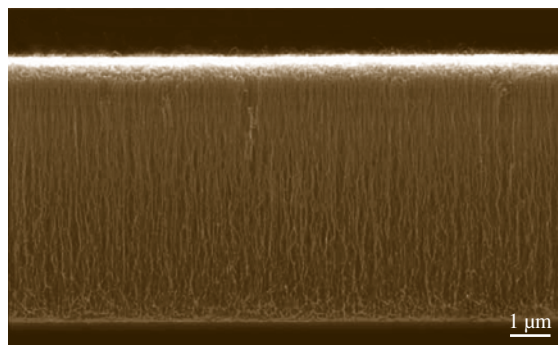


Fig. 4.11 SEM image of a vertically aligned carbon nanotube array (after [4.65])

substrate-based aligned CNTs are produced in a batch process using high temperatures that is not amenable to scalable production. Additionally, the limitations of many growth processes to specific substrates, such as alumina, have created roadblocks to the diverse applications envisioned for these materials. Recent efforts have made progress in growth of CNTs on conductive Cu substrates and at low temperatures [4.70], but a better understanding of the mechanisms behind CNT growth needs to be elucidated prior to large-scale advances in these areas. Fortunately, aligned CNT arrays have emerged as excellent test-beds to analyze the mechanistic aspects of CNT growth. Unlike most substrate-free CNT growth processes, aligned CNTs nucleate at virtually the same time and are uninhibited in many cases by significant steric hindrances that can alter the catalytic properties of randomly aligned materials. Therefore, one can use aligned CNT growth to probe quantitative and bulk-scale characteristics of the CNT growth and termination mechanisms that are relevant to all CNT growth processes.

4.3.3 Growth Mechanisms

The identification of specific mechanisms related to CNT growth remains controversial due to the wide variety of observations in growth processes that a single, unified mechanism would have to explain. However, it has been most readily accepted that CNT growth occurs via a vapor–solid–solid (VSS) model or a vapor–liquid–solid (VLS) model that has been readily employed for catalyst-based synthetic processes of other nanomaterials. In some cases for high temperature (> 900 °C) CNT growth, it is expected that the catalyst particles are in liquid phase whereas in lower temperature processes (< 700 °C) it is expected that catalyst particles

exist as a solid. It should be noted that the fast growth rates observed in CNT array growth can be modeled using diffusion parameters relevant to solids [4.71]. In these simple models, the hydrocarbon feedstock reacts with the catalyst particle and provides carbon that diffuses to the catalyst particle. In the initial phases of growth, a carbon cap precipitates on the surface of the particle and lifts off to result in CNT nucleation. Following nucleation, a constant carbon flux to the particle leads to the diffusion of carbon through the particle and to the edges of the growing CNT. In the simplest theoretical case, this becomes a steady-state system where a constant flux of carbon is supplied to the particle and the nanotube grows at a constant rate. However, from an experimental perspective, carbon nanotube synthetic processes terminate at some point, which is still not completely understood. This is believed to be a function of a process of *carbon overcoating* where amorphous carbon builds up on the catalyst particle and, over time, renders it inactive in growing CNTs. TEM studies have identified that morphology changes of the catalyst in the form of Ostwald ripening or other kinetic processes that occur due to the high free energy of catalyst nanoparticles and their exposure to the high temperature growth conditions may play a key role in termination processes as well, especially when the catalyst is supported by a solid surface [4.72].

Theoretical models of this process, one which is illustrated in Fig. 4.12, have been able to unify the interplay between multi-walled and single-walled CNT growth through the simple concept of carbon flux that

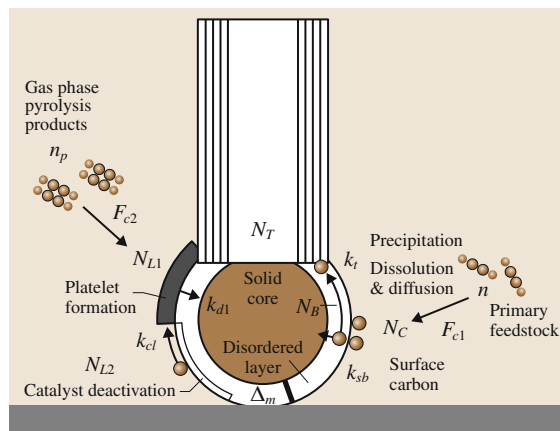


Fig. 4.12 Schematic showing the complex processes occurring during the catalytic growth of CNTs based on a model from Puretzky et al. (After [4.73])

is incident on the particle [4.71]. In a carbon starved environment (where the carbon flux is smaller than the diffusion rate), the result will be the nucleation of CNTs with only one wall whose outer diameter matches the particle size. Greater flux of carbon will result in the formation of multiple walls in the CNT. Whereas these ideas may oversimplify the challenges in understanding CNT synthetic processes, it is hoped that some unified model will emerge in the future that can establish a connection between the variable processes and systems used in CNT growth and the mechanisms that are at play in dictating nucleation, growth, and termination of CNTs.

4.4 Optical Properties

Because of their diameter-dependent direct band gaps, SWCNTs are promising for next-generation optoelectronic components. At the same time, their one-dimensionality is ideal for the study of 1-D excitons, whose properties remain largely unexplored despite predictions that they should behave very differently from excitons in higher dimensions [4.74, 75]. However, intrinsic optical properties of individual SWCNTs were difficult to probe for many years because of the effects of bundling and resulting tube-tube interactions in typical ensemble samples. During the past decade, much progress has been made in optical studies of SWCNTs, stimulated in part by the 2002 discovery of band gap photoluminescence (PL)

from individually suspended SWCNTs in aqueous solution [4.76]. These samples have created opportunities to perform spectroscopy of individual nanotubes of specific chiralities, allowing exploration of their intrinsic optical properties. PL excitation (PLE) spectroscopy [4.77–88], Raman spectroscopy [4.89–110], ultrafast optical spectroscopy [4.111–140], micro- and nano-spectroscopy [4.141–163], and magneto-optical spectroscopy [4.11, 15, 17, 156, 157, 164–170] of individualized SWCNTs are currently under investigation, revealing fundamental properties of 1-D excitons and phonons.

Due to the strong 1-D quantum confinement, photo-created electron-hole pairs form excitons, i. e., hydro-

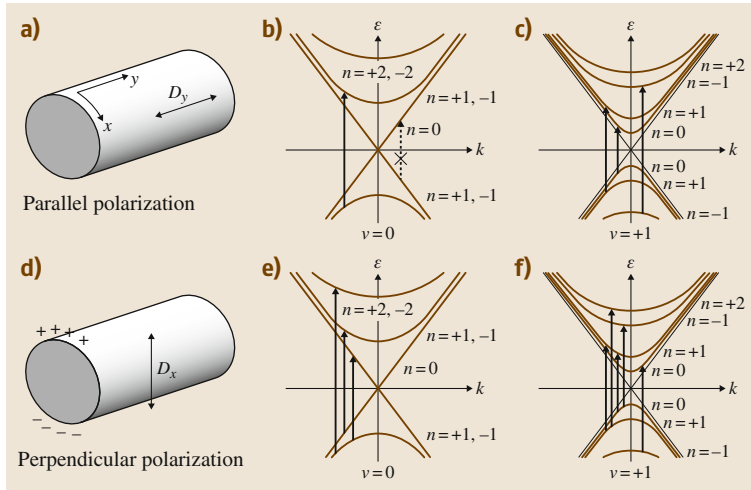


Fig. 4.13 (a–c) Incident light polarized parallel to SWCNT axis for a metallic SWCNT and a semiconducting SWCNT with allowed transitions indicated ($\Delta n = 0$). (d–f) Incident light polarized perpendicular to SWCNT axis for a metallic and semiconducting SWCNT with allowed transitions indicated ($\Delta n = \pm 1$). (After [4.23])

genic, Coulomb-bound electron–hole pairs [4.171]. In fact, in an ideal 1-D system, the binding energy of excitons has long been known to be infinite [4.172, 173]. Later, the binding energies of excitons in SWCNTs were experimentally determined to be hundreds of meV [4.174, 175], a significant fraction of their bare band gap, making SWCNTs one of the first systems in which to investigate excitons in the 1-D quantum limit.

4.4.1 Optical Absorption and Photoluminescence

Interband optical properties of SWCNTs arise from their structure-dependent attributes such as diameter and chiral angle as well as their electronic type (i. e., metallic or semiconducting). Therefore, optical spectroscopy provides a powerful tool for determining these attributes and their distributions in a given macroscopic sample.

First we will summarize the selection rules for interband absorption and emission in SWCNTs. If the photon momenta are small compared to the crystal momentum of the Bloch electrons, then approximate conservation of total linear momentum disallows *horizontal transitions*. Hence only *vertical transitions* are observed.

As in any solid, only vertical transitions are possible due to conservation of total linear momentum. This is because the photon momenta are small compared to the crystal momentum of the Bloch electrons. In the case of 1-D systems like SWCNTs, only transitions between states with nearly equal linear momenta along the tube axis are allowed. Since valence and conduction subbands in SWCNTs can be indexed by

their angular momentum along the tube axis [4.23] (Fig. 4.13), angular momentum conservation must be considered for optical absorption and emission. Light polarized parallel to the tube axis does not have any angular momentum, and thus only transitions between states having equal angular momentum (i. e., the same subband index) are allowed for this polarization. In contrast, light polarized perpendicular to the tube axis can impart angular momentum to the circumference of the tube. This is visualized by thinking of the equal mixture of right- and left-handed circularly polarized light that comprises this polarization configuration; left-handed (σ_-) light changes angular momentum by -1 and right-handed (σ_+) by $+1$. The perpendicular polarization, therefore, allows for transitions between states with a change in angular momentum of ± 1 . However, there is a strong depolarization effect for a perpendicular optical field [4.10, 176, 177], which suppresses absorption, making these optical transitions difficult to observe.

Experimentally, absorption spectroscopy is the simplest way to understand the basic characteristics of interband optical transitions in SWCNTs [4.76, 178–180]. Optical transitions occur between the valence and conduction bands, following the selection rules described before. The transitions are illustrated in Fig. 4.14. Because the transitions between states in the valence band vary in a precise way with the tube diameter in the optical regime, nanotubes were quickly identified as excellent candidates for optoelectronic applications. The interband transitions in SWCNTs reflect the underlying crystal symmetry of the nanotube. Since most synthesized SWCNTs have diameters ranging

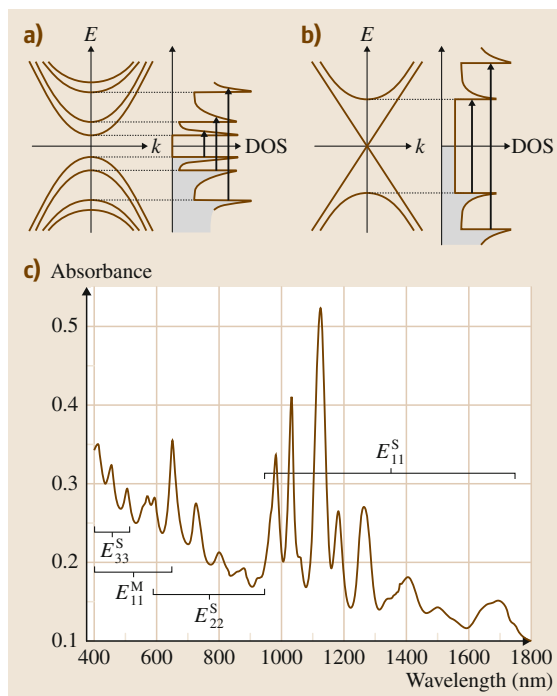


Fig. 4.14 Energy band diagram and density of states for (a) the E_{11} , E_{22} , and E_{33} transitions for semiconducting nanotubes, and (b) the E_{11} and E_{22} transitions for metallic nanotubes. The occupied states are expressed by the gray color. (c) Optical absorption spectrum of HiPco SWCNTs in a wide energy range from UV to IR. (Note that the first (second) of the subscripts of E_{ii} refers to the conduction (valence) subband index.) (After [4.8])

from 0.5 to 1.5 nm, the E_{11} and E_{22} transitions range from 800 meV to 3 eV. With increasing purity and individualization, higher-order transitions (up to E_{66}) have been observed, as well as phonon side-bands.

Figure 4.14c shows an optical absorption spectrum for HiPco SWCNTs, displaying four absorption bands:

1. E_{11} transition in semiconducting tubes
2. E_{22} transition in semiconducting tubes
3. E_{11} transition in metallic tubes
4. E_{33} transition in metallic tubes.

Within each band, there are multiple absorption peaks, coming from different (n, m) species present in the sample. It is therefore difficult to determine the (n, m) distribution quantitatively, unless the sample is highly enriched in a single (n, m) species. However, the intensity ratio between absorption peaks of metallic tubes and absorption peaks of semiconducting tubes

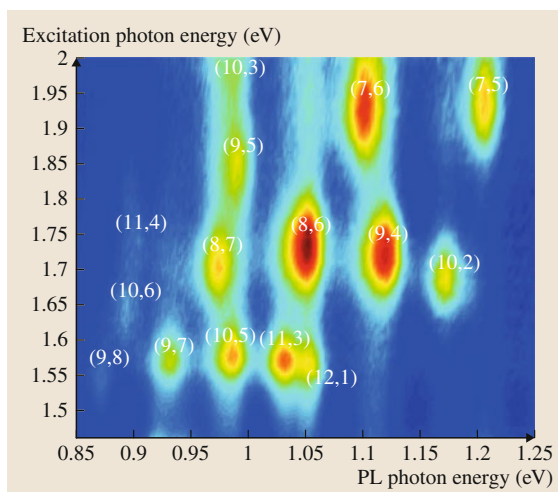


Fig. 4.15 Typical PLE map for HiPco nanotubes suspended in aqueous SDS. (After [4.8])

allows a qualitative estimate of the population ratio between these two types.

In the process of photoluminescence (PL), a high energy photon is absorbed by the medium and then a lower-energy photon is emitted. The excited state in a SWCNT can, in principle, be any high energy state or anywhere in the continuum, but due to enhanced absorption, a resonance appears when the E_{22} transition is excited and emission comes from E_{11} transitions. This effect was first observed in SWCNTs by O'Connell et al., and it quickly became one of the most common characterization tools for nanotube materials. In a typical PL experiment, the sample is excited by a range of visible wavelengths, and the luminescence is measured over a range of near-infrared wavelengths. Plotting the measured light intensity against the emission and excitation wavelengths creates a *photoluminescence excitation* (PLE) map (Fig. 4.15). Contrary to absorption spectroscopy, this technique is not useful for probing metallic (and small band gap) nanotubes but has the advantage of being sensitive enough to assign chiralities of semiconducting nanotubes, as illustrated in Fig. 4.15. It has proven to be ideal for measuring large quantities of materials, especially when combined with other spectroscopic tools (e.g., resonant Raman and absorption), and provides statistical information which cannot be obtained with electron microscopy. In addition, PL experiments have been used to obtain an understanding of excitonic states associated with the 1-D nature and the fourfold degeneracy of the electronic band structure of these semiconductors.

4.4.2 Raman Spectroscopy

As a consequence of their unique 1-D band structure, resonant Raman scattering spectroscopy serves as a powerful technique for the characterization and study of carbon nanotubes. A variant of normal Raman scattering, resonant Raman scattering (RRS) measures the intensity and energy of incident photons that are inelastically scattered off matter. The change in energy of the scattered photon relative to the energy of the incident photon corresponds to a quantum of the material under investigation, in this case a vibrational or phonon mode of an SWCNT. The resonant aspect of the technique comes from the use of excitation laser energies that coincide with real optical transitions of the SWCNT, resulting in a resonant enhancement effect that increases the Raman scattering probability from about 1 in 10^7 to approximately 1 in 10^3 . The unique combination of the resonant nature of this technique with the highly anisotropic structure of carbon nanotubes allows for unconventional uses of vibrational Raman scattering to provide information on bulk and individual mechanical, electronic, and solution properties of these materials. One specific advantage of RRS over other optical methods is its ability to examine both semiconducting and metallic types of SWCNTs, regardless of aggregation state, doping, or number of defects.

The most widely used and intense Raman-active vibrational modes used for studying and characterizing

carbon nanotubes are shown in Fig. 4.16. The lowest frequency mode ($\approx 100\text{--}400\text{ cm}^{-1}$) appears only in carbon nanotubes and fullerene structures and is known as the radial breathing mode (RBM) [4.181, 182] (Sect. 4.2.3). It is an isotropic stretching vibration occurring in the radial direction perpendicular to the tube axis. Since its frequency varies inversely with nanotube diameter [4.181], it serves as one of the most common methods for optically determining the tube diameter of a particular SWCNT species.

When such data is taken using a tunable laser source, the excitation energy dependence of specific RBMs can be determined. The energy at which the RBM Raman intensity reaches a maximum corresponds to the incident and scattered photon resonances with the SWCNT optical transition. As a result both diameter and optical transition energy can be determined from RBM Raman measurements allowing for assignment of RBM Raman features to specific (n, m) SWCNT structures [4.90–93, 97]. Once the optical transition energies are known for individualized SWCNTs, RBM intensity excitation profile data can be used to determine aggregation state [4.183] and even relative (n, m) abundance [4.109, 184–186].

The G-band vibration, centered at $1550\text{--}1600\text{ cm}^{-1}$, is another very intense vibration and is common to all sp^2 -hybridized carbon [1,2]. It is an in-plane, C–C stretching mode which is isotropic in graphene but anisotropic in carbon nanotubes due to the curvature-induced inequality of the two bond-displacement directions which causes the phonon to split into two, the G^+ and G^- peaks. Because of the splitting of the G-band into two separate but related modes, the overall line shape and intensity of the G-band can identify whether the tubes undergoing resonance with the excitation laser are metallic or semiconducting, as shown in Fig. 4.16 [4.103, 181, 187–190]. Furthermore, shifts in the G-band frequency can be observed due to doping via charge transfer resulting in the so-called *Eklund shift* [4.191]. With the application of uniaxial mechanical strain, the effective spring constants in each bond displacement direction can be further modified causing shifts in both G^+ and G^- frequencies as well as shifts in the observed optical transition energies, making the G-band a sensitive monitor of mechanical strain [4.192].

Another important mode is the D-band phonon, an out-of-plane bending mode with frequency 1300 cm^{-1} [4.181, 182]. This mode is normally Raman-inactive in pristine or perfect sp^2 -carbon due to symmetry considerations, however, when the translational symmetry of the extended structure of graphene, graphite, or a car-

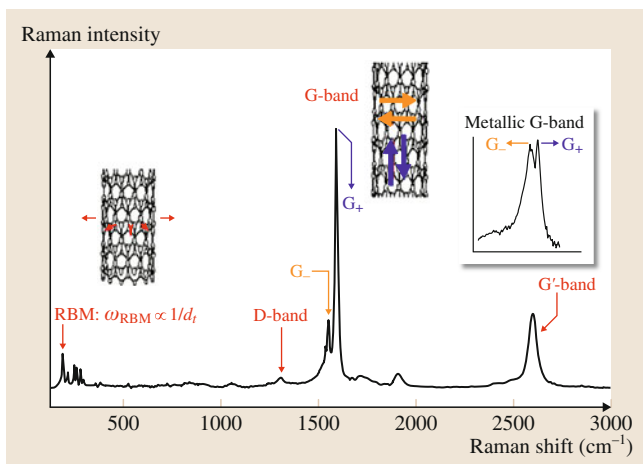


Fig. 4.16 A typical resonant Raman spectrum of a bulk SWCNT sample, taken at 785 nm excitation, for SWCNTs produced at Rice University. The spectrum illustrates the primary vibrational modes observed for SWCNTs, namely the RBM, D-band, G-band and G'-band

bon nanotube is broken by some sort of disorder, the D-band becomes Raman active and its intensity generally increases with the degree of disorder. This is why the D-band is often referred to as the *disorder* or *defect* peak in graphitic-like materials. This disorder can be actual bond dislocation defects, chemical functional groups, physisorbed molecular species, charge transfer complexes, etc., i. e., anything that can cause a localization of electron density in the otherwise delocalized π -bonding network.

Lastly, the G' -band ($2600\text{--}2700\text{ cm}^{-1}$), also common to all sp^2 -hybridized carbon, is a dispersive, second-order Raman mode highly sensitive to small changes in electronic and vibrational structure [4.182]. Specifically, the excitation dependence of the G' -band can be used to measure the dispersion of the optical transition under resonance, an important characteristic for understanding electronic band structure. Such *mapping* of the G' -band excitation profile allowed the first experimental confirmation of the trigonal warping effect in the electronic density-of-states [4.194].

Raman scattering provides information only about the crystal structure of carbon nanotubes. However, when combined with the resonance effect, the intensity of the scattered photons can provide quantitative information about the electronic, aggregation, chemical, and mechanical states of carbon nanotubes. Such information is invaluable to future research tasked with turning these molecules into macroscopic materials with tailor-made properties.

4.4.3 Resonant Rayleigh Spectroscopy

Resonant Rayleigh scattering or resonant elastic light scattering has recently become a popular tool for the optical study and rapid characterization of nanotube samples [4.195–197]. This technique can rapidly identify excited states in both metallic and semiconducting SWCNTs due to its high scattering intensity when combined with a broadband, tunable excitation source. *Sfeir* et al. [4.195] made initial observations of scattering peaks in the excitation spectra consistent with expected optical transitions for both semiconducting and metallic species. In particular, the excitation spectra of metallic SWCNTs exhibited peak splitting which were attributed to trigonal warping of the graphene Brillouin zone. In subsequent studies by *Sfeir* et al. [4.196] and *Berciaud* et al. [4.193], individual nanotubes were structurally identified using electron beam diffraction via transmission electron microscopy prior to Rayleigh scattering measurements, allowing a direct assignment of optical

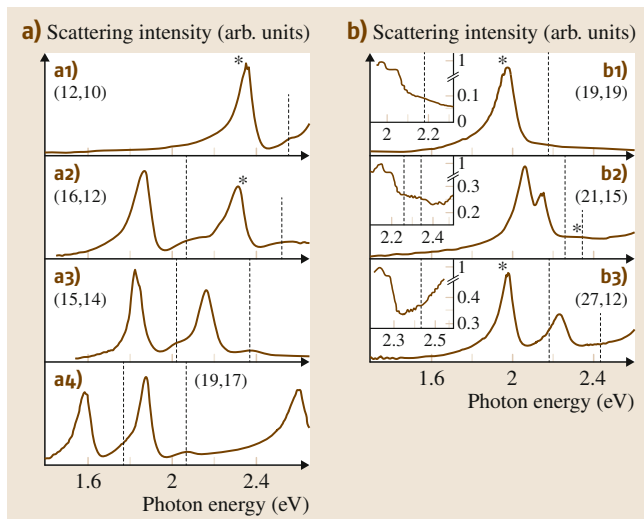


Fig. 4.17a,b Rayleigh scattering excitation spectra of (a) specific semiconducting and (b) metallic single-walled carbon nanotube chiralities. Vertical dashed lines indicate the energy position at which phonon sidebands are expected. Insets (b) are magnifications of the energy regions where phonon sidebands are expected, revealing no apparent feature. (After [4.193])

spectra obtained via resonant Rayleigh scattering to individual (n, m) species, as shown in Fig. 4.17. Semiconducting features were assigned to E_{33}^S and E_{44}^S excitonic optical transitions, while those of metallic SWCNTs were attributed to those of E_{11}^M . In addition, spectra of semiconducting SWCNTs show smaller, higher-energy features, located $\approx 200\text{ meV}$ above the main excitonic optical transition peak, attributed to phonon sidebands.

More recently, *Liu* et al. [4.197] combined electron beam diffraction with in situ Rayleigh scattering to measure 206 optical transitions of (n, m) -identified nanotubes. In particular, for nanotubes spanning diameters $1.4\text{--}4.7\text{ nm}$, optical transitions were measured for semiconducting species ranging from E_{33}^S up to E_{77}^S , and for metallic species ranging from E_{11}^M up to E_{33}^M . From this broad range of data collected via Rayleigh scattering spectroscopy along with existing E_{11}^S and E_{22}^S data collected via photoluminescence excitation spectroscopy, an empirical equation was produced to predict optical transition energies with appropriate (n, m) - and E_{ii} -dependent parameters, providing a predictive tool for assigning measured optical spectra to specific SWCNT chiralities over a broad range of experimentally relevant energies.

One particularly useful application of Rayleigh scattering spectroscopy is the wide-scale characterization of

many nanotubes simultaneously [4.198]. Using a wide-field laser illumination in a dark-field microscope geometry and refractive-index-matching, Joh et al. were able to Rayleigh image entire chips containing many different SWCNT species as a function of laser excitation energy. Combined with atomic force microscopy (AFM), this improvement in experimental setup allows not only the identification of nanotube growth but also the rapid determination of optical spectrum and diameter from Rayleigh scattering and AFM measurements, respectively, facilitating assignment to specific (n, m) structures [4.198].

4.4.4 Ultrafast Spectroscopy

Ultrafast spectroscopy allows the interrogation of carrier and phonon dynamics in condensed matter systems. As the rise and relaxation times of these ultrafast phenomena are on the order of 1 ps, they can be observed by using femtosecond laser pulses. One of the most popular tools for this is time-resolved pump-probe measurements. When a strong optical pump pulse from a femtosecond laser generates electron-hole pairs, the

concomitant changes in the properties of the material (e.g., Raman scattering, absorption, and reflectivity) are detected by a weaker probe pulse, and the delay is controlled by the experimenter.

Time-resolved pump-probe spectroscopy is a suitable method for measuring carrier dynamics, such as distribution functions and relaxation mechanisms. Using this method, one can explore carrier dephasing processes, carrier-carrier scattering, carrier-phonon scattering, and radiative and nonradiative recombination processes [4.111, 113, 115, 123, 199–202].

Figure 4.18 shows typical differential transmission ($\Delta T/T_0$) signals as a function of delay between pump and probe pulse. Two traces taken at 0.89 eV (1393 nm) and 1.60 eV (775 nm) correspond to E_{11} and E_{22} ranges, respectively. In both cases, a positive differential transmission is consistent with band filling, and the shorter decay time is explained by a nonradiative intraband relaxation process [4.203]. The slower decay time only found in the E_{11} range ($h\nu = 0.89$ eV in Fig. 4.18) can be explained as a radiative interband recombination, because the signal is resonantly enhanced when the photon energy is consistent with an interband absorption peak [4.111, 113, 200].

Coherent phonon (CP) spectroscopy is a powerful characterization tool, especially for SWCNTs. It allows direct measurement of excited state phonon dynamics in the time domain, including phase information and dephasing time. This information cannot be directly obtained via Raman spectroscopy. CP spectroscopy has several more advantages over Raman spectroscopy, including high resolution and narrow linewidths, no Rayleigh scattering, and no photoluminescence. Hence it allows characterization of metallic as well as semiconducting nanotubes, whereas PLE is incapable of characterizing metallic nanotubes.

Since the observation of coherent phonons in SWCNTs by Gambetta et al., many studies of the RBM and G-mode coherent phonons in SWCNTs have been published [4.129, 130, 134, 135, 137, 204, 205]. Figure 4.19a shows a coherent phonon oscillation signal in the time-domain [4.137]. To determine the frequencies of the excited lattice vibrations, one can perform a fast Fourier transformation (FFT) of the time-domain oscillations, such as is shown in Fig. 4.19b. The multiple peaks in the lower frequencies correspond to the RBM, which indicates that the SWCNT sample contains several chiralities that are resonantly excited at 840 nm (1.48 eV) [4.130]. Since the CP spectrum has high resolution, the peaks can be used to accurately determine the chiral index of the SWCNTs [4.206].

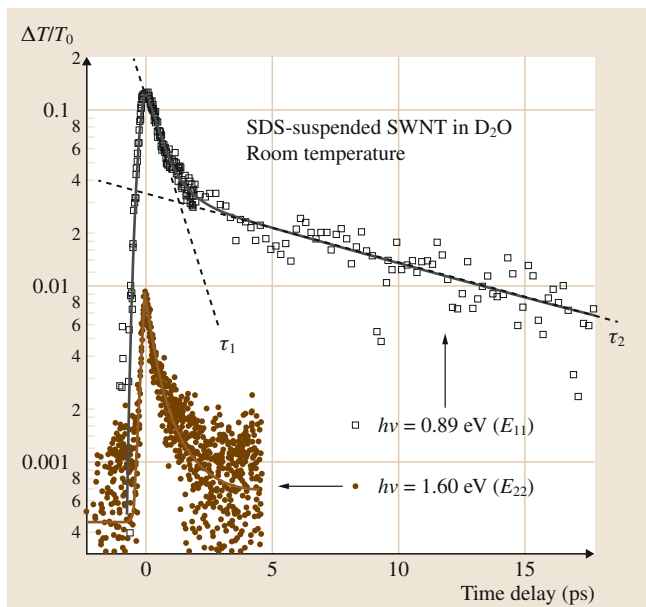


Fig. 4.18 Ultrafast pump-probe data at two wavelengths, corresponding to first and second subband transitions. A very fast single decay is seen in the second subband case while two decay components ($\tau_1 \approx 770$ fs and $\tau_2 \approx 10$ ps) are clearly seen in the first subband case. Solid lines show Gaussian and exponential fits in the appropriate delay regimes. (After [4.113])

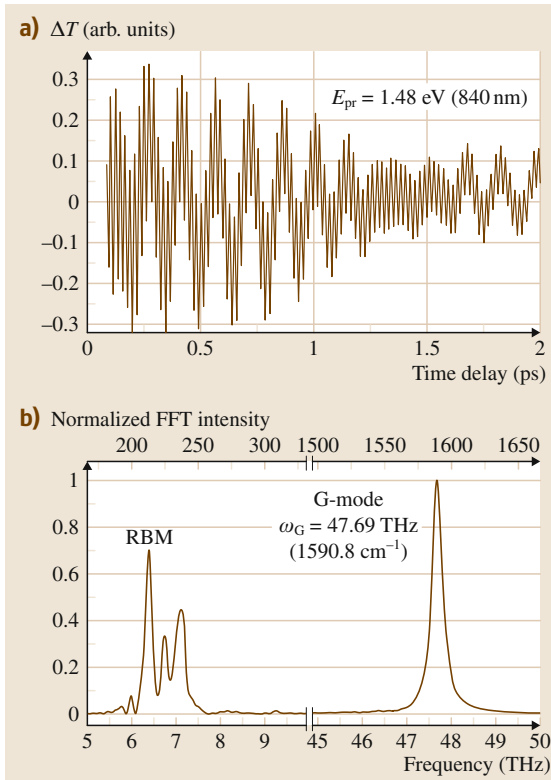


Fig. 4.19 (a) Transmitted intensity modulations due to coherent phonon oscillations in SWCNTs, which were extracted from the pump-probe signal for pump and probe energies of 1.55 eV (800 nm, E_{pu}) and 1.48 eV (840 nm, E_{pr}), respectively. The beating pattern arises from superposition of the CP oscillations from the RBM and G-mode. (b) Corresponding Fourier-transformed spectrum showing radial-breathing modes (RBMs) at 6.0–7.5 THz (200–250 cm^{-1}) and G-mode phonons at 47.69 THz (1590.8 cm^{-1}). (After [4.137])

The peak at 47.69 THz (1590.8 cm^{-1}) corresponds to G-mode phonons of SWCNTs. With regard to the G-mode, Kim et al. recently presented a clear picture for the dephasing of G-band phonons by random frequency modulation via interaction with the RBM through anharmonicity [4.136, 137].

Using a pulse-shaping technique [4.207], chiral-selective excitation has been achieved for studying the physical properties of single-chirality SWCNTs [4.134]. Figure 4.20a shows typical CP oscillations (Fig. 4.20a, left) and their Fourier transformed spectrum (Fig. 4.20a, right). By introducing multiple pulse trains with different repetition rates (7.07–6.15 THz), a coherent

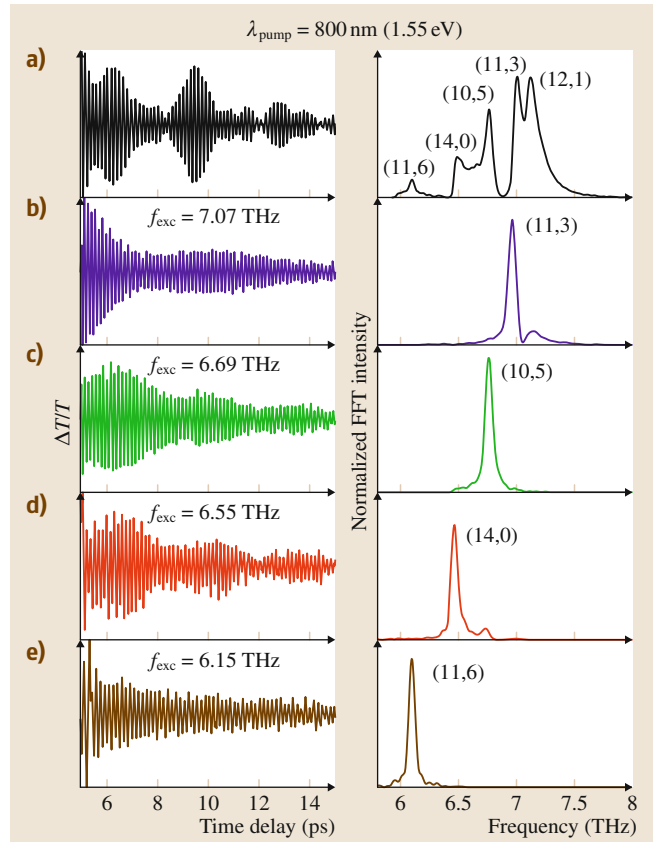


Fig. 4.20 (a) Left: time-domain transmission modulations of the probe due to coherent RBM vibrations in ensemble SWCNT solution generated using standard pump-probe techniques without pulse shaping. (a) Right: Fourier transformation of time-domain oscillations with chirality-assigned peaks. (b–e) Left: time-domain coherent RBM oscillations selectively excited by multiple pulse trains via pulse shaping with corresponding repetition rates of 6.15, 6.55, 6.69, and 7.07 THz. (b–e) Right: Fourier transformations of corresponding oscillations, with their dominant nanotube chirality (n, m) indicated. (After [4.134])

RBM oscillation is selectively excited, as shown in Fig. 4.20b–e, respectively. For instance, by choosing a pump repetition rate of 7.07 THz, the (11,3) nanotubes can be excited selectively, as shown in Fig. 4.20b. Note that the accuracy of selectivity depends on the number of pulses in the tailored pulse train.

4.4.5 Excitonic Effects

1-D Coulomb interaction differs significantly from systems with other dimensions. For example, the ex-

citon binding energy becomes infinite in an ideal 1-D electron-hole system [4.172, 173, 208]. In addition, the Sommerfeld factor, the ratio of the exciton continuum to the free electron-hole pair above the band edge, has been shown to be less than 1 in 1-D systems [4.74, 75]. 1-D excitons in SWCNTs [4.209] seem to be even more peculiar. Early experimental PLE results (e.g., [4.80]) indicated that interband excitation energies are *higher* than those expected from band structure calculations based on simple tight-binding models. This blue shift is totally against our conventional wisdom that excitonic binding should red shift the excitation energy from the band edge. Ando's pioneering theoretical work [4.210, 211] indicates that there is a significant blue shift from the single-particle band gap (which is what tight-binding calculations yield) due to quasi-particle corrections. This blue shift is expected to exceed the excitonic binding energy, and thus, the net effect is a blue shift. A number of more recent theoretical studies [4.177, 212–229] not only confirmed these predictions and provided estimates for the exciton binding energies but also raised an array of new issues, questions, and predictions, including the intrinsic radiative lifetimes, the existence of *dark* excitons, and the stability of excitons in metallic carbon nanotubes. Two-photon PLE studies [4.174, 175] have successfully determined the exciton binding energies to be very large (300–500 meV). Excitonic signatures have also been detected in absorption spectra of metallic nanotubes [4.180]. Furthermore, recent temperature-dependent magneto-optical studies have provided new insight into the excitonic fine structure in SWCNTs [4.165–169], including the direct measurement of dark-bright splitting values in individual SWCNTs [4.156, 157].

The existence of two equivalent valleys in momentum space, K and K' valleys, combined with strong short-range Coulomb interactions (intervalley mixing and exchange), produces an intriguing excitonic fine structure in SWCNTs [4.223, 231]. There are four combinations of lowest-energy excitons: two are direct excitons formed by linear combinations of KK and $K'K'$ electron-hole pairs and two are indirect excitons that are created by indirect $K'K$ and KK' electron-hole pairs. The latter are finite momentum exciton states that require a phonon-assisted transition to be optically created. Direct excitons are zero momentum states, which facilitates optical absorption and emission. However, the mixing of the KK and $K'K'$ transitions produces two wavefunctions that have opposite parity under transformations about the axis perpendicular to the tube

(sometimes referred to as the U symmetry axis). The lower (s -like, often called the $1g$ state) exciton state has even symmetry, while the upper state (p -like, $1u$ state) has odd symmetry. Since a photon will only couple with a state with odd parity (system overall has even parity), the upper state is optically active (*bright*) and the lower state is inactive (*dark*), which is a unique scenario whereby the lowest state is not the emissive one [4.214, 217, 219, 221–223, 231]. The $n = 2$ orbitals of the E_{11} exciton reverse the ordering of even and odd symmetry, such that the $2u$ (odd symmetry) has a lower energy than the $2g$ (even) state.

Experimentalists have exploited these symmetry-based transition rules to investigate SWCNT excitons. Since only the $1u$ exciton state couples to the light field by way of one photon, and $2g$ couples only using two photons, one can excite one-photon dark states and monitor the $1u$ luminescence (Fig. 4.21) [4.174, 175]. Using the difference between the excitation energy for E_{11}^{2g} and the emission energy of E_{11}^{1u} and assuming

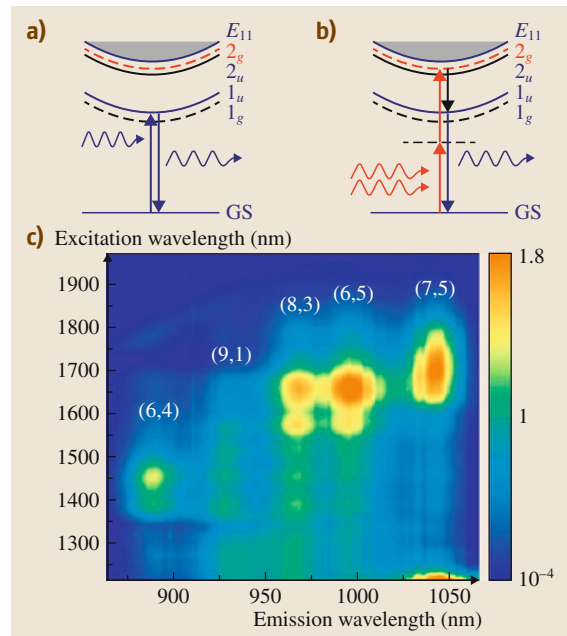


Fig. 4.21 (a) One photon can couple to the $1u$ state both as an excitation and emission. (b) Two photons can access even parity states, like $1g$ or $2g$. In two-photon spectroscopy, two photons excite a dark state while the bright, luminescent $1u$ state is monitored. (c) Experimental contour map of the PL intensity as a function of two-photon excitation (y-axis) versus one-photon emission (x-axis). (After [4.230])

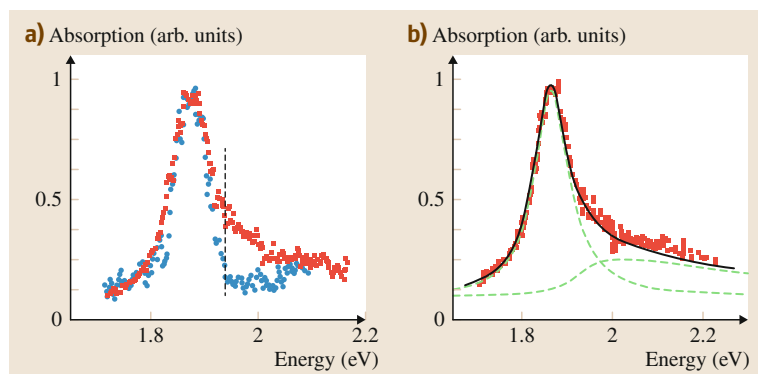


Fig. 4.22 (a) Absorption spectrum of a (21,21) metallic nanotube (red symbols) and a (16,15) semiconducting SWCNT (blue symbols), after a slight shift in energy and adjustment in strength. In the armchair nanotube, absorption from the continuum transitions is apparent in the high-energy wing. From the threshold of the continuum absorption (dashed line), we estimate an exciton binding energy of 50 meV. (b) Comparison of the theory (black solid line) for the optical transition in a metallic nanotube. The absorption can be decomposed into the dominant exciton contribution and a continuum contribution (green dashed lines). (After [4.233])

a hydrogenic model, the exciton binding energy was estimated to be ~ 300 to 400 meV for $0.6 < d_t < 0.9$ nm SWCNTs and showed a linear dependence on the inverse of the diameter [4.232]. Furthermore, the tubular nature of SWCNT crystal structure allows a magnetic field applied parallel to the tube axis to induce non-intuitive quantum phenomena. Such a magnetic field breaks time reversal symmetry and adds an Aharonov–Bohm phase to the electronic wavefunction, which mixes the lowest-energy bright and dark exciton states. In particular, a series of recent experiments [4.156, 157, 165–169] demonstrated that such a symmetry-breaking magnetic field can dramatically *brighten* the dark state. Namely, the PL intensity increases, or *brightens*, with magnetic field and the amount of brightening decreases with temperature. This phenomenon, magnetic brightening, can be understood as a consequence of interplay between the strong intervalley Coulomb mixing and field-induced lifting of valley degeneracy.

Contrary to the situation of semiconducting SWCNTs, excitonic properties of metallic SWCNTs have been poorly explored [4.186], although they are expected to provide a novel system for the study of electron–hole pairs in the presence of degenerate 1-D

electrons. Unlike *conventional* 1-D metals, the lowest van Hove singularity (VHS) peak in the conduction-band is unoccupied in metallic SWCNT, allowing one to create excitons into an interacting 1-D electron system by resonantly pumping the lowest 1-D VHS peak. The created excitons should show unique dephasing and energy relaxation dynamics, the correct understanding of which should provide significant new insight into many-body dynamics in femtosecond time scales. Screening does take place in metallic SWCNTs, but only weakly, allowing for exciton binding energies to reach 50 meV, as measured by direct optical absorption of a single metallic SWCNT [4.233], shown in Fig. 4.22. Unlike graphene, transitions in metallic SWCNTs cannot occur between the linear bands that form the Dirac cone at K and K' , as discussed earlier. Instead, like semiconducting SWCNTs, the lowest allowed transition occurs between the highest valence van Hove singularity the lowest conduction one. This transition is heavily modified by the large exciton binding energy creating Lorentzian-like transitions that are similar to the semiconducting SWCNTs. Since the absorption is from excitons and not a free plasmon resonance like most metals, metallic SWCNTs scatter the visible light that they do not absorb [4.234].

4.5 Transport Properties

Electronic transport properties of carbon nanotubes were studied intensively very soon after their discovery. A wide variety of CNT systems have been studied, including ropes, networks, and films. Numerous effects typical of polymer matrices, classical crystals, and disordered materials have been observed in these bulk

systems. Some of the key parameters governing transport are the sample quality and the nature and number of nanotube–nanotube and nanotube–electrode junctions. In this section, a brief presentation of nanotube films is given to illustrate the complexity induced by the combination of these parameters; the main part is dedicated

to individual nanotubes, where a better understanding has been achieved, to illustrate the strong distinction between metallic and semiconducting nanotubes and some of the most important parameters to describe their device operation.

SWCNT films or *mats* are formed by randomly or partially oriented *SWCNT* bundles. In some respects, such a network is similar to an amorphous metal system with conductive tubes or bundles as the metallic islands separated by energy or spacial barriers. As a result, the *DC* transport is primarily determined by intertube transport within bundles or interbundle transport, while the *1-D* intratube transport nature is buried [4.235].

The *DC* conductivity of *SWCNTs* is metallic at high temperatures, increasing linearly with decreasing temperature [4.236]. However, at lower temperatures, the *DC* conductivity reaches a maximum and starts to decrease with decreasing temperature. Such non-metallic behavior is usually explained by either variable range hopping (*VRH*) [4.237, 238] or fluctuation-induced tunneling (*FIT*) [4.239, 240]. But it is still not clear whether such behavior is mainly due to weak interbundle connections, localization by impurities, defects, or frozen semiconducting tubes within bundles [4.235]. Other experimental techniques such as magnetoresistance measurements [4.237, 238] and *AC* conductivity measurements [4.241, 242] are also used to explore the transport mechanism in *SWNT* films.

Studied as *individual nano-objects*, both metallic and semiconducting nanotubes have provided much insight and are still explored as both ideal one-dimensional mesoscopic systems [4.243–246] and potential building blocks for electronic applications [4.247–251]. Metallic nanotubes have charge carriers with very high mobilities near the Dirac point, and current densities as high as 25 μA can be carried by a single nanotube [4.252], making them much larger than copper for the same cross-section. Moreover, due to the strong Coulomb interaction in one-dimensional metals, electron–electron correlations become important and their properties become described by the Tommonaga–Luttinger liquid model [4.253]. On the other end, the chirality dependence of semiconducting nanotube band gaps have allowed to study many device properties ranging from single-electron transistors [4.254] to Schottky [4.255] and p-n diodes [4.251] and are showing a very high sensitivity to the environment or external excitations (optical, magnetic) expected to give rise, combined with their mechanical strength, to highly robust detectors.

In most of the numerous reports in the literature, individual nanotubes are directly contacted by two metallic electrodes and a third nearby electrode is used to apply an electrostatic field (Fig. 4.23), as proposed since the first transport measurements in 1997 and 1998 [4.243, 247–249]. This three-terminal (transistor) configuration allows the direct determination of the metallicity of the nanotubes (Sect. 4.2.2) by measuring the resistance or current-voltage characteristics of the device as a function of the potential applied through the third electrode (called gate). The detailed fabrication procedure varies a lot depending on the expected outcomes: devices are obtained by either depositing nanotubes from dispersions or directly growing them on a substrate; electrodes can be deposited on top of the nanotubes, or they can lie on top of them; typically the substrate is highly-doped silicon (which will be used as the gate electrode) over which a thermal oxide is grown (Fig. 4.23); as a consequence, the *SWCNT* can be suspended or directly in contact with the substrate.

Most basic electronic properties can be clarified by considering the effect of an external potential to the doping level of the nanotube, and the transport characteristics of a *1-D* system. This second aspect can be given by the Landauer formula of the two terminal resistance [4.256]. The two-terminal conductance of a *1-D* system, is given by

$$G = \frac{4e^2}{h} \sum_i \int \bar{T}_i(E) \left(-\frac{\partial f[(E - E_F)/k_B T]}{\partial E} \right) dE, \quad (4.6)$$

where the total conductance is given by the sum at the Fermi energy E_F of all subbands with index i of transmission $\bar{T}_i(E)$, and $f(E)$ is the Fermi distribution. The prefactor 4 is due to the subband spin and orbital degeneracies.

The modulation of the nanotube doping by the gate voltage can be obtained by considering the electrostatic equilibrium at a given gate potential. The carbon nanotube is capacitively coupled to the gate electrode and charges are injected in both of them. This charge injection will induce a change in the electrochemical potential of the nanotube through a density-of-states term [4.257, 258] and can be expressed as (for low source–drain voltage and neglecting temperature broadening)

$$E_F = eV_g - e^2 \frac{\int_0^{E_F} \rho(E) dE}{C_g}, \quad (4.7)$$

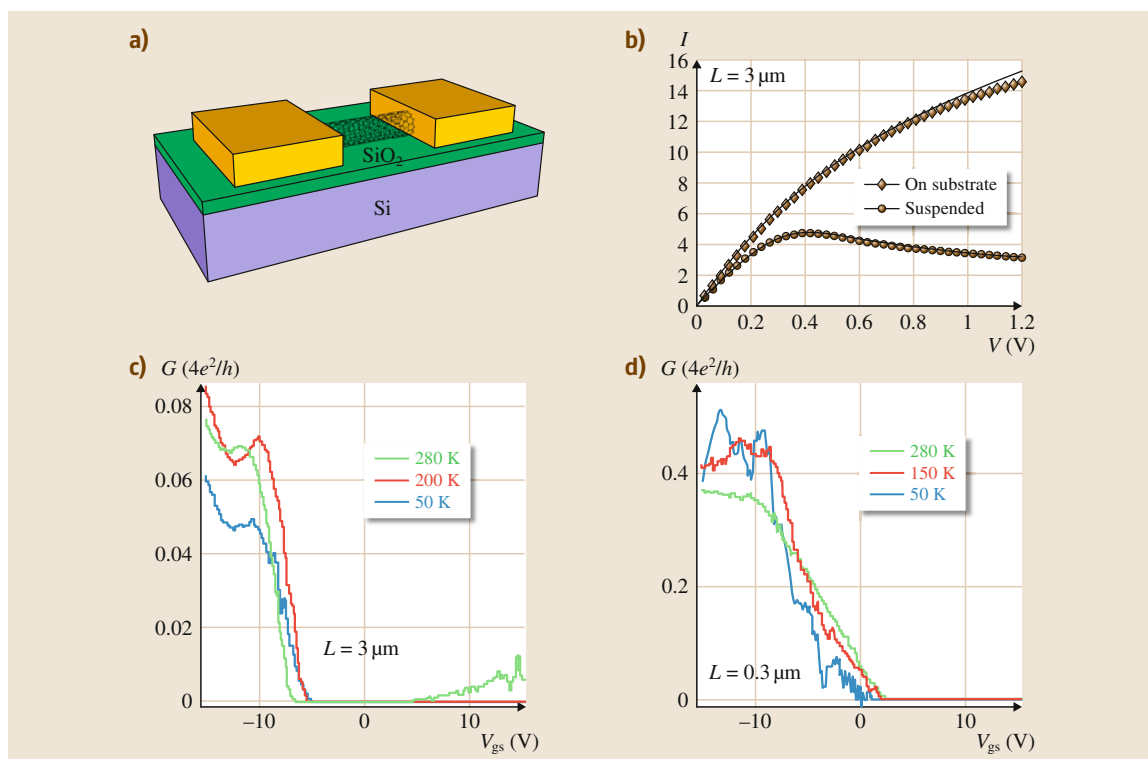


Fig. 4.23 (a) Schematic of the typical transistor configuration used to measure individual carbon nanotube transport properties. (b) $I(V)$ characteristic at high voltage of a long carbon nanotube device with comparison between a nanotube on substrate and suspended. (After [4.252]). (c) Conductance G (at low source-drain bias V_{ds}) versus gate voltage V_{gs} for a $3 \mu\text{m}$ long SWCNT device recorded at various temperatures. (d) G versus V_{gs} for a 300 nm long tube section on the same tube as for (c) at various T . ((c,d) after [4.245])

with V_g the potential applied between the gate and the source-drain electrodes, C_g the electrostatic (geometric) capacitance and $\rho(E)$ the density of states integrated from the center of the band gap (or the Dirac point) to the Fermi energy. In this specific expression, the Dirac point is assumed to be at $V_g(E_F = 0) = 0 \text{ V}$. However, in most devices, due to charge traps and doping from the oxide or impurities, an hysteresis in the gate dependence [4.259] and a threshold voltage ($V_g(E_F = 0) = V_{th}$) will appear [4.260, 261].

From these two equations, one can see that the conductance depends on the transmission of electrons through the whole device at the Fermi energy controlled by the gate voltage. Hence, different nanotubes will exhibit clear gate dependencies even at room temperature:

- Semiconducting nanotubes will exhibit field-effect transistors type behaviors with on/off ratios of many orders of magnitude, since there is no subband

available near E_F . They will exhibit diode type current-voltage characteristics. The most common reported behavior is unipolar with a p-doping of the nanotube attributed to adsorbates on the nanotube surface [4.249] (Fig. 4.23c,d) and effects from the substrate (or the electrodes); however, ambipolar devices are now commonly achieved [4.262].

- The small band gap carbon nanotubes will only show a small dip, since the band gap energy is comparable to the thermal energy and the tails of the Fermi distribution are within the valence or conduction band.
- Metallic nanotubes will only show very weak (or no) gate voltage dependence since they will be less sensitive to the gate voltage (due to finite density-of-states everywhere) and the number of subbands will remain constant over a large energy range; and they typically exhibit linear $I-V$ curves before saturation.

The various transport regimes described by (4.6) are governed by the transmission of the whole device including the tube, but also the contacts. The minimum conductance is then given by the ballistic regime where $\bar{T}_i(E) = 1$ and gives a quantized conductance of $G_{\text{bal}} = \frac{4e^2}{h}$ for each subband. This corresponds to a resistance of 6.5 k Ω . At room temperature, additional resistance is due to incoherent addition of nonperfect contact transmission and diffusive centers in the nanotube, this is the *classical regime*. At low temperature, coherent effects dominate and quantum dot regimes or localization effects develop; these regimes are referred as *quantum transport* or *mesoscopic regimes*. Ballistic resistance has been demonstrated for metallic carbon nanotubes up to room temperature [4.244, 263], whereas semiconducting nanotubes do not exactly reach this value [4.245, 263] (Fig. 4.23c,d).

Impressive progress has been made in the understanding and reduction of the contact contribution to the resistance. Different metals have been used to contact nanotubes with the most common being gold, titanium, palladium and platinum. A first barrier can form at the interface between the metal and the nanotube due to bad wetting of the nanotube in the metal; this interface will be governed by the cleanliness and contaminations of the interface and by the overlap between the metal-nanotube wavefunctions [4.28]. A low, ohmic contact resistance is typically obtained by using top electrodes made of palladium or gold and/or by annealing the device. Another route to achieve near perfect contacts consists in direct growth on top of the contacts [4.245], or using nano-welding (*burying* the nanotube in the contact). Moreover, in the case of semiconductors, even with a good interface a Schottky barrier can form depending on the band alignment [4.255, 264]. The matching of the metal and nanotube work function has been shown to provide a good approximation of this barrier height, although charge transfer at the interface must be considered for a precise understanding. These barriers have been shown to govern the field-effect properties of nanotube transistors and yield to a very high sensitivity of these devices to the environment. As an example, a good p-type contact will be obtained for a metal with a high work function, but a good interface is also necessary. As a consequence, titanium will be a bad choice due to its work function lying in the center of the nanotube band gap, but platinum also, due to a poor contact and the formation of additional barriers; whereas palladium will satisfy both conditions.

Obviously, the intrinsic resistance of the nanotube will also contribute to the overall measured value. In the

classical case, the two main contributions come from scattering by disorder and phonons. The origin of disorder is often complex to assign and scattering can be due to lattice defects (vacancies, impurities, ...), mechanical deformations and potential fluctuations induced by adsorbates and the substrate [4.261]. A backscattering mechanism can be distinguished between intervalley (from K to K') or intravalley scattering and will be associated with short-range and long-range disorder, respectively. It has been theoretically [4.261] shown that metallic nanotubes are insensitive to the first type of scattering and they exhibit lower intrinsic resistance than semiconducting nanotubes. Scattering will also occur with acoustic phonons at low source-drain bias. In metallic and clean (doped) semiconducting nanotubes the I - V curves are linear at low-bias; and mobilities higher than 100 000 cm²/(V s) and ballistic transport for short distance between contacts have been demonstrated [4.244, 252, 263]. At higher voltage, the resistance will start saturating due to interaction with optical phonons (around $\hbar\omega_0 \simeq 160$ meV) and the maximum current carried by a single tube will be as high as 25 μ A (Fig. 4.23b). For suspended nanotubes, a negative differential conductance can even be observed due to heating induced by hot phonons (Fig. 4.23b). This higher current limit can be overcome only for contact distances shorter than the optical phonon mean-free path around 10 nm [4.265].

At lower temperature, coherent addition of the scattering contributions and coherent transmission at the electrode interface must be considered. Moreover, the effect of confinement and electron-electron interaction becomes important and some of these effects might even need to be considered up to room temperature. A large variety of phenomena have been observed depending on the metallicity, the transmission at the contacts and the nature, density and strength of the scattering centers in the nanotubes. Detailed reviews provide an extensive description of such quantum phenomena from both the theoretical [4.28, 261] and experimental point of views; we can summarize some of the consensus achieved by dividing these mesoscopic results in three main effects:

- Correlated electrons in 1-D metals are not described by a Fermi liquid of weakly interacting fermions, but as a correlated ground state called a *Luttinger liquid*. Spin and charge propagate as two independent bosonic modes and different power law dependencies of the tunneling density of state and conductance are expected. This law will depend on

the bias voltage range, temperature, the nature of the contacts (to the end or the bulk of the nanotubes) and will depend on the Luttinger liquid parameter, $g \approx 0.22$ for SWCNTs [4.36, 266]. Although such measurements are difficult to assign univoquely, experimental power laws have been demonstrated to be consistent with theory [4.253, 267].

- When the presence of scatterers becomes too important, the mean-free path is given by static scatterers; as the temperature decreases the coherence length increases and coherent back-scattering takes place: this is the so-called *localization regime*. Both weak and strong localization can occur depending whether disorder or electron interactions dominate. Magneto-resistance measurements allow unique assignment of these regimes, and, in the case of individual SWCNTs, weak localization is intimately related to Luttinger liquid behaviors; this is not the case for small bundles or MWCNTs, where Fermi liquid behaviors are observed.
- When no (or very few, weak) scattering centers are present, the coherent response is dominated by the reflection and transmission at the contacts. The behavior can vary from *Coulomb blockade* [4.243, 247, 269], where nanotubes behave like single-electron transistors when contacts are transmit poorly, to *Fabry–Perot type* interferences [4.244, 263], where the system behaves like an electron waveguide when contacts are almost transparent. Both regimes are characterized by very strong oscillations of the conductance, as illustrated in Fig. 4.24. In the first case, the finite length of the nanotube induces a supplementary quantization of the wavevector and forms of a zero-dimensional system (right inset), while in the second case, constructive and destructive interferences of the wavefunction occur (left inset). Interestingly, in both cases, the induced wavevector quantization is given by $\Delta k = \pi/L$. The quantum dot regime exhibits more complex V_g and V_b dependency due to degeneracy lifting induced by the mutual interaction between added charges leading to spin-orbit coupling. Magnetoresistance measurements have been very useful to probe such effects in detail [4.269].

One of the current challenges in the field consists in exploiting the properties of single nanotube devices to

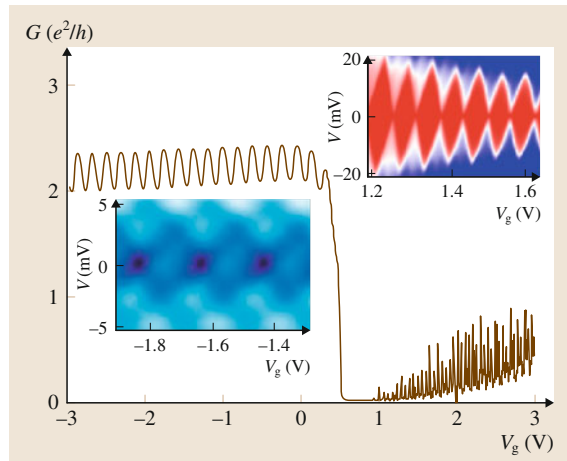


Fig. 4.24 Gate dependent conductance of a suspended, ultra-clean small band gap carbon nanotube at $T = 300$ mK. The almost transparent contacts in the p-doping regime exhibits a Fabry–Perot pattern. *Left inset*: shows conductance while varying bias and gate voltage (dark blue: $2e^2/h$, bright white: $4e^2/h$). In the *n* doping regime, Schottky barrier and lower transmission at the contacts induce a Coulomb blockade regime. *Right inset*: Coulomb diamonds. (After [4.268])

large-scale applications and much progress has been made in building more and more complex structures using individual nanotubes, and also controlling bulk samples by using for example aligned growth or chirality sorted films. These structures have been exploited in numerous configurations and for various applications. For example, large-scale logic and analog electronic structures, microwave and radio-frequency operation, proximity effects from superconducting or ferromagnetic electrodes have been demonstrated. It is also worth noticing that transport measurements have also been coupled with other experimental configurations and a very rich literature has also arisen regarding photovoltaic detection and electroluminescence, nano-electromechanical resonators, and scanning tunneling spectroscopies. All this has contributed to a deeper understanding of the mechanisms described above, but also demonstrated the wide range of potential applications of carbon nanotube especially for (mass or chemical) sensors and optoelectronics [4.8, 270].

4.6 Thermal and Mechanical Properties

Since their discovery, it has been expected that **SWCNTs** would have remarkable thermal and mechanical properties. This is because of the hexagonal arrangement of carbon atoms and the nature of the sp^2 carbon bond. We will first present a brief introduction to the basic thermal properties of carbon nanotubes and then describe their mechanical properties, where a much larger consensus has been achieved.

4.6.1 Thermal Properties

Specific Heat

The specific heat C_v of graphite arises from phonon and electronic contributions as

$$C_v = C_{ph} + C_{el}. \quad (4.8)$$

The phonon contribution to the specific heat can be calculated by

$$C_{ph} = \int_0^{\omega_{\max}} k_B \left(\frac{\hbar\omega}{k_B T} \right)^2 \frac{\exp\left(\frac{\hbar\omega}{k_B T}\right) \rho(\omega)}{\left[\exp\left(\frac{\hbar\omega}{k_B T}\right) - 1 \right]^2} d\omega, \quad (4.9)$$

where $\rho(\omega)$ is the phonon density of states and ω_{\max} is the highest phonon energy of the material. For $T \ll \Theta_D$ (where Θ_D is the Debye temperature), only acoustic phonon modes are populated. If an acoustic phonon mode in d -dimensions follows an $\omega \propto k^\alpha$ dispersion, then according to (4.9), the corresponding specific heat should obey $C_{ph} \propto T^{d/\alpha}$ [4.47].

Figure 4.25a highlights the low frequency phonon modes of **SWCNTs** [4.37]. All acoustic phonon modes show linear dispersion and high phonon velocities. For example, for a (10,10) tube, $v_{LA} = 24$ km/s, $v_{TA} = 9$ km/s, and $v_{twist} = 15$ km/s. Thus, for each acoustic phonon mode, C_{ph} shows a linear relation to temperature given by [4.271]

$$C_{ph} = \frac{\pi k_B^2 T}{\hbar v_{ph} \rho_m}, \quad (4.10)$$

where ρ_m is the linear mass density and v_{ph} is the phonon speed.

The electronic contribution to C_v can be evaluated by [4.271]

$$C_{el} = \Omega \int_0^\infty (E - E_F) \frac{df}{dT} N(E) dE, \quad (4.11)$$

where f is the Fermi–Dirac function and Ω is the d -dimensional volume. For undoped metallic **CNTs**, $N(E)$ is a constant below the first van Hove singularities which implies that C_{el} also linear with temperature for $T \ll \hbar v_F / k_B R$:

$$C_{el} = \frac{\pi k_B^2 T}{\hbar v_F \rho_m}, \quad (4.12)$$

where v_F is the Fermi velocity. According to (4.10) and (4.12), the ratio between C_{ph} and C_{el} is

$$\frac{C_{ph}}{C_{el}} \approx \frac{v_{ph}}{v_F} \approx 10^2. \quad (4.13)$$

As a result, the electronic contribution to the specific heat can be ignored. For an undoped semiconducting **SWCNT**, C_{el} is even smaller and should decay more rapidly with decreasing temperature. However, if the tubes are doped above the van Hove singularity, then C_{el} could be significantly enhanced.

Figure 4.25b shows the measured heat capacity of **SWCNTs** with a highlight of their low temperature behavior [4.272]. The temperature dependence is also compared with other carbon materials. Briefly, the heat capacity of **SWCNTs** is smaller than graphene due to the reduction of density of phonons by *subband* splitting (see Fig. 4.25a inset). On the other hand, it is higher than graphite, whose low frequency phonons are further quenched by graphite inter-layer interactions. However, this discrepancy is amended when **SWCNTs** are tightly bundled due to the inter-tube bundling effect (Fig. 4.6). The low temperature behavior of the heat capacity could be well fitted by taking into account this bundling effect and also the lowest subband mode contribution (Fig. 4.25c). The fitting parameters are also close to the theoretically calculated phonon spectrum.

Thermal Conductivity

In this section, we will only consider diagonal elements of the thermal conductivity matrix

$$\kappa_{zz} = \sum c v_z^2 \tau, \quad (4.14)$$

where c is the specific heat, v_z is the group velocity, τ the relaxation time of a given phonon state, and the sum is over all phonon states. For $T \ll \Theta_D$, the relaxation time is determined by scattering off impurities, defects, and sample boundaries, and is roughly constant. Therefore the low-temperature thermal conductivity should follow the same temperature dependence as the specific heat. But due to the weight factor $v_z^2 \tau$, certain phonon

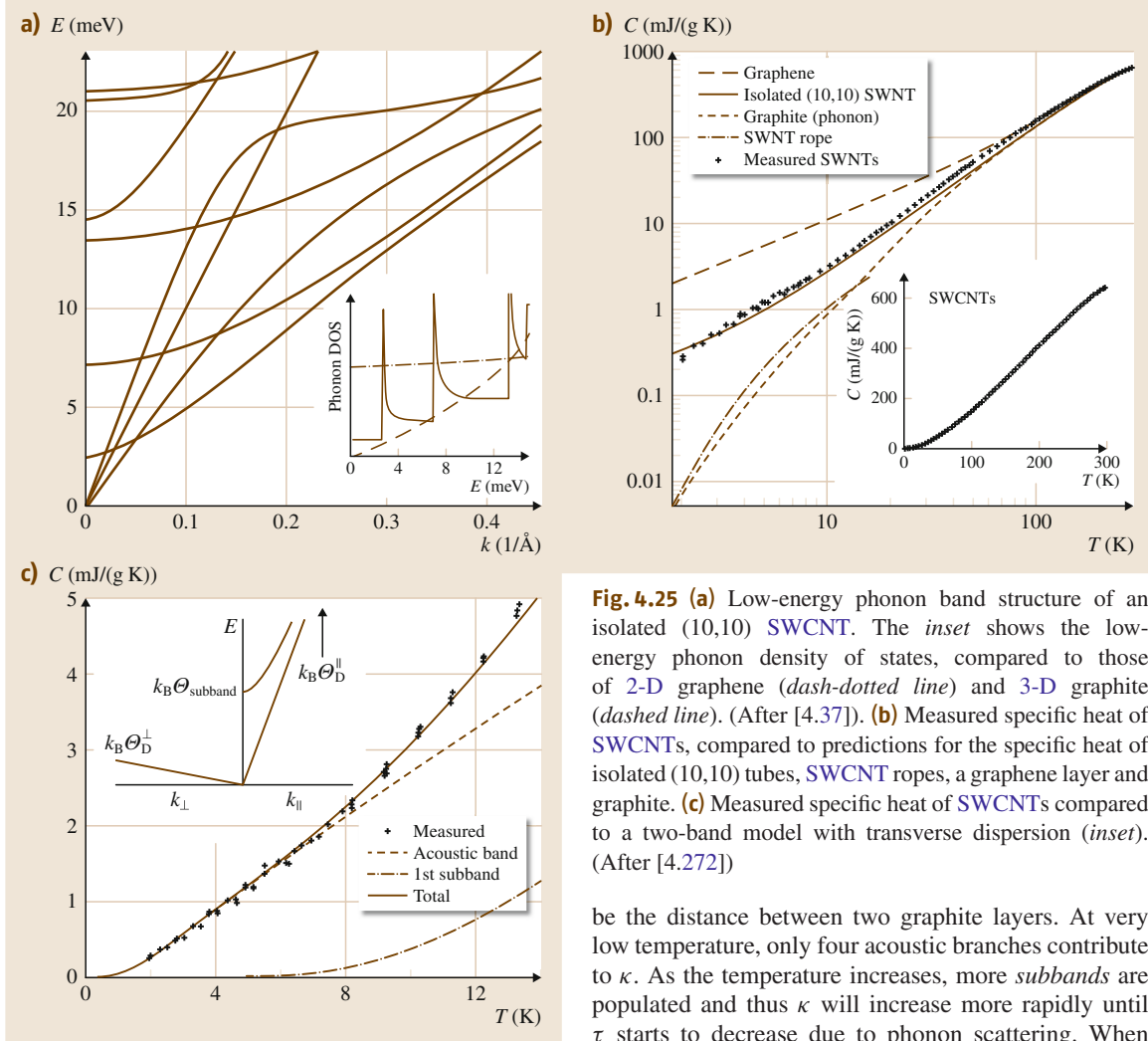


Fig. 4.25 (a) Low-energy phonon band structure of an isolated (10,10) SWCNT. The *inset* shows the low-energy phonon density of states, compared to those of 2-D graphene (dash-dotted line) and 3-D graphite (dashed line). (After [4.37]). (b) Measured specific heat of SWCNTs, compared to predictions for the specific heat of isolated (10,10) tubes, SWCNT ropes, a graphene layer and graphite. (c) Measured specific heat of SWCNTs compared to a two-band model with transverse dispersion (*inset*). (After [4.272])

modes with higher ν_z and τ should contribute more. κ is bounded by the 1-D ballistic transport limit. For each phonon mode, the quantum of thermal conductance is [4.47]

$$G_{\text{th}} = \frac{\pi^2 k_B T}{3 h}, \quad (4.15)$$

and therefore the effective thermal conductivity is

$$\kappa_{\text{eff}} = G_{\text{th}} \frac{L}{\pi d_t \delta d}, \quad (4.16)$$

where L is the length of the carbon nanotube, d_t is its diameter, and δd is the effective thickness that the phonon propagates over, which is usually assumed to

be the distance between two graphite layers. At very low temperature, only four acoustic branches contribute to κ . As the temperature increases, more *subbands* are populated and thus κ will increase more rapidly until τ starts to decrease due to phonon scattering. When $T \gg \Theta_D$, Umklapp scattering between zone boundary phonons will significantly reduce τ and consequently reduce κ [4.273]. So there should be a turning point in $\kappa(T)$, where it reaches its maximum. Since CNTs have a very high Debye temperature and their 1-D structure reduces Umklapp scattering due to deficiency in conserving momentum and energy, the turning point should be at a fairly high temperature.

In metallic or doped SWCNTs, electron systems also contribute to the thermal conductivity. Principally, the electronic thermal conductivity κ_{el} can be determined from electronic conductivity by the Wiedemann-Franz law

$$\frac{\kappa_{\text{el}}}{\sigma} \approx L_0, \quad (4.17)$$

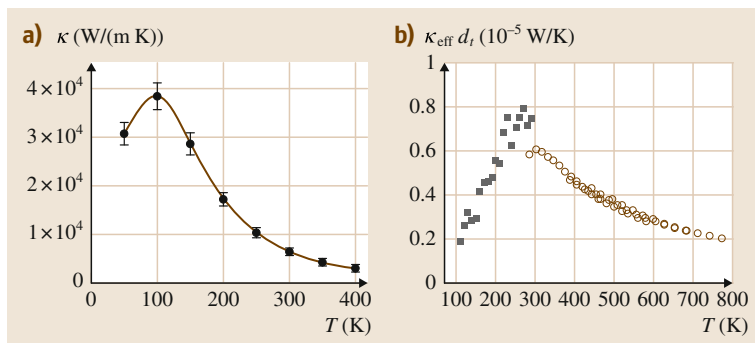


Fig. 4.26 (a) Calculated thermal conductivity of an isolated (10,10) SWCNT, as a function of temperature. (b) Measured diameter-adjusted thermal conductivity ($\kappa_{\text{eff}} d_t$, see (4.16)) of an isolated SWCNT, as a function of temperature. Since the diameters of the tubes range from 1 to 3 nm, the maximum value of kappa is several thousands W/(m K) (■: Yu et al. [4.273]; ○: this work). (After [4.274])

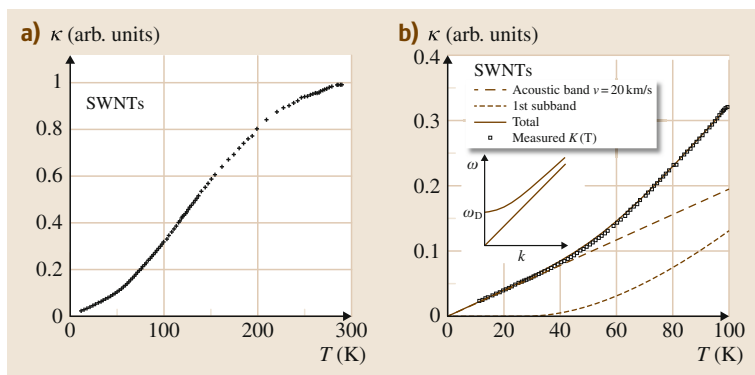


Fig. 4.27 (a) Thermal conductivity of a bulk sample of SWNTs below room temperature. (b) Highlight of the low temperature part fitted by two-band model. (After [4.275])

where the Lorenz number $L_0 = 2.45 \cdot 10^8 (\text{V/K})^2$ and σ is the electronic conductivity. The estimated κ_{el} is usually one or two orders of magnitude smaller than κ_{ph} and therefore can be ignored in most cases.

As shown in Fig. 4.26a the thermal conductivity of SWCNT has been predicted as high as 40 000 W/(m K) at its maximum and 3600 W/(m K) at room temperature [4.274]. On the other hand, the measured κ peaks around one order of magnitude lower a few thousandths of a watt per millikelvin W/(m K) as shown in Fig. 4.26b [4.276, 277], probably due to imperfections or short tube length [4.278]. When tubes are bundled or formed into a CNT network, κ will decrease strongly depending on the sample's morphology. The reduction may be attributed to a quench of phonon modes by intertube interactions, analogous to the effect on C_{ph} . This effect should be more significant for well-aligned CNT fibers or MWCNT devices [4.279]. Another reason is the weak transport at tube–tube junctions. It has been predicted that in a random network, κ would obey [4.280]

$$\kappa \sim \rho^2 L^2, \quad (4.18)$$

where ρ is the density of tubes in the network. This opens the possibility to tune the thermal conductivity of a SWCNT device from a good thermal conductor to a good thermal insulator [4.281].

Figure 4.27 shows a measured κ as function of temperature for a SWCNT network [4.275]. In this case, the effect of the intertube junction on κ is treated as a reduction of the phonon relaxation time τ . Consequently, the turning point of κ shifts to a higher temperature while its temperature dependency still reflects the 1-D nature of a CNT. The $\kappa(T)$ curve could be fit by considering the four acoustic phonon modes and the first subband mode (Fig. 4.27b). However, the fitting parameters are slightly different from those by fitting to heating capacity. The difference may be attributed to the weight factor $v^2 \tau$ in κ .

4.6.2 Mechanical Properties

SWCNTs lack the multiple cylindrical nesting of MWCNTs and are expected to be stiffer due to curvature effects [4.282]. Over the past couple of decades, SWCNTs have attracted a considerable amount of interest owing to their extraordinary mechanical properties,

such as their ability to sustain large deformations, their excellent stiffness, and high strength. Additionally, most conventional synthesis techniques result in **SWCNTs** arranged in ropes with a close-packed stacking, thus forming high performance self-assembled fibers on the nanoscale.

Elastic Properties

Overney et al. were the first to report on the structural rigidity of carbon nanotubes [4.284]. The authors used an empirical Keating Hamiltonian with parameters determined from first principles in order to model **SWCNTs** consisting of 100, 200, and 400 atoms. It was later pointed out by *Treacy* et al. that their results implied a Young's modulus in the range of 1.5–5.0 TPa [4.285]. *Lu* performed an extensive study of the elastic properties of **SWCNTs** (Table 4.1) and **SWCNT** ropes using an empirical force constant model [4.283]. The Young's modulus, E , for the materials was extracted from the second derivative of the ab initio strain energy with respect to the axial strain, $\partial^2 E / \partial \epsilon^2$. The tensile Young's modulus (≈ 1 TPa, a value which is in good agreement with the C_{11} elastic constant of graphite) and the torsion shear modulus of individual **SWCNTs** were found to be comparable to that of diamond and that of a graphitic sheet, while the bulk modulus was found to be smaller. Their elastic moduli were shown to be insensitive to structural details such as the chirality and radius. One must bear in mind that in order to deduce properties such as **SWCNT** Young's modulus, it is re-

quired to adopt a convention for the effective nanotube thickness. *Lu* chose the interlayer separation of graphite (0.34 nm, now a widely accepted convention) as the **SWCNT** wall thickness in his calculations. Assuming the extent of π orbitals (≈ 0.066 nm) to be the thickness, as *Yakobson* et al. had proposed earlier, can result in rather spectacular values of the **SWCNT** Young's modulus (≈ 5 TPa) [4.286]. *Lu's* study of **SWCNT** ropes, each assumed to be composed of 100–500 armchair **SWNTs** of uniform size arranged in hexagonal order, found them to be soft along the basal plane but very stiff along the axial direction. Their Young's moduli (average ≈ 0.6 TPa) were found to be about one-half that of diamond, values that decreased with nanotube radius. An alternate method that was based on the energy per-surface area rather than per-volume was used to deduce the **SWCNT** Young's modulus [4.287]. The authors used a nonorthogonal tight-binding scheme for their calculations and reported a surface Young's modulus of 0.42 TPa-nm (1.2 TPa) with only a slight dependence on diameter for **SWCNTs** with a diameter > 0.7 nm.

Interestingly, while **SWCNTs** can be highly rigid in the axial direction (as is evident from the high tensile Young's modulus values), they can experience considerable structural instability under compression, torsion, or bending in the radial direction [4.288]. *Yakobson* et al. modeled the buckling of **SWNTs** exposed to axial compression, with the atomic interaction modeled using the Tersoff–Brenner potential [4.289, 290]. They found

Table 4.1 Elastic coefficients and moduli of selective single-walled nanotubes. (n, m) are the chiral indices, R is the radius in nm, C_{11} and C_{33} are the elastic constants along the basal plane and the axial direction, respectively. B , Y , M are bulk, Young's, and shear moduli in units of TPa and ν is the Poisson ratio. Experimental values for the graphite and the diamond are listed for comparison. (After [4.283])

(n_1, n_2)	R (nm)	C_{11}	C_{33}	B (TPa)	Y (TPa)	M (TPa)	ν
(5,5)	0.34	0.397	1.054	0.191	0.971	0.436	0.280
(6,4)	0.34	0.397	1.054	0.191	0.972	0.437	0.280
(7,3)	0.35	0.397	1.055	0.190	0.973	0.454	0.280
(8,2)	0.36	0.397	1.057	0.190	0.974	0.452	0.280
(9,1)	0.37	0.396	1.058	0.191	0.974	0.465	0.280
(10,0)	0.39	0.396	1.058	0.190	0.975	0.451	0.280
(10,10)	0.68	0.398	1.054	0.191	0.972	0.457	0.278
(50,50)	3.39	0.399	1.054	0.192	0.972	0.458	0.278
(100,100)	6.78	0.399	1.054	0.192	0.972	0.462	0.277
(200,200)	13.5	0.399	1.054	0.192	0.972	0.478	0.277
Graphite along the basal plane		1.6	–	0.0083	1.02	0.44	0.16
Graphite along the C axis		–	0.036	0.0083	0.0365	0.004	0.012
Diamond along the cube axis		1.07	1.07	0.442	1.063	0.5758	0.1041

that nanotubes subject to large deformations reversibly switched into four different morphological patterns with each one corresponding to an abrupt release of energy and a singularity in the strain energy versus strain curve (Fig. 4.26). The authors' simulations of bending and torsion resulted in **SWCNT** cross-section collapses and similar observations of changes in energy with the increase in bending angle and azimuthal angle, between the tube ends, respectively. Cross-section collapses and flattening can also occur in **SWCNT** ropes owing to van der Waal's attractive forces between the tubes. Tersoff and Ruoff studied the deformation pattern of **SWCNTs** in ropes and concluded that rigid tubes with diameters < 1 nm deform insignificantly while those with diameters > 2.5 nm flatten against each other thus forming a honeycomb-like structure [4.291].

Strength and Plasticity

Quantum mechanical calculations predict that defect-free single-walled carbon nanotubes possess tensile strengths greater than 100 GPa (i.e., close to the theoretical strength viz. $E/10$ GPa) and failure strains as high as 15–30% depending upon chirality [4.293, 294]. Yakobson et al., used molecular dynamics (MD) simulations to perform high-strain-rate tensile tests (in the range of 100 MHz) on **SWCNTs** and found that stretching simply elongated the hexagons in the tube walls, until at the critical point an atomic disorder suddenly nucleated: one or a few C–C bonds broke almost simultaneously, and the resulting *holes* in the tube walls became crack precursors. While the fractures propagated very quickly along the circumference of the tubes, the nanotubes themselves did not break completely in half but were separated into two parts connected by a monoatomic carbon chain [4.288]. Under compression, classical MD simulations have shown a **SWCNT** to also be remarkably resilient, sustaining strains as high as 15% with no signs of brittleness, plasticity, or atomic rearrangements [4.295].

Theoretical predictions, however, have constantly emphasized the important role played by defects, the loading rate, and temperature on the strength of a **SWCNT** [4.296]. Defects often become incorporated into the **SWCNT** structure during purification or dispersion. Also, the mode of **CNT** synthesis plays an important role in determining the nature and distribution of defects, with low temperature catalytic chemical vapor deposition (CVD) grown nanotubes typically having a more defect laden structure when compared to nanotubes grown via other techniques such as laser vaporization and arc discharge (AD). The presence of

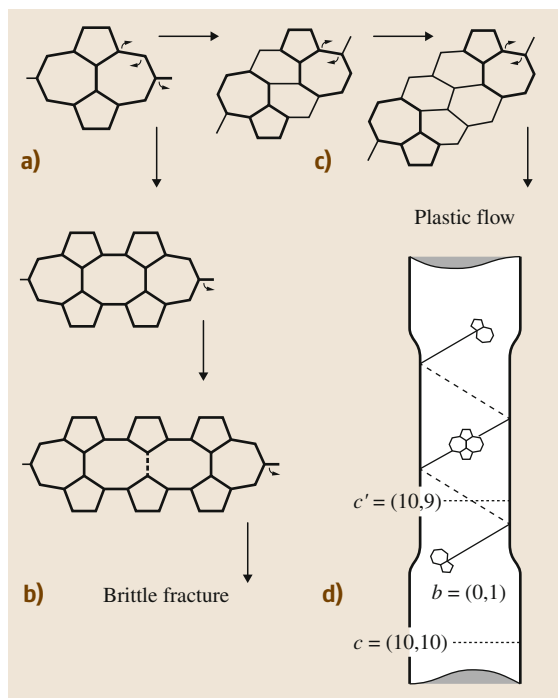


Fig. 4.28 Stone–Wales (S–W) transformations of an equatorially oriented bond into a vertical position creates a nucleus of relaxation (*top left corner*). It evolves further as either a crack (*brittle fracture route, left column*) or as a couple of dislocations gliding away along the spiral slip plane (*plastic yield, top row*). In both cases only S–W rotations are required as elementary steps. The stepwise change of the nanotube diameter reflects the change of chirality (*bottom right image*). (After [4.292])

defects on the nanotube wall can considerably degrade the strength of a **SWCNT**. Belytschko et al. observed a drop in the failure stress from 93 GPa to 74 GPa upon the incorporation of a single atom defect on a zigzag **SWCNT** wall. The failure strains were also found to drop from 15.5% to 10% [4.293]. Sammalkorpi et al. used MD simulations to study how vacancies affect the Young's modulus and tensile strength of **SWCNTs** [4.297]. They found that while the Young's modulus depended weakly on the vacancy concentration (a relatively high defect density of one vacancy per 50 Å resulted in about a 3% decrease in the Young's modulus), the **SWCNT** tensile strength could degrade by $\approx 40\%$ (actual value chirality dependent) if vacancies were present on their walls.

With regard to the deformation of **SWCNTs** in static or slow tension conditions, an interesting phenomenon

was uncovered by quantum molecular dynamics simulations and dislocation theory: a mechanical relaxation step that occurs via a bond rotation known as a Stone–Wales (S–W) transformation (Fig. 4.28) [4.298]. It leads to the formation of the lowest energy defect, a cluster of two pentagons and heptagons 5/7/7/5 on the SWCNT wall. In a lattice of hexagons this represents a dislocation dipole, which explains its formation under high tension. At high temperatures, 5/7/7/5 defects in SWNTs of a certain chirality, can separate into two 5,7 pairs that glide away from each other in a spiral path, leaving in their wake a plastically deformed nanotube with an altered chirality. In contrast, a competing mechanism of evolution, which does not require thermal activation, occurs at a high strain level as a sequence of direct brittle bond-breaking steps leading to formation of disordered cracks and large open rings, which results in the brittle failure of a SWCNT (Fig. 4.28) [4.292, 299]. Thus, while all SWCNTs behave in a brittle fashion at high strains and low temperatures, at high temperatures and low strains, SWCNTs of a certain chirality can be completely or partially ductile. This has been observed in a (10,10) armchair nanotube with a 5/7/7/5 defect under axial tension. At a strain value close to 15% and temperature of about 1300 K, nucleation of large open rings occurred (brittle relaxation), while at a strain value $\approx 3\%$ and at a temperature of about 3000 K, 5/7 defect motion resulted in plastic flow [4.300]. It has been suggested that an axially compressed SWCNT would also deform plastically via S–W defect based mechanism [4.292]. Interestingly, Srivastava et al., who employed a quantum generalized tight binding molecular dynamics (GTBMD) scheme to study SWNTs under compression, observed an alternate mechanism of plastic deformation in which SWCNT bonding geometry collapsed from a graphitic sp^2 to a localized diamond-like sp^3 reconstruction [4.301, 302]. The computed critical strain for such a collapse for a (8,0) zigzag SWNT was $\approx 12\%$, a value considerably lower than the elastic limit computed using classical MD simulations (Fig. 4.29).

Mechanical Characterization

Owing to their small size and the magnitude of the forces involved, the mechanical characterization of individual SWCNTs is extremely challenging. There are thus only a handful of reports that deal with characterization of individual SWCNTs, with many of them relying on the electrical breakdown of MWCNTs for SWCNT generation. However, numerous studies fo-

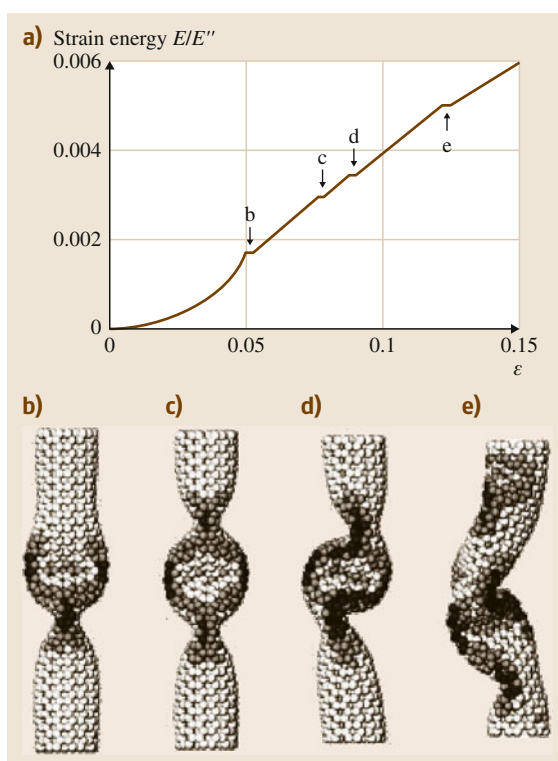


Fig. 4.29a–e MD-simulated nanotube of length 6 nm, diameter 1 nm, and armchair helicity (7,7) under axial compression. The strain energy displays four singularities **b, c, d, e** as shown in strain energy (normalized to its second derivative) versus strain (ϵ) curve corresponding to shape changes (**a**); at $\epsilon = 0.05$ the cylinder buckles into the pattern (**b**), displaying two identical flattenings, *fins*, perpendicular to each other. Further increasing strain enhances this pattern gradually until at $\epsilon = 0.076$ the tube switches to a three-fin pattern (**c**), which still possesses a straight axis. On buckling sideways at $\epsilon = 0.09$ the flattenings serve as hinges, and only a plane of symmetry is preserved (**d**). At $\epsilon = 0.13$ (**e**) an entirely squashed asymmetric nanotube. (After [4.286])

cus on the properties of SWCNT ropes. Using an atomic force microscope (AFM) based deflection technique, Salvétat et al. measured the vertical deflection of SWCNT ropes bridging holes on a porous alumina membrane (Fig. 4.30) [4.303]. The ropes were modeled as beams, with a term describing sliding between tubes (shear) comprising the ropes being included in the expression for mechanical deformation

$$\delta = \delta_B + \delta_S = FL^3/192EI + f_s FL/4GA,$$

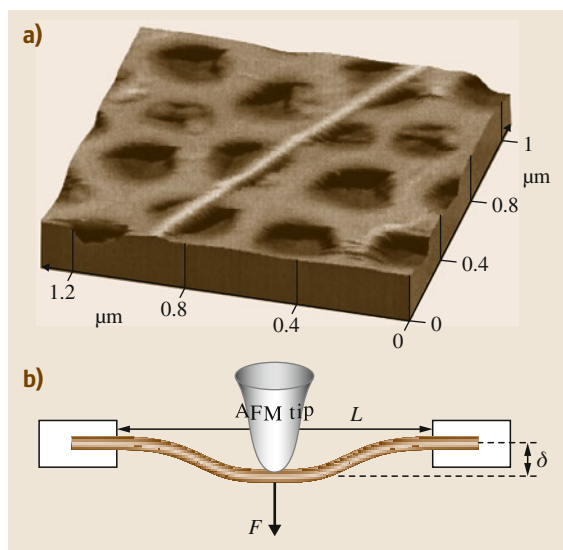


Fig. 4.30 (a) AFM image of a SWCNT rope adhered to the polished alumina ultrafiltration membrane, with a portion bridging a pore. (b) The AFM is used to apply a load to the nanobeam and to determine directly the resulting deflection. (After [4.303])

where F is the concentrated load, δ_B and δ_S are the deflections due to bending and shear deformation respectively, L is the suspended length, E is the elastic modulus, f_s is the shape factor (equal to 10/9 for a cylindrical beam), G is the shear modulus, I is the second moment of area of the beam and A is the cross-sectional area. Deflections of small diameter long ropes, for which shearing was assumed to be negligible, were used to compute Young's modulus (measured to be about 1 TPa), while the deflection of thick ropes was used to compute the intertube shear modulus G measured as ≈ 1 GPa. Walters et al. also studied the elastic properties of freely suspended SWCNT ropes by inducing large elastic strains using an AFM tip operating in the lateral force mode [4.304]. By modeling the stretched ropes as elastic strings (instead of beams), the authors were able to derive an expression for the force F exerted on the tube by the AFM tip

$$F = 2T \sin(\theta) = 2T \frac{2x}{L} \approx \frac{8kx^3}{L_0},$$

where T is the tension in the string, L_0 its equilibrium length, k the spring constant, and x the lateral deflection in the middle. Assuming a Young's modulus of 1.25 TPa for SWCNTs, they deduced that close-packed

nanotube ropes would have a yield strength exceeding 45.67 GPa (corresponding to a 5.8% strain). Yu et al. subjected 15 SWCNT ropes to tensile loading using a nanostressing stage (two opposing AFM tips) operated inside an SEM chamber [4.305]. Force versus strain data were obtained for 8 ropes, with the highest strain value observed being 5.3%. By examining the fragments left on the AFM tips post failure, the authors deduced that only the SWCNTs along the periphery of the ropes were load bearing. They were thus able to ascertain the average breaking strength of SWNTs along the perimeter of each rope, viz. 13 to 52 GPa. The corresponding Young's moduli were determined to be in the range of 320 to 1470 GPa. The mechanical properties of SWCNT bundles in compression were studied by Chesnokov et al., who subjected them to quasi-hydrostatic pressure using a piston-cylinder setup. The bundles were found to undergo a reversible deformation up to a pressure of 3 GPa [4.306]. Tang et al. used a diamond anvil cell to subject SWCNT bundles to hydrostatic pressure and observed that the SWCNTs were linearly elastic up to 1.5 GPa at room temperature. The volume compressibility, measured via in situ synchrotron x-ray diffraction, was determined to be 0.024 GPa^{-1} [4.307].

Krishnan et al. estimated the stiffness of individual SWCNTs by observing their freestanding room temperature vibrations in a TEM [4.308]. The nanotube lengths and tip vibration amplitudes were estimated directly from the digital micrographs. The nanotubes were modeled as stochastically driven resonators (i.e., they were assumed to be vibrating beams) and their Young's moduli estimated from their Gaussian vibrational profile whose standard deviation is given by

$$\sigma^2 = 0.8486 \frac{L^3 k_B T}{YWG(W^2 + G^2)},$$

where L is the cantilevered beam's length (SWNT length), G is the graphite interlayer spacing, W is the SWCNT diameter, T the temperature and Y the Young's modulus. Micrographs of 27 nanotubes in the diameter range 1.0–1.5 nm were measured to yield an average Young's modulus of $1.3 + 0.4 / - 0.6$ TPa. Wang et al. directly tested the mechanical response of SWCNTs by subjecting them to tensile loads using an AFM within a TEM setup [4.309]. The SWCNTs for the experiments were formed in situ by subjecting MWNTs to large voltage biases. The tubes were found to exhibit fracture strengths ranging from 25 to 100 GPa. SWCNTs with relatively higher strength possessed visibly perfect

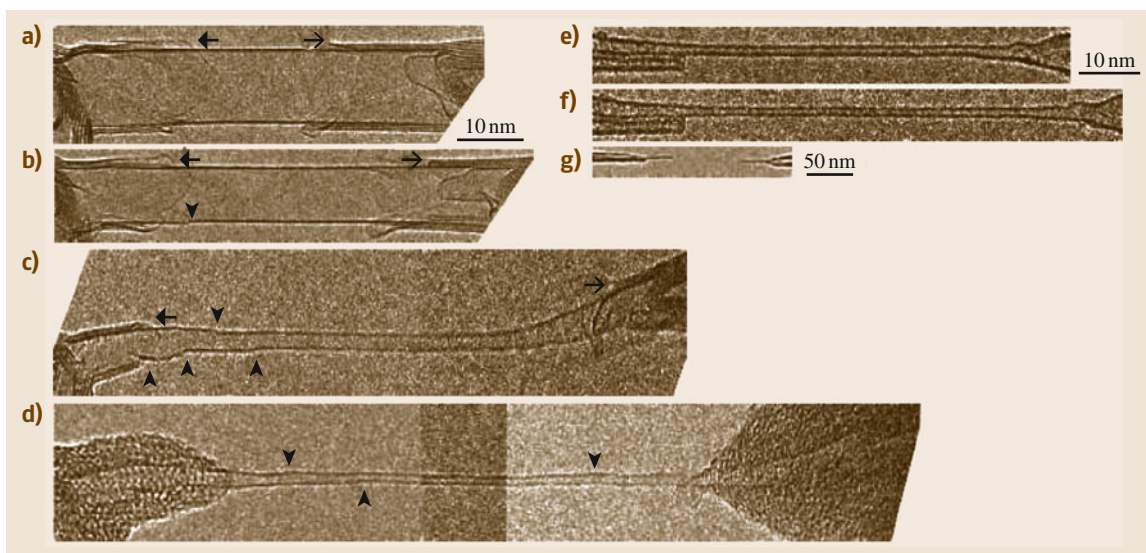


Fig. 4.31 In situ tensile elongation of individual SWNTs viewed in a HRTEM. (a–d) Tensile elongation of a SWNT under a constant bias of 2.3 V (images are all scaled to the same magnification). Arrowheads mark kinks, arrows indicate features at the ends of the nanotube that are almost unchanged during elongation; e.g., tensile elongation of a SWCNT at room temperature without bias ((e–g) are scaled to the same magnification). (After [4.310])

shell structures while the significant strength reduction in low-strength samples was attributed to clearly identifiable shell structural defects. Huang et al. observed *superplasticity* in a SWCNT (Fig. 4.31) [4.310]. The nanotube was subjected to a tensile load and at failure, found to be 91 nm long, showing an elongation of 280% with its diameter reduced 15-fold, from 12 to 0.8 nm. Since the deformation occurred at a bias of about 2.3 V,

the temperature in the middle of the SWCNT was estimated to be more than 2000 °C. This superplastic deformation was assumed to be the result of the nucleation and motion of kinks (possibly 5/7 pairs) as well as atom diffusion. In contrast, tensile-pulling experiments conducted at room temperature with no bias showed in SWCNTs failing at a tensile strain of less than 15%.

4.7 Concluding Remarks

Single-walled carbon nanotubes have been extensively studied and immense progress has been made in their basic understanding, demonstrating the potential of nanoscience in general. A good understanding of their basic properties has been reached, but direct evidences of some fundamental processes are still lacking; for example, spin-charge separation expected in Luttinger liquids.

The feasibility of nanotube applications lies directly between basic and technical questions. For example, nanotube photodetectors and emitters (or even lasers) would be of great tunability and could potentially cover large wavelength ranges. Efforts are being made to obtain purer, single chirality semiconductors material in large quantities, and to understand the mechanisms limiting their light emission.

References

- 4.1 S. Iijima: Helical microtubules of graphitic carbon, *Nature* **354**(6348), 56–58 (1991)
- 4.2 M.S. Dresselhaus, G. Dresselhaus, P. Avouris (eds.): *Carbon Nanotubes: Synthesis, Structure, Properties,*

- and Applications, Topics in Applied Physics, Vol. 80 (Springer, Berlin, Heidelberg 2001)
- 4.3 S. Reich, C. Thomsen, J. Maultzsch: *Carbon Nanotubes: Basic Concepts and Physical Properties* (Wiley-VCH, Weinheim 2004)
 - 4.4 M.J. O'Connell (Ed.): *Carbon Nanotubes: Properties and Applications* (CRC, Boca Raton 2006)
 - 4.5 A. Jorio, G. Dresselhaus, M.S. Dresselhaus (Eds.): *Carbon Nanotubes: Advanced Topics in the Synthesis, Structure, Properties and Applications*, Topics in Applied Physics, Vol. 111 (Springer, Berlin, Heidelberg 2008)
 - 4.6 T. Giamarchi: *Quantum Physics in One Dimension* (Oxford Univ. Press, Oxford 2004)
 - 4.7 P. Avouris, M. Freitag, V. Perebeinos: Carbon-nanotube photonics and optoelectronics, *Nat. Photonics* **2**, 341–350 (2008)
 - 4.8 S. Nanot, E.H. Hároz, J.-H. Kim, R.H. Hauge, J. Kono: Optoelectronic properties of single-wall carbon nanotubes, *Adv. Mater.* **24**, 4977–4994 (2012)
 - 4.9 M.S. Dresselhaus, A. Jorio, M. Hofmann, G. Dresselhaus, R. Saito: Perspectives on carbon nanotubes and graphene Raman spectroscopy, *Nano Lett.* **10**, 751–758 (2010)
 - 4.10 H. Ajiki, T. Ando: Aharonov–Bohm effect in carbon nanotubes, *Physica B* **201**, 349–352 (1994)
 - 4.11 M.F. Islam, D.E. Milkie, C.L. Kane, A.G. Yodh, J.M. Kikkawa: Direct measurement of the polarized optical absorption cross section of single-wall carbon nanotubes, *Phys. Rev. Lett.* **93**, 037404 (2004)
 - 4.12 Y. Murakami, E. Einarsson, T. Edamura, S. Maruyama: Polarization dependence of the optical absorption of single-walled carbon nanotubes, *Phys. Rev. Lett.* **94**, 087402 (2005)
 - 4.13 H. Ajiki, T. Ando: Magnetic properties of carbon nanotubes, *J. Phys. Soc. Jpn.* **62**, 2470–2480 (1993)
 - 4.14 J.P. Lu: Novel magnetic properties of carbon nanotubes, *Phys. Rev. Lett.* **74**, 1123–1126 (1995)
 - 4.15 S. Zaric, G.N. Ostojic, J. Kono, J. Shaver, V.C. Moore, R.H. Hauge, R.E. Smalley, X. Wei: Estimation of magnetic susceptibility anisotropy of carbon nanotubes using magneto-photoluminescence, *Nano Lett.* **4**, 2219–2221 (2004)
 - 4.16 M.F. Islam, D.E. Milkie, O.N. Torrens, A.G. Yodh, J.M. Kikkawa: Magnetic heterogeneity and alignment of single wall carbon nanotubes, *Phys. Rev. B* **71**, 201401 (2005)
 - 4.17 T.A. Searles, Y. Imanaka, T. Takamasu, H. Ajiki, J.A. Fagan, E.K. Hobbie, J. Kono: Large anisotropy in the magnetic susceptibility of metallic carbon nanotubes, *Phys. Rev. Lett.* **105**, 017403 (2010)
 - 4.18 T.-I. Jeon, K.-J. Kim, C. Kang, S.-J. Oh, J.-H. Son, K.H. An, D.J. Bae, Y.H. Lee: Terahertz conductivity of anisotropic single walled carbon nanotube films, *Appl. Phys. Lett.* **80**, 3403–3405 (2002)
 - 4.19 L. Ren, C.L. Pint, L.G. Booshehri, W.D. Rice, X. Wang, D.J. Hilton, K. Takeya, I. Kawayama, M. Tonouchi, R.H. Hauge, J. Kono: Carbon nanotube terahertz polarizer, *Nano Lett.* **9**, 2610–2613 (2009)
 - 4.20 J. Kyoung, E.-Y. Jang, M.D. Lima, H.-R. Park, R.-O. Robls, X. Lepro, Y.-H. Kim, R.H. Baughman, D.-S. Kim: A reel-wound carbon nanotube polarizer for terahertz frequencies, *Nano Lett.* **11**, 4227–4231 (2011)
 - 4.21 L. Ren, C.L. Pint, T. Arikawa, K. Takeya, I. Kawayama, M. Tonouchi, R.H. Hauge, J. Kono: Broadband terahertz polarizers with ideal performance based on aligned carbon nanotube stacks, *Nano Lett.* **12**, 787–790 (2012)
 - 4.22 H. Ajiki, T. Ando: Electronic states of carbon nanotubes, *J. Phys. Soc. Jpn.* **62**, 1255–1266 (1993)
 - 4.23 T. Ando: Theory of electronic states and transport in carbon nanotubes, *J. Phys. Soc. Jpn.* **74**, 777–817 (2005)
 - 4.24 J. Kono, S. Roche: Magnetic properties. In: *Carbon Nanotubes: Properties and Applications*, ed. by M.J. O'Connell (CRC, Boca Raton 2006), 119–151
 - 4.25 J. Kono, R.J. Nicholas, S. Roche: High magnetic field phenomena in carbon nanotubes. In: *Carbon Nanotubes: Advanced Topics in the Synthesis, Structure, Properties and Applications*, ed. by A. Jorio, G. Dresselhaus, M.S. Dresselhaus (Springer, Berlin, Heidelberg 2008), 393–421
 - 4.26 R. Saito, G. Dresselhaus, M.S. Dresselhaus: *Physical Properties of Carbon Nanotubes* (Imperial College Press, London 1998)
 - 4.27 A. Loiseau, P. Launois, P. Petit, S. Roche, J.-P. Salvetat (eds.): *Understanding Carbon Nanotubes: From Basics to Application*, Lecture Notes in Physics, Vol. 677 (Springer, Berlin, Heidelberg 2006)
 - 4.28 F. Léonard: *The Physics of Carbon Nanotube Devices* (William Andrew, Norwich 2009)
 - 4.29 A.H. Castro Neto, F. Guinea, N.M.R. Peres, K.S. Novoselov, A.K. Geim: The electronic properties of graphene, *Rev. Mod. Phys.* **81**(1), 109 (2009)
 - 4.30 R. Saito, M. Fujita, G. Dresselhaus, M.S. Dresselhaus: Electronic structure of chiral graphene tubules, *Appl. Phys. Lett.* **60**, 2204–2206 (1992)
 - 4.31 N. Hamada, S. Sawada, A. Oshiyama: New one-dimensional conductors: Graphitic microtubules, *Phys. Rev. Lett.* **68**, 1579–1581 (1992)
 - 4.32 H. Ajiki, T. Ando: Electronic states of carbon nanotubes, *J. Phys. Soc. Jpn.* **62**, 1255–1266 (1993)
 - 4.33 J.W. Mintmire, B.I. Dunlap, C.T. White: Are fullerene tubules metallic?, *Phys. Rev. Lett.* **68**, 631–634 (1992)
 - 4.34 P.R. Wallace: The band theory of graphite, *Phys. Rev.* **71**(9), 622–634 (1947)
 - 4.35 B. Bourlon: *Physique Interfeuillet Dans Les Nanotubes de Carbone Multifeuillet*. Ph.D. Thesis (Université Paris VI, Paris 2005)
 - 4.36 C. Kane, L. Balents, M.P.A. Fisher: Coulomb interactions and mesoscopic effects in carbon nanotubes, *Phys. Rev. Lett.* **79**, 5086–5089 (1997)
 - 4.37 M.S. Dresselhaus, P.C. Eklund: Phonons in carbon nanotubes, *Adv. Phys.* **49**(6), 705–814 (2000)

- 4.38 R.A. Jishi, L. Venkataraman, M.S. Dresselhaus, G. Dresselhaus: Phonon modes in carbon nanotubes, *Chem. Phys. Lett.* **209**(1/2), 77–82 (1993)
- 4.39 P.C. Eklund, J.M. Holden, R.A. Jishi: Phonon modes in carbon nanotubes, *Carbon* **33**(7), 959–972 (1995)
- 4.40 R. Saito, T. Takeya, T. Kimura, G. Dresselhaus, M.S. Dresselhaus: Raman intensity of single-wall carbon nanotubes, *Phys. Rev. B* **57**, 4145–4153 (1998)
- 4.41 O. Dubay, G. Kresse: Accurate density functional calculations for the phonon dispersion relations of graphite layer and carbon nanotubes, *Phys. Rev. B* **67**, 035401 (2003)
- 4.42 J. Yu, R.K. Kalia, P. Vashishta: Phonons in graphitic tubules: A tight-binding molecular dynamics study, *J. Chem. Phys.* **103**, 6697 (1995)
- 4.43 M. Menon, E. Richter, K.R. Subbaswamy: Structural and vibrational properties of fullerenes and nanotubes in a nonorthogonal tight-binding scheme, *J. Chem. Phys.* **104**(15), 5875–5882 (1996)
- 4.44 J. Kürti, G. Kresse, H. Kuzmany: First-principles calculations of the radial breathing mode of single-wall carbon nanotubes, *Phys. Rev. B* **58**, R8869–R8872 (1998)
- 4.45 D. Sánchez-Portal, E. Artacho, J.M. Soler, A. Rubio, P. Ordejón: *Ab initio* structural, elastic, and vibrational properties of carbon nanotubes, *Phys. Rev. B* **59**, 12678–12688 (1999)
- 4.46 L.-H. Ye, B.-G. Liu, D.-S. Wang, R. Han: *Ab initio* phonon dispersions of single-wall carbon nanotubes, *Phys. Rev. B* **69**, 235409 (2004)
- 4.47 J. Hone: Phonons and thermal properties of carbon nanotubes. In: *Carbon Nanotubes*, Topics in Applied Physics, Vol. 80, ed. by M. Dresselhaus, G. Dresselhaus, P. Avouris (Springer, Berlin, Heidelberg 2001) pp. 273–286
- 4.48 S. Rols, Z. Benes, E. Anglaret, J.L. Sauvajol, P. Papanek, J.E. Fischer, G. Coddens, H. Schober, A.J. Dianoux: Phonon density of states of single-wall carbon nanotubes, *Phys. Rev. Lett.* **85**, 5222–5225 (2000)
- 4.49 J. Hone: Carbon nanotubes: Thermal properties. In: *Dekker Encyclopedia of Nanoscience and Nanotechnology*, ed. by J.A. Schwarz, C.I. Contescu, K. Putyera (Marcel Dekker, New York 2004) pp. 603–610
- 4.50 A. Mizel, L.X. Benedict, M.L. Cohen, S.G. Louie, A. Zettl, N.K. Budraa, W.P. Beyermann: Analysis of the low-temperature specific heat of multiwalled carbon nanotubes and carbon nanotube ropes, *Phys. Rev. B* **60**, 3264–3270 (1999)
- 4.51 D. Kahn, J.P. Lu: Vibrational modes of carbon nanotubes and nanoropes, *Phys. Rev. B* **60**, 6535–6540 (1999)
- 4.52 P. Eklund, P.A.R. Blackmon, A.J. Hart, J. Kong, P. Bhabendra, A. Rao, A. Rinzier: *International Assessment of Research and Development on Carbon Nanotubes: Manufacturing and Applications* (World Technology Evaluation Center, Arlington 2007), available online at <http://www.wtec.org/cnm/>
- 4.53 M. Kundrapu, J. Li, A. Shashurin, M. Keidar: A model of carbon nanotube synthesis in arc discharge plasmas, *J. Phys. D* **45**, 315305 (2012)
- 4.54 T. Guo, P. Nikolaev, A. Thess, D.T. Colbert, R.E. Smalley: Catalytic growth of single-walled nanotubes by laser vaporization, *Chem. Phys. Lett.* **243**, 49–54 (1995)
- 4.55 T.W. Ebbesen, P.M. Ajayan: Large-scale synthesis of carbon nanotubes, *Nature* **358**(6383), 220–222 (1992)
- 4.56 D.S. Bethune, C.H. Kiang, M.S. Devries, G. Gorman, R. Savoy, J. Vazquez, R. Beyers: Cobalt-catalysed growth of carbon nanotubes with single-atomic-layer walls, *Nature* **363**(6430), 605–607 (1993)
- 4.57 T. Guo, P. Nikolaev, A. Thess, D.T. Colbert, R.E. Smalley: Catalytic growth of single-walled nanotubes by laser vaporization, *Chem. Phys. Lett.* **243**(1/2), 49–54 (1995)
- 4.58 B.I. Yakobson, R.E. Smalley: Fullerene nanotubes: $C_{1000000}$ and beyond, *Am. Sci.* **85**(4), 324–337 (1997)
- 4.59 M.J. Bronikowski, P.A. Willis, D.T. Colbert, K.A. Smith, R.E. Smalley: Gas-phase production of carbon single-walled nanotubes from carbon monoxide via the HiPco process: A parametric study, *J. Vac. Sci. Technol. A* **19**(4), 1800–1805 (2001)
- 4.60 Y. Liu, W.Z. Qian, Q. Zhang, G.Q. Ning, G.H. Luo, Y. Wang, D.Z. Wang, F. Wei: Synthesis of high-quality, double-walled carbon nanotubes in a fluidized bed reactor, *Chem. Eng. Technol.* **32**(1), 73–79 (2009)
- 4.61 Y. Wang, B. Li, P.S. Ho, Z. Yao, L. Shi: Effect of supporting layer on growth of carbon nanotubes by thermal chemical vapor deposition, *Appl. Phys. Lett.* **89**, 183113 (2006)
- 4.62 R. Philippe, A. Morand, M. Corrias, B. Caussat, Y. Kihn, P. Kalck, D. Plee, P. Gaillard, D. Bernard, P. Serp: Catalytic production of carbon nanotubes by fluidized-bed CVD, *Chem. Vap. Depos.* **13**(9), 447–457 (2007)
- 4.63 M. Meyyappan: A review of plasma enhanced chemical vapour deposition of carbon nanotubes, *J. Phys. D* **42**(21), 15 (2009)
- 4.64 Y.Q. Xu, E. Flor, H. Schmidt, R.E. Smalley, R.H. Hauge: Effects of atomic hydrogen and active carbon species in 1 mm vertically aligned single-walled carbon nanotube growth, *Appl. Phys. Lett.* **89**(12), 3 (2006)
- 4.65 C.L. Pint, G.B. Bozzolo, R. Hauge: Catalyst design for carbon nanotube growth using atomistic modeling, *Nanotechnology* **19**, 405704 (2008)
- 4.66 S.S. Fan, M.G. Chapline, N.R. Franklin, T.W. Tombler, A.M. Cassell, H.J. Dai: Self-oriented regular arrays of carbon nanotubes and their field emission properties, *Science* **283**(5401), 512–514 (1999)
- 4.67 K. Hata, D.N. Futaba, K. Mizuno, T. Namai, M. Yumura, S. Iijima: Water-assisted highly efficient synthesis of impurity-free single-walled carbon nanotubes, *Science* **306**(5700), 1362–1364 (2004)
- 4.68 Y. Murakami, S. Chiashi, Y. Miyauchi, M.H. Hu, M. Ogura, T. Okubo, S. Maruyama: Growth of ver-

- tically aligned single-walled carbon nanotube films on quartz substrates and their optical anisotropy, *Chem. Phys. Lett.* **385**(3/4), 298–303 (2004)
- 4.69 S. Yasuda, D.N. Futaba, T. Yamada, J. Satou, A. Shibuya, H. Takai, K. Arakawa, M. Yumura, K. Hata: Improved and large area single-walled carbon nanotube forest growth by controlling the gas flow direction, *ACS Nano* **3**(12), 4164–4170 (2009)
- 4.70 G.D. Nessim, M. Seita, K.P. O'Brien, A.J. Hart, R.K. Bonaparte, R.R. Mitchell, C.V. Thompson: Low temperature synthesis of vertically aligned carbon nanotubes with electrical contact to metallic substrates enabled by thermal decomposition of the carbon feedstock, *Nano Lett.* **9**(10), 3398–3405 (2009)
- 4.71 R.F. Wood, S. Pannala, J.C. Wells, A.A. Puzetzy, D.B. Geohegan: Simple model of the interrelation between single- and multiwall carbon nanotube growth rates for the CVD process, *Phys. Rev. B* **75**(23), 8 (2007)
- 4.72 S.M. Kim, C.L. Pint, P.B. Amama, D.N. Zakharov, R.H. Hauge, B. Maruyama, E.A. Stach: Evolution in catalyst morphology leads to carbon nanotube growth termination, *J. Phys. Chem. Lett.* **1**(6), 918–922 (2010)
- 4.73 A.A. Puzetzy, D.B. Geohegan, S. Jesse, I.N. Ivanov, G. Eres: In situ measurements and modeling of carbon nanotube array growth kinetics during chemical vapor deposition, *Appl. Phys. A* **81**, 223–240 (2005)
- 4.74 T. Ogawa, T. Takagahara: Interband absorption spectra and Sommerfeld factors of a one-dimensional electron-hole system, *Phys. Rev. B* **43**, 14325–14328 (1991)
- 4.75 T. Ogawa, T. Takagahara: Optical absorption and Sommerfeld factors of one-dimensional semiconductors: An exact treatment of excitonic effects, *Phys. Rev. B* **44**, 8138–8156 (1991)
- 4.76 M.J. O'Connell, S.M. Bachilo, C.B. Huffman, V.C. Moore, M.S. Strano, E.H. Háróz, K.L. Rialon, P.J. Boul, W.H. Noon, C. Kittrell, J. Ma, R.H. Hauge, R.B. Weisman, R.E. Smalley: Band gap fluorescence from individual single-walled carbon nanotubes, *Science* **297**, 593–596 (2002)
- 4.77 S.M. Bachilo, M.S. Strano, C. Kittrell, R.H. Hauge, R.E. Smalley, R.B. Weisman: Structure-assigned optical spectra of single-walled carbon nanotubes, *Science* **298**, 2361–2366 (2002)
- 4.78 S. Lebedkin, F. Hennrich, T. Skipa, M.M. Kappes: Near-infrared photoluminescence of single-walled carbon nanotubes prepared by the laser vaporization method, *J. Phys. Chem. B* **107**, 1949–1956 (2003)
- 4.79 J. Lefebvre, Y. Homma, P. Finnie: Bright band gap photoluminescence from unprocessed single-walled carbon nanotubes, *Phys. Rev. Lett.* **90**, 217401 (2003)
- 4.80 R.B. Weisman, S.M. Bachilo: Dependence of optical transition energies on structure for single-walled carbon nanotubes in aqueous suspension: An empirical Kataura plot, *Nano Lett.* **3**, 1235–1238 (2003)
- 4.81 Y. Miyauchi, S. Chiashi, Y. Murakami, Y. Hayashida, S. Maruyama: Fluorescence spectroscopy of single-walled carbon nanotubes synthesized from alcohol, *Chem. Phys. Lett.* **387**, 198–203 (2004)
- 4.82 O.N. Torrens, D.E. Milkie, M. Zheng, J.M. Kikkawa: Photoluminescence from intertube carrier migration in single-walled carbon nanotube bundles, *Nano Lett.* **6**, 2864–2867 (2006)
- 4.83 P.H. Tan, A.G. Rozhin, T. Hasan, P. Hu, V. Scardaci, W.I. Milne, A.C. Ferrari: Photoluminescence spectroscopy of carbon nanotube bundles: Evidence for exciton energy transfer, *Phys. Rev. Lett.* **99**, 137402 (2007)
- 4.84 O. Kiowski, K. Arnold, S. Lebedkin, F. Hennrich, M.M. Kappes: Direct observation of deep excitonic states in the photoluminescence spectra of single-walled carbon nanotubes, *Phys. Rev. Lett.* **99**, 237402 (2007)
- 4.85 O.N. Torrens, M. Zheng, J.M. Kikkawa: Energy of k -momentum dark excitons in carbon nanotubes by optical spectroscopy, *Phys. Rev. Lett.* **101**(15), 157401 (2008)
- 4.86 Y. Murakami, J. Kono: Nonlinear photoluminescence excitation spectroscopy of carbon nanotubes: Exploring the upper density limit of one-dimensional excitons, *Phys. Rev. Lett.* **102**, 037401 (2009)
- 4.87 Y. Murakami, J. Kono: Existence of an upper limit on the density of excitons in carbon nanotubes by diffusion-limited exciton-exciton annihilation: Experiment and theory, *Phys. Rev. B* **80**, 035432 (2009)
- 4.88 J.A. Fagan, J.Y. Huh, J.R. Simpson, J.L. Blackburn, J.M. Holt, B.A. Larsen, A.R. Hight Walker: Separation of empty and water-filled single-wall carbon nanotubes, *ACS Nano* **5**, 3943–3953 (2011)
- 4.89 A. Jorio, A.G. Souza Filho, G. Dresselhaus, M.S. Dresselhaus, A.K. Swan, M.S. Ünlü, B.B. Goldberg, M.A. Pimenta, J.H. Hafner, C.M. Lieber, R. Saito: G -band resonant Raman study of 62 isolated single-wall carbon nanotubes, *Phys. Rev. B* **65**, 155412 (2002)
- 4.90 H. Telg, J. Maultzsch, S. Reich, F. Hennrich, C. Thomsen: Chirality distribution and transition energies of carbon nanotubes, *Phys. Rev. Lett.* **93**, 177401 (2004)
- 4.91 S.K. Doorn, D.A. Heller, P.W. Barone, M.L. Usrey, M.S. Strano: Resonant Raman excitation profiles of individually dispersed single walled carbon nanotubes in solution, *Appl. Phys. A* **78**, 1147–1155 (2004)
- 4.92 C. Fantini, A. Jorio, M. Souza, M.S. Strano, M.S. Dresselhaus, M.A. Pimenta: Optical transition energies for carbon nanotubes from resonant Raman spectroscopy: Environment and temperature effects, *Phys. Rev. Lett.* **93**, 147406 (2004)
- 4.93 J. Maultzsch, H. Telg, S. Reich, C. Thomsen: Radial breathing mode of single-walled carbon nanotubes: Optical transition energies and chiral-index assignment, *Phys. Rev. B* **72**, 205438 (2005)

- 4.94 S.K. Doorn, M.J. O'Connell, L. Zheng, Y.T. Zhu, S. Huang, J. Liu: Raman spectral imaging of a carbon nanotube intramolecular junction, *Phys. Rev. Lett.* **94**, 016802 (2005)
- 4.95 J. Jiang, R. Saito, A. Grüneis, S.G. Chou, G.G. Samsonidze, A. Jorio, G. Dresselhaus, M.S. Dresselhaus: Intensity of the resonance Raman excitation spectra of single-wall carbon nanotubes, *Phys. Rev. B* **71**, 205420 (2005)
- 4.96 J.C. Meyer, M. Paillet, T. Michel, A. Moréac, A. Neumann, G.S. Duesberg, S. Roth, J.-L. Sauvajol: Raman modes of index-identified freestanding single-walled carbon nanotubes, *Phys. Rev. Lett.* **95**, 217401 (2005)
- 4.97 A. Jorio, C. Fantini, M.A. Pimenta, R.B. Capaz, G.G. Samsonidze, G. Dresselhaus, M.S. Dresselhaus, J. Jiang, N. Kobayashi, A. Grüneis, R. Saito: Resonance Raman spectroscopy (n,m)-dependent effects in small-diameter single-wall carbon nanotubes, *Phys. Rev. B* **71**, 075401 (2005)
- 4.98 M. Paillet, T. Michel, J.C. Meyer, V.N. Popov, L. Henrard, S. Roth, J.-L. Sauvajol: Raman active phonons of identified semiconducting single-walled carbon nanotubes, *Phys. Rev. Lett.* **96**, 257401 (2006)
- 4.99 H. Son, A. Reina, G.G. Samsonidze, R. Saito, A. Jorio, M.S. Dresselhaus, J. Kong: Raman characterization of electronic transition energies of metallic single-wall carbon nanotubes, *Phys. Rev. B* **74**, 073406 (2006)
- 4.100 Y. Yin, A.N. Vamivakas, A.G. Walsh, S.B. Cronin, M.S. Ünlü, B.B. Goldberg, A.K. Swan: Optical determination of electron-phonon coupling in carbon nanotubes, *Phys. Rev. Lett.* **98**, 037404 (2007)
- 4.101 F. Wang, W. Liu, Y. Wu, M.Y. Sfeir, L. Huang, J. Hone, S. O'Brien, L.E. Brus, T.F. Heinz, Y.R. Shen: Multiphonon Raman scattering from individual single-walled carbon nanotubes, *Phys. Rev. Lett.* **98**, 047402 (2007)
- 4.102 K.T. Nguyen, A. Gaur, M. Shim: Fano lineshape and phonon softening in single isolated metallic carbon nanotubes, *Phys. Rev. Lett.* **98**, 145504 (2007)
- 4.103 Y. Wu, J. Maultzsch, E. Knoesel, B. Chandra, M. Huang, M.Y. Sfeir, L.E. Brus, J. Hone, T.F. Heinz: Variable electron-phonon coupling in isolated metallic carbon nanotubes observed by Raman scattering, *Phys. Rev. Lett.* **99**, 027402 (2007)
- 4.104 H. Farhat, H. Son, G.G. Samsonidze, S. Reich, M.S. Dresselhaus, J. Kong: Phonon softening in individual metallic carbon nanotubes due to the Kohn anomaly, *Phys. Rev. Lett.* **99**, 145506 (2007)
- 4.105 J.C. Tsang, M. Freitag, V. Perebeinos, J. Liu, P. Avouris: Doping and phonon renormalization in carbon nanotubes, *Nat. Nanotechnol.* **2**, 725–730 (2007)
- 4.106 M. Oron-Carl, R. Krupke: Raman spectroscopic evidence for hot-phonon generation in electrically biased carbon nanotubes, *Phys. Rev. Lett.* **100**, 127401 (2008)
- 4.107 M. Fouquet, H. Telg, J. Maultzsch, Y. Wu, B. Chandra, J. Hone, T.F. Heinz, C. Thomsen: Longitudinal optical phonons in metallic and semiconducting carbon nanotubes, *Phys. Rev. Lett.* **102**, 075501 (2009)
- 4.108 T. Michel, M. Paillet, D. Nakabayashi, M. Picher, V. Jourdain, J.C. Meyer, A.A. Zahab, J.-L. Sauvajol: Indexing of individual single-walled carbon nanotubes from Raman spectroscopy, *Phys. Rev. B* **80**, 245416 (2009)
- 4.109 E.H. Hároz, W.D. Rice, B.Y. Lu, S. Ghosh, R.H. Hauge, R.B. Weisman, S.K. Doorn, J. Kono: Enrichment of armchair carbon nanotubes via density gradient ultracentrifugation: Raman spectroscopy evidence, *ACS Nano* **4**, 1955–1962 (2010)
- 4.110 J.G. Duque, H. Chen, A.K. Swan, A.P. Shreve, S. Kilina, S. Tretiak, X. Tu, M. Zheng, S.K. Doorn: Violation of the Condon approximation in semiconducting carbon nanotubes, *ACS Nano* **5**, 5233–5241 (2011)
- 4.111 G.N. Ostojic, S. Zaric, J. Kono, M.S. Strano, V.C. Moore, R.H. Hauge, R.E. Smalley: Interband recombination dynamics of resonantly-excited single-walled carbon nanotubes, *Phys. Rev. Lett.* **92**, 117402 (2004)
- 4.112 L. Huang, H.N. Pedrosa, T.D. Krauss: Ultrafast ground-state recovery of single-walled carbon nanotubes, *Phys. Rev. Lett.* **93**, 017403 (2004)
- 4.113 J. Kono, G.N. Ostojic, S. Zaric, M.S. Strano, V.C. Moore, J. Shaver, R.H. Hauge, R.E. Smalley: Ultrafast optical spectroscopy of micelle-suspended single-walled carbon nanotubes, *Appl. Phys. A* **78**, 1093–1098 (2004)
- 4.114 A. Hagen, G. Moos, V. Talalaev, T. Hertel: Electronic structure and dynamics of optically excited single-wall carbon nanotubes, *Appl. Phys. A* **78**, 1137 (2004)
- 4.115 Y.-Z. Ma, J. Stenger, J. Zimmerman, S.M. Bachilo, R.E. Smalley, R.B. Weisman, G.R. Fleming: Ultrafast carrier dynamics in single-walled carbon nanotubes probed by femtosecond spectroscopy, *J. Chem. Phys.* **120**, 3368 (2004)
- 4.116 F. Wang, G. Dukovic, L.E. Brus, T.F. Heinz: Time-resolved fluorescence in carbon nanotubes and its implication for radiative lifetimes, *Phys. Rev. Lett.* **92**, 177402 (2004)
- 4.117 R.J. Ellingson, C. Engtrakul, M. Jones, M. Samec, G. Rumbles, A.J. Nozik, M.J. Heben: Ultrafast photoresponse of metallic and semiconducting single-wall carbon nanotubes, *Phys. Rev. B* **71**, 115444 (2005)
- 4.118 S. Reich, M. Dworzak, A. Hoffmann, C. Thomsen, M.S. Strano: Excited-state carrier lifetime in single-walled carbon nanotubes, *Phys. Rev. B* **71**, 033402 (2005)
- 4.119 F. Wang, G. Dukovic, E. Knoesel, L.E. Brus, T.F. Heinz: Observation of rapid Auger recombination in optically excited semiconducting carbon nanotubes, *Phys. Rev. B* **70**, 241403 (2004)

- 4.120 A. Maeda, S. Matsumoto, H. Kishida, T. Takenobu, Y. Iwasa, M. Shiraishi, M. Ata, H. Okamoto: Large optical nonlinearity of semiconducting single-walled carbon nanotubes under resonant excitations, *Phys. Rev. Lett.* **94**, 047404 (2005)
- 4.121 C.-X. Sheng, Z.V. Vardeny, B. Dalton, R.H. Baughman: Exciton dynamics in single-walled nanotubes: Transient photoinduced dichroism and polarized emission, *Phys. Rev. B* **71**, 125427 (2005)
- 4.122 S.G. Chou, F. Plentz, J. Jiang, R. Saito, D. Nezich, H.B. Ribeiro, A. Jorio, M.A. Pimenta, G.G. Samsonidze, A.P. Santos, M. Zheng, G.B. Onoa, E.D. Semke, G. Dresselhaus, M.S. Dresselhaus: Phonon-assisted excitonic recombination channels observed in DNA-wrapped carbon nanotubes using photoluminescence spectroscopy, *Phys. Rev. Lett.* **94**, 127402 (2005)
- 4.123 Y.-Z. Ma, L. Valkunas, S.L. Dexheimer, S.M. Bachilo, G.R. Fleming: Femtosecond spectroscopy of optical excitations in single-walled carbon nanotubes: Evidence for exciton-exciton annihilation, *Phys. Rev. Lett.* **94**, 157402 (2005)
- 4.124 C. Manzoni, A. Gambetta, E. Menna, M. Meneghetti, G. Lanzani, G. Cerullo: Intersubband exciton relaxation dynamics in single-walled carbon nanotubes, *Phys. Rev. Lett.* **94**, 207401 (2005)
- 4.125 J.S. Lauret, C. Voisin, S. Berger, G. Cassaboïs, C. Delalande, P. Roussignol, L. Goux-Capes, A. Filoramo: Environmental effects on the carrier dynamics in carbon nanotubes, *Phys. Rev. B* **72**, 113413 (2005)
- 4.126 A. Hagen, M. Steiner, M.B. Raschke, C. Lienau, T. Hertel, H. Qian, A.J. Meixner, A. Hartschuh: Exponential decay lifetimes of excitons in individual single-walled carbon nanotubes, *Phys. Rev. Lett.* **95**, 197401 (2005)
- 4.127 S.G. Chou, M.F. DeCamp, J. Jiang, G.G. Samsonidze, E.B. Barros, F. Plentz, A. Jorio, M. Zheng, G.B. Onoa, E.D. Semke, A. Tokmakoff, R. Saito, G. Dresselhaus, M.S. Dresselhaus: Phonon-assisted exciton relaxation dynamics for a (6,5)-enriched DNA-wrapped single-walled carbon nanotube sample, *Phys. Rev. B* **72**, 195415 (2005)
- 4.128 G.N. Ostojic, S. Zaric, J. Kono, V.C. Moore, R.H. Hauge, R.E. Smalley: Stability of high-density one-dimensional excitons in carbon nanotubes under high laser excitation, *Phys. Rev. Lett.* **94**, 097401 (2005)
- 4.129 A. Gambetta, C. Manzoni, E. Menna, M. Meneghetti, G. Cerullo, G. Lanzani, S. Tretiak, A. Piryatinski, A. Saxena, R.L. Martin, A.R. Bishop: Real-time observation of nonlinear coherent phonon dynamics in single-walled carbon nanotubes, *Nat. Phys.* **2**, 515–520 (2006)
- 4.130 Y.-S. Lim, K.-J. Yee, J.-H. Kim, J. Shaver, E.H. H  roz, J. Kono, S.K. Doorn, R.H. Hauge, R.E. Smalley: Coherent lattice vibrations in carbon nanotubes, *Nano Lett.* **6**, 2696–2700 (2006)
- 4.131 Y. Hashimoto, Y. Murakami, S. Maruyama, J. Kono: Anisotropic decay dynamics of photoexcited aligned carbon nanotube bundles, *Phys. Rev. B* **75**, 245408 (2007)
- 4.132 D. Song, F. Wang, G. Dukovic, M. Zheng, E.D. Semke, L.E. Brus, T.F. Heinz: Direct measurement of the lifetime of optical phonons in single-walled carbon nanotubes, *Phys. Rev. Lett.* **100**, 225503 (2008)
- 4.133 K. Kang, T. Ozel, D.G. Cahill, M. Shim: Optical phonon lifetimes in single-walled carbon nanotubes by time-resolved Raman scattering, *Nano Lett.* **8**, 4642–4647 (2008)
- 4.134 J.-H. Kim, K.-J. Han, N.-J. Kim, K.-J. Yee, Y.-S. Lim, G.D. Sanders, C.J. Stanton, L.G. Booshehri, E.H. H  roz, J. Kono: Chirality-selective excitations of coherent phonons in carbon nanotubes by femtosecond optical pulses, *Phys. Rev. Lett.* **102**, 037402 (2009)
- 4.135 L. L  er, C. G  dermaier, J. Crochet, T. Hertel, D. Brida, G. Lanzani: Coherent phonon dynamics in semiconducting carbon nanotubes: A quantitative study of electron-phonon coupling, *Phys. Rev. Lett.* **102**, 127401 (2009)
- 4.136 I. Chatzakis, H. Yan, D. Song, S. Berciaud, T.F. Heinz: Temperature dependence of the anharmonic decay of optical phonons in carbon nanotubes and graphite, *Phys. Rev. B* **83**, 205411 (2011)
- 4.137 J.-H. Kim, K.-J. Yee, Y.-S. Lim, L.G. Booshehri, E.H. H  roz, J. Kono: Optical phonon dephasing in single-walled carbon nanotubes probed via impulsive stimulated Raman scattering, *Phys. Rev. B* **86**, 161415(R) (2011)
- 4.138 D.T. Nguyen, C. Voisin, P. Roussignol, C. Roquelet, J.S. Lauret, G. Cassabo  s: Elastic exciton-exciton scattering in photoexcited carbon nanotubes, *Phys. Rev. Lett.* **107**, 127401 (2011)
- 4.139 S.M. Santos, B. Yuma, S. Berciaud, J. Shaver, M. Gallart, P. Gilliot, L. Cognet, B. Lounis: All-optical trion generation in single-walled carbon nanotubes, *Phys. Rev. Lett.* **107**, 187401 (2011)
- 4.140 J.J. Crochet, S. Hoseinkhani, L. L  er, T. Hertel, S.K. Doorn, G. Lanzani: Free-carrier generation in aggregates of single-wall carbon nanotubes by photoexcitation in the ultraviolet regime, *Phys. Rev. Lett.* **107**, 257402 (2011)
- 4.141 M. Freitag, Y. Martin, J.A. Misewich, R. Martel, P. Avouris: Photoconductivity of single carbon nanotubes, *Nano Lett.* **3**, 1067–1071 (2003)
- 4.142 A. Hartschuh, E.J. S  nchez, X.S. Xie, L. Novotny: High-resolution near-field Raman microscopy of single-walled carbon nanotubes, *Phys. Rev. Lett.* **90**, 095503 (2003)
- 4.143 J.A. Misewich, R. Martel, P. Avouris, J.C. Tsang, S. Heinze, J. Tersoff: Electrically induced optical emission from a carbon nanotube FET, *Science* **300**, 783–786 (2003)
- 4.144 A. Hartschuh, H.N. Pedrosa, L. Novotny, T.D. Krauss: Simultaneous fluorescence and Raman scattering

- from single carbon nanotubes, *Science* **301**, 1354–1356 (2003)
- 4.145 J. Lefebvre, J.M. Fraser, P. Finnie, Y. Homma: Photoluminescence from an individual single-walled carbon nanotube, *Phys. Rev. B* **69**, 075403 (2004)
- 4.146 H. Htoon, M.J. O'Connell, P.J. Cox, S.K. Doorn, V.I. Klimov: Low temperature emission spectra of individual single-walled carbon nanotubes: Multiplicity of subspecies within single-species nanotube ensembles, *Phys. Rev. Lett.* **93**, 027401 (2004)
- 4.147 K. Matsuda, Y. Kanemitsu, K. Irie, T. Saiki, T. Someya, Y. Miyauchi, S. Maruyama: Photoluminescence intermittency in an individual single-walled carbon nanotube at room temperature, *Appl. Phys. Lett.* **86**, 123116 (2005)
- 4.148 K. Balasubramanian, M. Burghard, K. Kern, M. Scollari, A. Mews: Photocurrent imaging of charge transport barriers in carbon nanotube devices, *Nano Lett.* **5**, 507–510 (2005)
- 4.149 H. Htoon, M.J. O'Connell, S.K. Doorn, V.I. Klimov: Single carbon nanotubes probed by photoluminescence excitation spectroscopy: The role of phonon-assisted transitions, *Phys. Rev. Lett.* **94**, 127403 (2005)
- 4.150 J.U. Lee: Photovoltaic effect in ideal carbon nanotube diodes, *Appl. Phys. Lett.* **87**, 073101 (2005)
- 4.151 J. Chen, V. Perebeinos, M. Freitag, J. Tsang, Q. Fu, J. Liu, P. Avouris: Bright infrared emission from electrically induced excitons in carbon nanotubes, *Science* **310**, 1171–1174 (2005)
- 4.152 J.U. Lee, P.J. Codella, M. Pietrzykowski: Direct probe of excitonic and continuum transitions in the photocurrent spectroscopy of individual carbon nanotube p–n diodes, *Appl. Phys. Lett.* **90**, 053103 (2007)
- 4.153 L. Cognet, D.A. Tsybolski, J.–D.R. Rocha, C.D. Doyle, J.M. Tour, R.B. Weisman: Stepwise quenching of exciton fluorescence in carbon nanotubes by single-molecule reactions, *Science* **316**, 1465–1468 (2007)
- 4.154 A. Högele, C. Galland, M. Winger, A. Imamoğlu: Photon antibunching in the photoluminescence spectra of a single carbon nanotube, *Phys. Rev. Lett.* **100**, 217401 (2008)
- 4.155 C. Galland, A. Högele, H.E. Türeci, A. Imamoğlu: Non-Markovian decoherence of localized nanotube excitons by acoustic phonons, *Phys. Rev. Lett.* **101**, 067402 (2008)
- 4.156 A. Srivastava, H. Htoon, V.I. Klimov, J. Kono: Direct observation of dark excitons in individual carbon nanotubes: Inhomogeneity in the exchange splitting, *Phys. Rev. Lett.* **101**, 087402 (2008)
- 4.157 R. Matsunaga, K. Matsuda, Y. Kanemitsu: Evidence for dark excitons in a single carbon nanotube due to the Aharonov–Bohm effect, *Phys. Rev. Lett.* **101**, 147404 (2008)
- 4.158 K. Matsuda, T. Inoue, Y. Murakami, S. Maruyama, Y. Kanemitsu: Exciton dephasing and multiexciton recombinations in a single carbon nanotube, *Phys. Rev. B* **77**, 033406 (2008)
- 4.159 N.M. Gabor, Z. Zhong, K. Bosnick, J. Park, P.L. McEuen: Extremely efficient multiple electron-hole pair generation in carbon nanotube photodiodes, *Science* **325**, 1367–1371 (2009)
- 4.160 M. Steiner, M. Freitag, V. Perebeinos, A. Naumov, J.P. Small, A.A. Bol, P. Avouris: Gate-variable light absorption and emission in a semiconducting carbon nanotube, *Nano Lett.* **9**, 3477–3481 (2009)
- 4.161 R. Matsunaga, Y. Miyauchi, K. Matsuda, Y. Kanemitsu: Symmetry-induced nonequilibrium distributions of bright and dark exciton states in single carbon nanotubes, *Phys. Rev. B* **80**, 115436 (2009)
- 4.162 M. Freitag, M. Steiner, A. Naumov, J.P. Small, A.A. Bol, V. Perebeinos, P. Avouris: Carbon nanotube photo- and electroluminescence in longitudinal electric fields, *ACS Nano* **3**, 3744–3748 (2009)
- 4.163 S. Moritsubo, T. Murai, T. Shimada, Y. Murakami, S. Chiashi, S. Maruyama, Y.K. Kato: Exciton diffusion in air-suspended single-walled carbon nanotubes, *Phys. Rev. Lett.* **104**, 247402 (2010)
- 4.164 S. Zaric, G.N. Ostojic, J. Kono, J. Shaver, V.C. Moore, M.S. Strano, R.H. Hauge, R.E. Smalley, X. Wei: Optical signatures of the Aharonov–Bohm phase in single-walled carbon nanotubes, *Science* **304**, 1129–1131 (2004)
- 4.165 S. Zaric, G.N. Ostojic, J. Shaver, J. Kono, O. Portugall, P.H. Frings, G.L.J.A. Rikken, M. Furis, S.A. Crooker, X. Wei, V.C. Moore, R.H. Hauge, R.E. Smalley: Excitons in carbon nanotubes with broken time-reversal symmetry, *Phys. Rev. Lett.* **96**, 016406 (2006)
- 4.166 J. Shaver, J. Kono, O. Portugall, V. Krstic, G.L.J.A. Rikken, Y. Miyauchi, S. Maruyama, V. Perebeinos: Magnetic brightening of carbon nanotube photoluminescence through symmetry breaking, *Nano Lett.* **7**, 1851–1855 (2007)
- 4.167 I.B. Mortimer, R.J. Nicholas: Role of bright and dark excitons in the temperature-dependent photoluminescence of carbon nanotubes, *Phys. Rev. Lett.* **98**, 027404 (2007)
- 4.168 J. Shaver, J. Kono: Temperature dependent magneto-photoluminescence spectroscopy of carbon nanotubes: Evidence for dark excitons, *Laser Photonics Rev.* **1**, 260–274 (2007)
- 4.169 J. Shaver, S.A. Crooker, J.A. Fagan, E.K. Hobbie, N. Ubrig, O. Portugall, V. Perebeinos, P. Avouris, J. Kono: Magneto-optical spectroscopy of highly-aligned carbon nanotubes: Identifying the role of threading magnetic flux, *Phys. Rev. B* **78**, 081402 (2008)
- 4.170 J. Shaver, A.N.G. Parra-Vasquez, S. Hansel, O. Portugall, C.H. Mielke, M. von Ortenberg, R.H. Hauge, M. Pasquali, J. Kono: Alignment dynamics of carbon nanotubes in pulsed ultrahigh magnetic fields, *ACS Nano* **3**, 131 (2009)
- 4.171 R.S. Knox: *Theory of Excitons*, Solid State Physics, Vol. 5 (Academic, New York 1963)

- 4.172 R. Loudon: One-dimensional hydrogen atom, *Am. J. Phys.* **27**, 649 (1959)
- 4.173 R.J. Elliot, R. Loudon: Theory of the absorption edge in semiconductors in a high magnetic field, *J. Phys. Chem. Solids* **15**, 196–207 (1960)
- 4.174 F. Wang, G. Dukovic, L.E. Brus, T.F. Heinz: The optical resonances in carbon nanotubes arise from excitons, *Science* **308**, 838 (2005)
- 4.175 J. Maultzsch, R. Pomraenke, S. Reich, E. Chang, D. Prezzi, A. Ruini, E. Molinari, M.S. Strano, C. Thomsen, C. Lienau: Exciton binding energies in carbon nanotubes from two-photon photoluminescence, *Phys. Rev. B* **72**, 241402 (2005)
- 4.176 S. Uryu, T. Ando: Exciton absorption of perpendicularly polarized light in carbon nanotubes, *Phys. Rev. B* **74**, 155411 (2006)
- 4.177 S. Uryu, T. Ando: Cross-polarized exciton absorption in carbon nanotubes with Aharonov–Bohm flux, *Phys. Rev. B* **76**, 115420 (2007)
- 4.178 H. Kataura, Y. Kumazawa, Y. Maniwa, I. Umez, S. Suzuki, Y. Ohtsuka, Y. Achiba: Optical properties of single-wall carbon nanotubes, *Synth. Met.* **103**, 2555–2558 (1999)
- 4.179 S. Berciaud, L. Cognet, P. Poulin, R.B. Weisman, B. Lounis: Absorption spectroscopy of individual single-walled carbon nanotubes, *Nano Lett.* **7**, 1203–1207 (2007)
- 4.180 F. Wang, D.J. Cho, B. Kessler, J. Deslippe, P.J. Schuck, S.G. Louie, A. Zettl, T.F. Heinz, Y.R. Shen: Observation of excitons in one-dimensional metallic single-walled carbon nanotubes, *Phys. Rev. Lett.* **99**, 227401 (2007)
- 4.181 A.M. Rao, E. Richter, S. Bandow, B. Chase, P.C. Eklund, K.A. Williams, S. Fang, K.R. Subbaswamy, M. Menon, A. Thess, R.E. Smalley, G. Dresselhaus, M.S. Dresselhaus: Diameter-selective Raman scattering from vibrational modes in carbon nanotubes, *Science* **275**, 187–191 (1997)
- 4.182 A. Jorio, M.S. Dresselhaus, R. Saito, G.F. Dresselhaus: *Raman Spectroscopy in Graphene Related Systems* (Wiley–VCH, Weinheim 2011)
- 4.183 M.J. O’Connell, S. Sivaram, S.K. Doorn: Near-infrared resonance Raman excitation profile studies of single-walled carbon nanotube intertube interactions: A direct comparison of bundled and individually dispersed HiPco nanotubes, *Phys. Rev. B* **69**, 235415 (2004)
- 4.184 A. Jorio, A.P. Santos, H.B. Ribeiro, C. Fantini, M. Souza, J.P.M. Viera, C.A. Furtado, J. Jiang, R. Saito, L. Balzano, D.E. Resasco, M.A. Pimenta: Quantifying carbon–nanotube species with resonance Raman scattering, *Phys. Rev. B* **72**, 075207 (2005)
- 4.185 H. Telg, J. Maultzsch, C. Thomsen: Raman Intensities of the Radial-Breathing Mode in Carbon Nanotubes: The Exciton–Phonon Coupling as a Function of (m, n) , *J. Nanophoton.* **4**, 041660 (2012)
- 4.186 E.H. H  roz, J.G. Duque, X. Tu, M. Zheng, A.R. Hight Walker, R.H. Hauge, S.K. Doorn, J. Kono: Fundamental optical processes in armchair carbon nanotubes, *Nanoscale* **5**(4), 1411–1411 (2012)
- 4.187 M.A. Pimenta, A. Marucci, S.A. Empedocles, M.G. Bawendi, E.B. Hanlon, A.M. Rao, P.C. Eklund, R.E. Smalley, G. Dresselhaus, M.S. Dresselhaus: Raman modes of metallic carbon nanotubes, *Phys. Rev. B* **58**(24), R16016–R16019 (1998)
- 4.188 S.D.M. Brown, A. Jorio, M.S. Dresselhaus, G. Dresselhaus: Observations of the *D*-band feature in the Raman spectra of carbon nanotubes, *Phys. Rev. B* **64**(7), 073403 (2001)
- 4.189 S. Piscanec, M. Lazzeri, J. Robertson, A.C. Ferrari, F. Mauri: Optical phonons in carbon nanotubes: Kohn anomalies, Peierls distortions, and dynamic effects, *Phys. Rev. B* **75**(3), 035427 (2007)
- 4.190 E.H. H  roz, J.G. Duque, W.D. Rice, C.G. Densmore, J. Kono, S.K. Doorn: Resonant Raman spectroscopy of armchair carbon nanotubes: Absence of broad *G*[−] feature, *Phys. Rev. B* **84**(12), 121403 (2011)
- 4.191 A.M. Rao, P.C. Eklund, S. Bandow, A. Thess, R.E. Smalley: Evidence for charge transfer in doped carbon nanotube bundles from Raman scattering, *Nature* **388**, 257 (1997)
- 4.192 S.B. Cronin, A.K. Swan, M.S.   nl  , B.B. Goldberg, M.S. Dresselhaus, M. Tinkham: Resonant Raman spectroscopy of individual metallic and semiconducting single-wall carbon nanotubes under uniaxial strain, *Phys. Rev. B* **72**, 035425 (2005)
- 4.193 S. Berciaud, C. Voisin, H. Yan, B. Chandra, R. Caldwell, Y. Shan, L.E. Brus, J. Hone, T.F. Heinz: Excitons and high-order optical transitions in individual carbon nanotubes: A Rayleigh scattering spectroscopy study, *Phys. Rev. B* **81**, 041414 (2010)
- 4.194 A.G. Souza Filho, A. Jorio, G.G. Samsonidze, G. Dresselhaus, M.S. Dresselhaus, A.K. Swan, M.S.   nl  , B.B. Goldberg, R. Saito, J.H. Hafner, C.M. Lieber, M.A. Pimenta: Probing the electronic trigonal warping effect in individual single-wall carbon nanotubes using phonon spectra, *Chem. Phys. Lett.* **354**, 62–68 (2002)
- 4.195 M.Y. Sfeir, F. Wang, L. Huang, C.C. Chuang, J. Hone, S.P. O’Brien, T.F. Heinz, L.E. Brus: Probing electronic transitions in individual carbon nanotubes by Rayleigh scattering, *Science* **306**, 1540 (2004)
- 4.196 M.Y. Sfeir, T. Beetz, F. Wang, L. Huang, X.M.H. Huang, M. Huang, J. Hone, S. O’Brien, J.A. Misewich, T.F. Heinz, L. Wu, Y. Zhu, L.E. Brus: Optical spectroscopy of individual single-walled carbon nanotubes of defined chiral structure, *Science* **312**, 554–556 (2006)
- 4.197 K. Liu, J. Deslippe, F. Xiao, R.B. Capaz, X. Hong, S. Aloni, A. Zettl, W. Wang, X. Bai, S.G. Louie, E. Wang, F. Wang: An atlas of carbon nanotube optical transitions, *Nat. Nanotechnol.* **7**, 325–329 (2012)
- 4.198 D.Y. Joh, L.H. Herman, S.  Y. Ju, J. Kinder, M.A. Segal, J.N. Johnson, G.K.L. Chan, J. Park: On-chip Rayleigh

- imaging and spectroscopy of carbon nanotubes, *Nano Lett.* **11**, 1–7 (2011)
- 4.199 T. Hertel, G. Moos: Electron–phonon interaction in single-wall carbon nanotubes: A time-domain study, *Phys. Rev. Lett.* **84**, 5002 (2000)
- 4.200 J.-H. Kim, J. Park, B.Y. Lee, D. Lee, K.-J. Yee, Y.-S. Lim, L.G. Booshehri, E.H. H  roz, J. Kono, S.-H. Baik: Polarization anisotropy of transient carrier and phonon dynamics in carbon nanotubes, *J. Appl. Phys.* **105**, 103506 (2009)
- 4.201 J. Wang, M.W. Graham, Y.-Z. Ma, G.R. Fleming, R.A. Kaindl: Ultrafast spectroscopy of midinfrared internal exciton transitions in separated single-walled carbon nanotubes, *Phys. Rev. Lett.* **104**, 177401 (2010)
- 4.202 B. Gao, G.B. Hartland, L. Huang: Transient absorption spectroscopy and imaging of individual chirality-assigned single-walled carbon nanotubes, *ACS Nano* **6**, 5083 (2012)
- 4.203 J.S. Lauret, C. Voisin, G. Cassabo  s, C. Delalande, P. Roussignol, O. Jost, L. Capes: Ultrafast carrier dynamics in single-wall carbon nanotubes, *Phys. Rev. Lett.* **90**, 057404 (2003)
- 4.204 K. Kato, K. Ishioka, M. Kitajima, J. Tang, R. Saito, H. Petek: Coherent phonon anisotropy in aligned single-walled carbon nanotubes, *Nano Lett.* **8**, 3102–3108 (2008)
- 4.205 L.G. Booshehri, C.L. Pint, G.D. Sanders, L. Ren, C. Sun, E.H. H  roz, J.-H. Kim, K.-J. Yee, Y.-S. Lim, R.H. Hauge, C.J. Stanton, J. Kono: Polarization dependence of coherent phonon generation and detection in highly-aligned single-walled carbon nanotubes, *Phys. Rev. B* **83**, 195411 (2011)
- 4.206 Y.-S. Lim, K.-J. Yee, J.-H. Kim, E.H. H  roz, J. Shaver, J. Kono, S.K. Doorn, R.H. Hauge, R.E. Smalley: Chirality assignment of micelle-suspended single-walled carbon nanotubes using coherent phonon oscillations, *J. Korean Phys. Soc.* **51**, 306 (2007)
- 4.207 A.M. Weiner, J.P. Heritage, E.M. Kirschner: High-resolution femtosecond pulse shaping, *J. Opt. Soc. Am. B* **5**(8), 1563 (1988)
- 4.208 R.J. Elliot, R. Loudon: Theory of fine structure on the absorption edge in semiconductors, *J. Phys. Chem. Solids* **8**, 382–388 (1959)
- 4.209 M.S. Dresselhaus, G. Dresselhaus, R. Saito, A. Jorio: Exciton photophysics of carbon nanotubes, *Annu. Rev. Phys. Chem.* **58**, 719–747 (2007)
- 4.210 T. Ando: Excitons in carbon nanotubes, *J. Phys. Soc. Jpn.* **66**, 1066–1073 (1997)
- 4.211 T. Ando: Excitons in carbon nanotubes revisited: Dependence on diameter, Aharonov–Bohm flux, and strain, *J. Phys. Soc. Jpn.* **73**, 3351–3363 (2004)
- 4.212 T.G. Pedersen: Variational approach to excitons in carbon nanotubes, *Phys. Rev. B* **67**, 073401 (2003)
- 4.213 C.L. Kane, E.J. Mele: Ratio problem in single carbon nanotube fluorescence spectroscopy, *Phys. Rev. Lett.* **90**, 207401 (2003)
- 4.214 C.D. Spataru, S. Ismail-Beigi, L.X. Benedict, S.G. Louie: Excitonic effects and optical spectra of single-walled carbon nanotubes, *Phys. Rev. Lett.* **92**, 077402 (2004)
- 4.215 E. Chang, G. Bussi, A. Ruini, E. Molinari: Excitons in carbon nanotubes: An *ab initio* symmetry-based approach, *Phys. Rev. Lett.* **92**, 196401 (2004)
- 4.216 T.G. Pederson: Exciton effects in carbon nanotubes, *Carbon* **42**, 1007 (2004)
- 4.217 V. Perebeinos, J. Tersoff, P. Avouris: Scaling of excitons in carbon nanotubes, *Phys. Rev. Lett.* **92**, 257402 (2004)
- 4.218 C.L. Kane, E.J. Mele: Electron interactions and scaling relations for optical excitations in carbon nanotubes, *Phys. Rev. Lett.* **93**, 197402 (2004)
- 4.219 H. Zhao, S. Mazumdar: Electron–electron interaction effects on the optical excitations of semiconducting single-walled carbon nanotubes, *Phys. Rev. Lett.* **93**, 157402 (2004)
- 4.220 E. Chang, G. Bussi, A. Ruini, E. Molinari: First-principles approach for the calculation of optical properties of one-dimensional systems with helical symmetry: The case of carbon nanotubes, *Phys. Rev. B* **72**, 195423 (2005)
- 4.221 V. Perebeinos, J. Tersoff, P. Avouris: Radiative lifetime of excitons in carbon nanotubes, *Nano Lett.* **5**, 2495–2499 (2005)
- 4.222 C.D. Spataru, S. Ismail-Beigi, R.B. Capaz, S.G. Louie: Theory and *ab initio* calculation of radiative lifetime of excitons in semiconducting carbon nanotubes, *Phys. Rev. Lett.* **95**, 247402 (2005)
- 4.223 T. Ando: Effects of valley mixing and exchange on excitons in carbon nanotubes with Aharonov–Bohm flux, *J. Phys. Soc. Jpn.* **75**, 024707 (2006)
- 4.224 J. Deslippe, C.D. Spataru, D. Prendergast, S.G. Louie: Bound excitons in metallic single-walled carbon nanotubes, *Nano Lett.* **7**, 1626–1630 (2007)
- 4.225 S. Kilina, S. Tretiak, S.K. Doorn, Z. Luo, F. Papadimitrakopoulos, A. Piryatinski, A. Saxena, A.R. Bishop: Cross-polarized excitons in carbon nanotubes, *Proc. Natl. Acad. Sci. USA* **105**, 6797–6802 (2008)
- 4.226 S. Uryu, T. Ando: Excitons in metallic carbon nanotubes with Aharonov–Bohm flux, *Phys. Rev. B* **77**, 205407 (2008)
- 4.227 P.T. Araujo, A. Jorio, M.S. Dresselhaus, K. Sato, R. Saito: Diameter dependence of the dielectric constant for the excitonic transition energy of single-wall carbon nanotubes, *Phys. Rev. Lett.* **103**, 146802 (2009)
- 4.228 T. Ando: Environment effects on excitons in semiconducting carbon nanotubes, *J. Phys. Soc. Jpn.* **79**, 024706 (2010)
- 4.229 A.R.T. Nugraha, R. Saito, K. Sato, P.T. Araujo, A. Jorio, M.S. Dresselhaus: Dielectric constant model for environmental effects on the exciton energies of single wall carbon nanotubes, *Appl. Phys. Lett.* **97**, 091905 (2010)

- 4.230 J. Maultzsch, H. Telg, S. Reich, C. Thomsen: Radial breathing mode of single-walled carbon nanotubes: Optical transition energies and chiral-index assignment, *Phys. Rev. B* **72**, 205438 (2005)
- 4.231 E. Chang, D. Prezzi, A. Ruini, E. Molinari: Dark excitons in carbon nanotubes, *Phys. Rev. B* (2012), in press
- 4.232 G. Dukovic, F. Wang, D. Song, M.Y. Sfeir, T.F. Heinz, L.E. Brus: Structural dependence of excitonic optical transitions and band-gap energies in carbon nanotubes, *Nano Lett.* **5**, 2314–2318 (2005)
- 4.233 F. Wang, D.J. Cho, B. Kessler, J. Deslippe, P.J. Schuck, S.G. Louie, A. Zettl, T.F. Heinz, Y.R. Shen: Observation of excitons in one-dimensional metallic single-walled carbon nanotubes, *Phys. Rev. Lett.* **99**, 227401 (2007)
- 4.234 E.H. H  roz, J.G. Duque, B.Y. Lu, P. Nikolaev, S. Arepalli, R.H. Hauge, S.K. Doorn, J. Kono: Unique origin of colors of armchair carbon nanotubes, *J. Am. Chem. Soc.* **134**, 4461–4464 (2011)
- 4.235 A.B. Kaiser: Electronic transport properties of conducting polymers and carbon nanotubes, *Rep. Prog. Phys.* **64**(1), 1 (2000)
- 4.236 J.E. Fischer, H. Dai, A. Thess, R. Lee, N.M. Hanjani, D.L. Dehaas, R.E. Smalley: Metallic resistivity in crystalline ropes of single-wall carbon nanotubes, *Phys. Rev. B* **55**, R4921–R4924 (1997)
- 4.237 G.T. Kim, E.S. Choi, D.C. Kim, D.S. Suh, Y.W. Park, K. Liu, G. Duesberg, S. Roth: Magnetoresistance of an entangled single-wall carbon-nanotube network, *Phys. Rev. B* **58**, 16064–16069 (1998)
- 4.238 Y. Yosida, I. Oguro: Variable range hopping conduction in bulk samples composed of single-walled carbon nanotubes, *J. Appl. Phys.* **86**(2), 999–1003 (1999)
- 4.239 M.S. Fuhrer, M.L. Cohen, A. Zettl, V. Crespi: Localization in single-walled carbon nanotubes, *Solid State Commun.* **109**(2), 105–109 (1998)
- 4.240 P. Pipinys, A. Kiveris: Phonon-assisted tunnelling in electrical conductivity of individual carbon nanotubes and networks ones, *Physica B* **403**(19/20), 3730–3733 (2008)
- 4.241 A.B. Kaiser, K.J. Challis, G.C. McIntosh, G.T. Kim, H.Y. Yu, J.G. Park, S.H. Jhang, Y.W. Park: Frequency and field dependent conductivity of carbon nanotube networks, *Curr. Appl. Phys.* **2**(2), 163–166 (2002)
- 4.242 H. Xu, S. Zhang, S.M. Anlage, L. Hu, G. Gr  ner: Frequency- and electric-field-dependent conductivity of single-walled carbon nanotube networks of varying density, *Phys. Rev. B* **77**, 075418 (2008)
- 4.243 M. Bockrath, D.H. Cobden, P.L. McEuen, N.G. Chopra, A. Zettl, A. Thess, R.E. Smalley: Single-electron transport in ropes of carbon nanotubes, *Science* **275**, 1922–1925 (1997)
- 4.244 W. Liang, M. Bockrath, D. Bozovic, J.H. Hafner, M. Tinkham, H. Park: Fabry–Perot interference in a nanotube electron waveguide, *Nature* **411**, 665 (2001)
- 4.245 A. Javey, J. Guo, Q. Wang, M. Lundstrom, H. Dai: Ballistic carbon nanotube field-effect transistors, *Nature* **424**, 654 (2003)
- 4.246 D.H. Cobden, M. Bockrath, P.L. McEuen, A.G. Rinzier, R.E. Smalley: Spin splitting and even-odd effects in carbon nanotubes, *Phys. Rev. Lett.* **81**, 681–684 (1998)
- 4.247 S.J. Tans, M.H. Devoret, H. Dai, A. Thess, R.E. Smalley, L.J. Geerligs, C. Dekker: Individual single-wall carbon nanotubes as quantum wires, *Nature* **386**, 474–477 (1997)
- 4.248 S.J. Tans, A.R.M. Verschueren, C. Dekker: Room-temperature transistor based on a single carbon nanotube, *Nature* **393**, 49–52 (1998)
- 4.249 R. Martel, T. Schmidt, H.R. Shea, T. Hertel, P. Avouris: Single- and multi-wall carbon nanotube field-effect transistors, *Appl. Phys. Lett.* **73**(17), 2447–2449 (1998)
- 4.250 S.J. Kang, C. Kocabas, T. Ozel, M. Shim, N. Pim-parkar, M.A. Alam, S.V. Rotkin, J.A. Rogers: High-performance electronics using dense, perfectly aligned arrays of single-walled carbon nanotubes, *Nat. Nanotechnol.* **2**, 230–236 (2007)
- 4.251 J.U. Lee, P.P. Gipp, C.M. Heller: Carbon nanotube p–n junction diodes, *Appl. Phys. Lett.* **85**, 145 (2004)
- 4.252 E. Pop, D. Mann, J. Cao, Q. Wang, K. Goodson, H. Dai: Negative differential conductance and hot phonons in suspended nanotube molecular wires, *Phys. Rev. Lett.* **95**, 155505 (2005)
- 4.253 M. Bockrath, D.H. Cobden, J. Lu, A.G. Rinzier, R.E. Smalley, L. Balents, P.L. McEuen: Luttinger liquid behavior in carbon nanotubes, *Nature* **397**, 598 (1999)
- 4.254 H.W.C. Postma, T. Teepen, Z. Yao, M. Grifoni, C. Dekker: Carbon nanotube single-electron transistors at room temperature, *Science* **293**, 76–79 (2001)
- 4.255 S. Heinze, J. Tersoff, R. Martel, V. Derycke, J. Appenzeller, P. Avouris: Carbon nanotubes as Schottky barrier transistors, *Phys. Rev. Lett.* **89**, 106801 (2002)
- 4.256 S. Datta: *Electronic Transport in Mesoscopic Systems* (Cambridge Univ. Press, Cambridge 1995)
- 4.257 H. Mathieu: *Physique des Semiconducteurs et des Composants   lectroniques* (Dunod, Paris 2001)
- 4.258 M. Kr  ger, M.R. Buitelaar, T. Nussbaumer, C. Sch  nberger, L. Forr  : Electrochemical carbon nanotube field-effect transistor, *Appl. Phys. Lett.* **78**(9), 1291–1293 (2001)
- 4.259 W. Kim, A. Javey, O. Vermesh, Q. Wang, Y. Li, H. Dai: Hysteresis caused by water molecules in carbon nanotube field-effect transistors, *Nano Lett.* **3**(2), 193–198 (2003)
- 4.260 J. Guo, S. Goasguen, M. Lundstrom, S. Datta: Metal–insulator–semiconductor electrostatics of carbon nanotubes, *Appl. Phys. Lett.* **81**(8), 1486–1488 (2002)
- 4.261 J.–C. Charlier, X. Blase, S. Roche: Electronic and transport properties of nanotubes, *Rev. Mod. Phys.* **79**, 677–732 (2007)

- 4.262 R. Martel, V. Derycke, C. Lavoie, J. Appenzeller, K.K. Chan, J. Tersoff, P. Avouris: Ambipolar electrical transport in semiconducting single-wall carbon nanotubes, *Phys. Rev. Lett.* **87**, 256805 (2001)
- 4.263 J. Kong, E. Yenilmez, T.W. Tombler, W. Kim, H. Dai, R.B. Laughlin, L. Liu, C.S. Jayanthi, S.Y. Wu: Quantum interference and ballistic transmission in nanotube electron waveguides, *Phys. Rev. Lett.* **87**, 106801 (2001)
- 4.264 F. Léonard, J. Tersoff: Role of Fermi-level pinning in nanotube Schottky diodes, *Phys. Rev. Lett.* **84**(20), 4693–4696 (2000)
- 4.265 A. Javey, P. Qi, Q. Wang, H. Dai: Ten- to 50-nm-long quasi-ballistic carbon nanotubes devices obtained without complex lithography, *Proc. Natl. Acad. Sci. USA* **101**, 13408–13410 (2004)
- 4.266 R. Egger, A.O. Gogolin: Effective low-energy theory for correlated carbon nanotubes, *Phys. Rev. Lett.* **79**, 5082 (1997)
- 4.267 Z. Yao, H.W.C. Postma, L. Balents, C. Dekker: Carbon nanotube intramolecular junctions, *Nature* **402**, 273 (1999)
- 4.268 J. Cao, Q. Wang, M. Rolandi, H. Dai: Aharonov–Bohm interference and beating in single-walled carbon-nanotube interferometers, *Phys. Rev. Lett.* **93**, 216803 (2004)
- 4.269 E.D. Minot, Y. Yaish, V. Sazonova, P.L. McEuen: Determination of electron orbital magnetic moments in carbon nanotubes, *Nature* **428**, 536–539 (2004)
- 4.270 P. Avouris, Z. Chen, V. Perebeinos: Carbon-based electronics, *Nat. Nanotechnol.* **2**, 605–615 (2007)
- 4.271 L.X. Benedict, S.G. Louie, M.L. Cohen: Heat capacity of carbon nanotubes, *Solid State Commun.* **100**(3), 177–180 (1996)
- 4.272 J. Hone, B. Batlogg, Z. Benes, A.T. Johnson, J.E. Fischer: Quantized phonon spectrum of single-wall carbon nanotubes, *Science* **289**(5485), 1730–1733 (2000)
- 4.273 J. Heremans, C.P. Beetz: Thermal conductivity and thermopower of vapor-grown graphite fibers, *Phys. Rev. B* **32**, 1981–1986 (1985)
- 4.274 S. Berber, Y.-K. Kwon, D. Tománek: Unusually high thermal conductivity of carbon nanotubes, *Phys. Rev. Lett.* **84**, 4613–4616 (2000)
- 4.275 J. Hone, M. Whitney, C. Piskoti, A. Zettl: Thermal conductivity of single-walled carbon nanotubes, *Phys. Rev. B* **59**, R2514–R2516 (1999)
- 4.276 E. Pop, D. Mann, Q. Wang, K. Goodson, H. Dai: Thermal conductance of an individual single-wall carbon nanotube above room temperature, *Nano Lett.* **6**(1), 96–100 (2006)
- 4.277 C. Yu, L. Shi, Z. Yao, D. Li, A. Majumdar: Thermal conductance and thermopower of an individual single-wall carbon nanotube, *Nano Lett.* **5**(9), 1842–1846 (2005)
- 4.278 N. Mingo, D.A. Broido: Carbon nanotube ballistic thermal conductance and its limits, *Phys. Rev. Lett.* **95**, 096105 (2005)
- 4.279 P. Kim, L. Shi, A. Majumdar, P.L. McEuen: Thermal transport measurements of individual multiwalled nanotubes, *Phys. Rev. Lett.* **87**, 215502 (2001)
- 4.280 A.N. Volkov, L.V. Zhigilei: Scaling laws and mesoscopic modeling of thermal conductivity in carbon nanotube materials, *Phys. Rev. Lett.* **104**, 215902 (2010)
- 4.281 R.S. Prasher, X.J. Hu, Y. Chalopin, N. Mingo, K. Lofgreen, S. Volz, F. Cleri, P. Keblinski: Turning carbon nanotubes from exceptional heat conductors into insulators, *Phys. Rev. Lett.* **102**, 105901 (2009)
- 4.282 C.F. Cornwell, L.T. Wille: Elastic properties of single-walled carbon nanotubes in compression, *Solid State Commun.* **101**, 555–558 (1997)
- 4.283 J.P. Lu: Elastic properties of carbon nanotubes and nanoropes, *Phys. Rev. Lett.* **79**, 1297–1300 (1997)
- 4.284 G. Overney, W. Zhong, D. Tomanek: Structural rigidity and low-frequency vibrational-modes of long carbon tubules, *Z. Phys. D* **27**, 93–96 (1993)
- 4.285 M.M.J. Treacy, T.W. Ebbesen, J.M. Gibson: Exceptionally high young's modulus observed for individual carbon nanotubes, *Nature* **381**, 678–680 (1996)
- 4.286 B.I. Yakobson, C.J. Brabec, J. Bernholc: Nanomechanics of carbon tubes: Instabilities beyond linear range, *Phys. Rev. Lett.* **76**, 2511–2514 (1996)
- 4.287 E. Hernandez, C. Goze, A. Rubio: Elastic properties of C and B_xC_yN_z composite nanotubes, *Phys. Rev. Lett.* **80**, 4502–4505 (1998)
- 4.288 B.I. Yakobson, C.J. Brabec, J. Bernholc: Structural mechanics of carbon nanotubes: From continuum elasticity to atomistic fracture, *J. Comput.-Aided Mater. Des.* **3**, 173–182 (1996)
- 4.289 J. Tersoff: Empirical interatomic potential for carbon, with applications to amorphous carbon, *Phys. Rev. Lett.* **61**, 2879–2882 (1988)
- 4.290 D.W. Brenner: Empirical potential for hydrocarbons for use in simulating the chemical vapor deposition of diamond films, *Phys. Rev. B* **42**, 9458–9471 (1990)
- 4.291 J. Tersoff, R.S. Ruoff: Structural-properties of a carbon nanotube crystal, *Phys. Rev. Lett.* **73**, 676–679 (1994)
- 4.292 B.I. Yakobson: Mechanical relaxation and “intramolecular plasticity” in carbon nanotubes, *Appl. Phys. Lett.* **72**, 918–920 (1998)
- 4.293 T. Belytschko, S.P. Xiao, G.C. Schatz, R.S. Ruoff: Simulation of the fracture of nanotubes, *Phys. Rev. B* **65**, 235430–1–235430–8 (2002)
- 4.294 S. Ogata, Y. Shibutani: Ideal tensile strength and band gap of single-walled carbon nanotubes, *Phys. Rev. B* **68**, 165409–1–165409–4 (2003)
- 4.295 J. Bernholc, C. Brabec, M. Buongiorno Nardelli, A. Maiti, C.M. Roland, B.I. Yakobson: Theory of growth and mechanical properties of nanotubes, *Appl. Phys. A* **67**, 39–46 (1998)
- 4.296 T. Dumitrica, M. Hua, B.I. Yakobson: Symmetry-, time-, and temperature-dependent strength of carbon nanotubes, *PNAS* **103**, 6105–6109 (2006)

- 4.297 M. Sammakorpi, A. Krashennikov, A. Kuronen, K. Nordlund, K. Kaski: Mechanical properties of carbon nanotubes with vacancies and related defects, *Phys. Rev. B* **70**, 245416–1–245416–8 (2004)
- 4.298 A.J. Stone, D.J. Wales: Theoretical studies of icosahedral C_{60} and some related species, *Chem. Phys. Lett.* **128**, 501–503 (1986)
- 4.299 T. Dumitrica, T. Belytschko, B.I. Yakobson: Bond-breaking bifurcation states in carbon nanotube fracture, *J. Chem. Phys.* **118**, 9485–9488 (2003)
- 4.300 M. Buongiorno Nardelli, B.I. Yakobson, J. Bernholc: Brittle and ductile behavior in carbon nanotubes, *Phys. Rev. Lett.* **81**, 4656–4659 (1998)
- 4.301 M. Menon, E. Richter, K.R. Subbaswamy: Structural and vibrational properties of fullerenes and nanotubes in a nonorthogonal tight-binding scheme, *J. Chem. Phys.* **104**, 5875–5882 (1996)
- 4.302 D. Srivastava, M. Menon, K. Cho: Nanoplasticity of single-wall carbon nanotubes under uniaxial compression, *Phys. Rev. Lett.* **83**, 2973–2976 (1999)
- 4.303 J.-P. Salvetat, G.A.D. Briggs, J.-M. Bonard, R.R. Bacsá, A.J. Kulik, T. Stöckli, N.A. Burnham, L. Forró: Elastic and shear moduli of single-walled carbon nanotube, *Phys. Rev. Lett.* **82**(5), 944–947 (1999)
- 4.304 D.A. Walters, L.M. Ericson, M.J. Casavant, J. Liu, D.T. Colbert, K.A. Smith, R.E. Smalley: Elastic strain of freely suspended single-wall carbon nanotube ropes, *Appl. Phys. Lett.* **74**, 3803–3805 (1999)
- 4.305 M.-F. Yu, B.S. Files, S. Arepalli, R.S. Ruoff: Tensile loading of ropes of single wall carbon nanotubes and their mechanical properties, *Phys. Rev. Lett.* **84**, 5552–5555 (2000)
- 4.306 S.A. Chesnokov, V.A. Nalimova, A.G. Rinzier, R.E. Smalley, J.E. Fischer: Mechanical energy storage in carbon nanotube springs, *Phys. Rev. Lett.* **82**, 343–346 (1999)
- 4.307 J. Tang, L.C. Qin, T. Sasaki, M. Yudasaka, A. Matsushita, S. Iijima: Compressibility and polygonization of single-walled carbon nanotubes under hydrostatic pressure, *Phys. Rev. Lett.* **85**, 1887–1889 (2000)
- 4.308 A. Krishnan, E. Dujardin, T.W. Ebbesen, P.N. Yianilos, M.M.J. Treacy: Young's modulus of single-walled nanotubes, *Phys. Rev. B* **58**, 14013–14019 (1998)
- 4.309 M.-S. Wang, D. Golberg, Y. Bando: Tensile tests on individual single-walled carbon nanotubes: Linking nanotube strength with its defects, *Adv. Mater.* **22**, 4071–4075 (2010)
- 4.310 J.Y. Huang, S. Chen, Z.Q. Wang, K. Kempa, Y.M. Wang, S.H. Jo, G. Chen, M.S. Dresselhaus, Z.F. Ren: Superplastic carbon nanotubes, *Nature* **439**, 281 (2006)